THE USE OF STEP SCAN FT-IR/PAS FOR THE STUDY OF STRUCTURAL CHANGES IN COAL AND CHAR PARTICLES DURING GASIFICATION

Osamu Yamada, Hajime Yasuda, Yasushi Soneda, Mitsuo Kobayashi,
Mitsunori Makino, and Mamoru Kaiho
National Institute for Resources and Environment
16-3 Onogawa, Tsukuba, Ibaraki 305 JAPAN

Key words: coal, char, step scan FT-IR/PAS

INTRODUCTION

To understand the reactions occur during coal gasification, it is essential to investigate reactivity and structural changes in coal and char. As coal and char are solid which hardly dissolve into most of solvents, variety of applicable methods for analyses is limited. An FT-IR spectroscopy is a promising method to detect the status of various kinds of functional groups and their chemical and physical changes. Recently, FT-IR photoacoustic spectroscopy(FT-IR/PAS) of coal has been intensively studied.[1] Depth profiling analyses using FT-IR/PAS is also discussed focusing on the technique to avoid a saturation of the photoacoustic signal.[2-4] In this paper, a step scan FT-IR/PAS with a phase modulation was applied to depth profiling of coal particles whose surfaces were treated by oxidation and ion-irradiation to elucidate a sampling depth. Depth profile of gasification char particles obtained from HYCOL entrained flow type gasifier were analyzed by step scan FT-IR/PAS.

EXPERIMENTAL

Preparation of oxidized coal samples

20g of Miike coal(C: 82.2%, daf; H: 6.2%, daf; N: 1.0%, daf; ash: 7.7%, dry, 24~60mesh) was placed in a glass-made, constant volume closed reactor equipped with a circulator, and was dried at 150°C under vacuum for 3 weeks. Oxidation reaction was initiated by introducing oxygen from the reservoir to the reactor maintained at 100°C. Pressure drop was monitored by pressure gauge(Balzers APG010) to calculate the amount of oxygen absorbed into coal.

Taiheiyo coal(C: 74.6%, daf; H: 6.6%, daf; N: 1.4%, daf; ash: 12.9%, dry; particles of 2~5mm) was held in a stainless steel wire mesh and oxidized in a air stream heated up to 300°C for 1h.

Oxidized coal samples were used for FT-IR/PAS analyses without further pulverization. After IR analyses, each sample is mixed with phenol resin, solidified and polished to make a cross sectional observation by a microscope using reflected light with an oil immersion method.

Preparation of ion-irradiated coal

Taiheiyo coal(60~100mesh) was dried under vacuum(~10⁴torr) at 170°C for 3 weeks. 4g of the dried coal was exposed to irradiation of argon ion with energy of 100keV for 4h using 200keV ion implanter(B) at Ion Engineering Center Corporation(Osaka, Japan).

Gasification Char

Chars were produced from Taiheiyo coal and Muswellbrook coal(C:80.3, daf; H:5.5, daf, N:1.7, daf, ash 11.7%, dry) during the operation of HYCOL gasifier (Chiba, Japan)[5].

FT-IR measurement

A Biorad FTS-60A/896 step scan FT-IR spectrometer was used for all spectral measurements. Spectra were recorded at resolution of 8cm⁻¹ using an MTEC model 100 photoacoustic cell with its accompanying preamplifier/power supply. Helium was used as the carrier gas in the PA cell. Stanford Research Systems SR510 lock-in amplifier was used when phase modulation was applied. Step scan speed/phase modulation frequency of 10/100Hz and 50/400Hz was used for the FT-IR measurement.

RESULTS AND DISCUSSION

Step scan FT-IR/PAS with a phase modulation

FT-IR/PAS has been in use for about ten years.[2] Many photoacoustic applications involve the study of the spectra for layered and heterogeneous samples with varying interferometer scanning velocity, to probe deeper into them

as the velocity is reduced. The main advantage of step scan interferometry for PAS is that a single modulation frequency can be applied over the entire spectral range to generate the PA signal. Step scan data collection for depth profiling experiments produces a constant sampling depth across the spectrum for each frequency used.[4] Spectrum obtained without phase modulation is quite photoacoustically saturated, but the phase modulated spectra are not. Among the vector component of PA signals, in-phase(0o) component carries response of deep layer and quadrature(90o) component takes signal of surface layer. In principle, by changing the phase angle of the lock-in amplifier, it should be possible to probe different depths of the sample with the same depth for all infrared frequencies in the spectrum.

Oxidized coal

Results of oxidation of Miike coal is summarized in Table 1. Main product in gaseous phase was water. Approximately one half of total amount of oxygen reacted($O_2 react$) was consumed to form H_2O, CO and CO_2. Oxidized coal samples which gained 0.54~2.36%(initial coal weight basis) of oxygen was consequently obtained. Photoacoustic spectra recorded at 2.5kHz(rapid scan) were shown in Figure 4. PA spectrum of unoxidized(dried) Miike coal recorded at the same FT-IR settings was used for reference.

Absorption peak at around 1700cm-1, attributable to carbonyl group, increased by oxidation. Broad peak reflects various kinds of carbonyl entities. Shoulder peak observed at higher than 1700cm-1 is attributed to ester or carboxylic acid. Small peaks detected at 1540cm-1 may be attributed to carboxylic ion. Besides, peaks at 2800~3050cm-1 decreased with oxidation indicating that reaction of dehydrogenation from mainly aliphatic compounds proceeded. Absorption increased around 3400cm-1 can be attributed to formation of hydroxyl group. PA spectra obtained here seems to be quite similar to those acquired by diffuse reflectance FT-IR spectroscopy[6] except OH region.

Depth profiling analyses of a series of oxidized coal samples was performed by using step scan mode(step speed/phase modulation frequency = 50Hz/400Hz). Figure 2 illustrate step scan FT-IR/PA spectra of oxidized Miike coal which are measured and phase-separated with phase angles of 45o and 0o respectively. PA spectrum of unoxidized Miike coal was used for background correction. In the layer near surface detected with phase angle of 45o(A), absorption at 1700cm-1 and 1100cm-1 increased indicating the formation of oxygen containing functional groups such as C=O and C-O with increase in the amount of oxygen reacted with coal. On the other hand, peaks at 2800~3050cm-1 did not show a definite increase nor decrease with series of oxidation conditions. Similar tendency of the intensity changes in peaks was observed when phase angle was decreased to 0o to obtain the signals from deeper layer as shown in Figure 2(B).

It is assumed that oxygen containing functional groups formed by oxidation uniformly distributes in oxidized layer, but dehydrogenation reaction takes place mainly in the surface layer. Other interpretation may be that aliphatic compounds decomposed and released by oxidation moves inside coal particle with certain mobility.

Michaelian utilize an FT-IR spectrometer with STop-and-Go mode for depth profiling of oxidized coal and estimated the thickness of oxidized layer at ~12μm corresponding to the modulation frequency of 200Hz.[3] This estimation, however, involves some assumption. Measurement of actual sampling depth is required. Oxidized Miike coal samples were used for cross-sectional observation by microscope with reflected lights. No obvious oxidation layer could be seen by microscope observation, possibly due to the mild oxidation conditions. Taiheiyo coal oxidized at 300oC was used for estimation of sampling depth of step scan FT-IR/PAS measurement. Figure 3 shows depth profiling PA spectra of oxidized Taiheiyo coal with various modulation frequencies and phase angles. PA spectra of unoxidized Taiheiyo coal was used for back ground correction to compare the changes in peaks before and after oxidation. When modulation frequency of 400Hz and phase angle of 90o were selected, the vicinity of coal surface should be detected. Considerable decrease in peaks at 2800~3050cm-1 attributed to CH stretching band was observed. Decreasing phase angle from 90o to 0o to obtain the signals of deeper layer, a peak at around 1700cm-1 attributed to C=O band increased. When modulation frequency is switched to 100Hz, infrared beam is expected to penetrate into deeper layer of coal particle. Applying the phase angle

of 90~45º, decrease in CH peaks was observed, while difference between PAS spectra of oxidized and unoxidized samples scarcely be detected with a phase angle of 0º. This indicates that changes in functional groups caused by oxidation occur only in the vicinity of coal surface.

Oxidized Taiheiyo coal samples were used for cross-sectional observation by microscope with reflective lights. 5~10μm of bright rim was observed on the edge of coal particles. Unoxidized coal did not show this kind of rim. Thus, actual sampling depth of the spectrometer is estimated to around 10μm.

Ion-irradiated coal

Step scan FT-IR/PA spectra of ion irradiated coal measured with various modulation frequencies and phase angles are shown in Figure 4. PA spectra of untreated Taiheiyo coal obtained at the same FT-IR settings are used as background. In the spectra recorded with 400Hz of modulation frequency, peaks at 2800~3050cm-1 and 1700cm-1 obviously decreased indicating dehydrogenation and decarbonylation occurred during ion irradiation. On the other hand, changes in functional groups is scarcely detected when modulation frequency is set to 100Hz with a phase angle of 45º and below. According to the results of ion irradiation on metal surface, layer with a thickness of 1μm should be treated. Effects of ion irradiation on coal may be different and penetration depth is expected to deeper than 1μm in the case of coal. The spectra of ion treated coal seems to be consistent with the estimation from the oxidation experiment and microscopic observation of Taiheiyo coal.

Gasification char

A Taiheiyo coal char and a Muswellbrook coal char produced by HYCOL entrained flow gasifier are used for the IR measurement. No obvious absorbance peaks could be detected on the surface by the conventional FT-IR spectroscopy. In Figure 5, depth profiling FT-IR/PA spectra are shown. For better baseline correction, spectra of the char collected at the same time in different two places (cyclones CY-301 and 302) during the operation of HYCOL gasifier are mutually compared. Using step scan speed as slow as 10Hz to allow IR beam to penetrate deeply inside char, peaks at 2900cm-1, attributed to CH, and broad peaks centered at 1700 and 3400cm-1 could be clearly detected. These peaks directly indicate that some organic part including oxygen containing functional groups still remain inside the char particle after being processed at high temperature up to 1600ºC. Two kinds of chars showed different depth profile. It is reported that almost all Taiheiyo char is categorized as network or Lacy type and Muswellbrook chars are mainly thick and thin walled balloon type[5]. Depth profile may reflect the difference of morphology of respective chars.

CONCLUSIONS

Step scan FT-IR/photoacoustic spectroscopy (PAS) was used for depth profiling of coal and gasification char particles. Phase modulation on the interferometer and phase separation at the detector, by a lock-in amplifier, and a variety of modulation frequencies and phase angles were used. The results showed considerably different spectra with depth of the coal. Sampling depth was estimated to ca 10μm by comparing the depth profiling spectra and cross-sectional microscopic observation of oxidized coal. Depth profiling of char obtained from HYCOL gasifier indicated the existence of an organic structure inside char particle. Considering that no obvious absorbance peaks could be detected by the conventional FT-IR spectroscopy, the use of step scan FT-IR/PAS is concluded to be a promising method for the analyses of even high temperature gasification chars as well as coals.

ACKNOWLEDGEMENT

REFERENCES

1)   D. W. Vidrine, 'Fourier Transform Infrared Spectroscopy', (Ed. J. R. Ferraro and L. J. Basile) Vol. 3, Academic Press, N.Y., (1982).
2)   D. W. Vidrine, Appl. Spectrosc., 1980, 34, 314.

3) K. H. Michaelian, Appl. Spectrosc., 1989, 43, 214 ; 1991, 45, 302.
4) R. M. Dittmar, J. L. Chao, and R. A. Palmer, Appl. Spectrosc., 1991, 45, 1104.
5) Matsuoka, H., Muramatsu, T., Nakanouchi, T., Sano, K., Fukushima, S., Tsujiguchi, S., and Koyama, S., Proc. 11th Annual International Pittsburgh Coal Canference, 1994, 2, 1316.
6) O. Yamada, Journal of NIRE, 1993, 2, 513.

Table 1   Results of oxidation of Miike coal [a]

Run	Time	O_2react [b]	Gaseous products / mmol					Analyses of oxidized coal		
	/ h	/ mmol	H_2O	CO	CO_2	CH_4	C_{2+}	O_2abs[c] /wt%	C%[d]	H%[d]
1	26	5.62	3.42	0.16	0.46	~ 0	~ 0	0.54	81.5	6.20
2	51	10.54	4.55	0.35	1.11	~ 0	~ 0	1.07	81.2	6.17
3	124	17.69	10.23	0.63	1.66	0.01	~ 0	1.79	80.6	6.08
4	384	25.17	15.14	0.99	2.63	0.01	~ 0	2.36	79.9	6.02

a) 20g of coal was used. Reaction temp: 100°C   b) The amount of oxygen reacted with 20g of coal.
c) The amount of oxygen absorbed in coal.   d) Ultimate analysis data, daf basis.
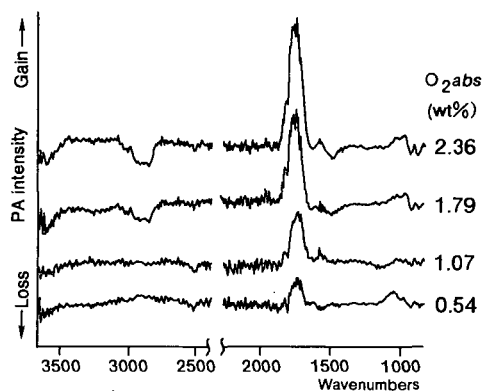

Figure 1   Photoacoustic spectra of oxidized Miike coal recorded at 2.5kHz(rapid scan mode). Spectrum of unoxidized Miike coal is used as background.
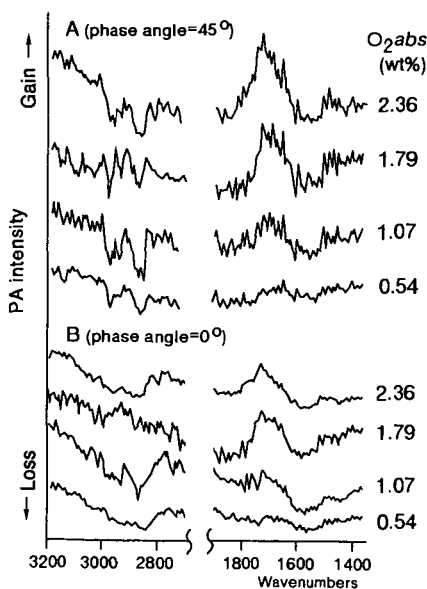

Figure 2   Step scan FT-IR/PA spectra of oxidized Miike coal measured with step scan/phase modulation freq.= 50/400Hz. Spectrum of unoxidized Miike coal is used as background.
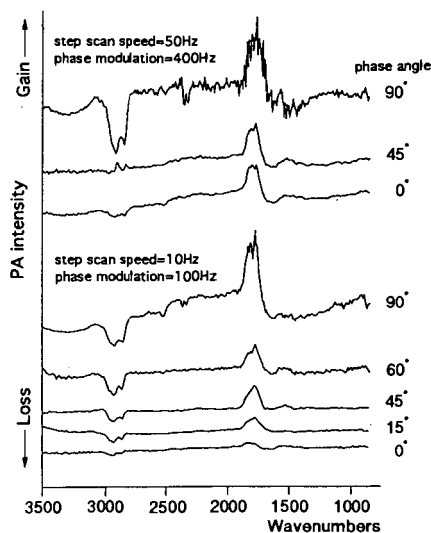
Figure 3   Depth profiling FT-IR/PA spectra of oxidized Taiheiyo coal. Spectrum of unoxidized Taiheiyo coal is used as background.
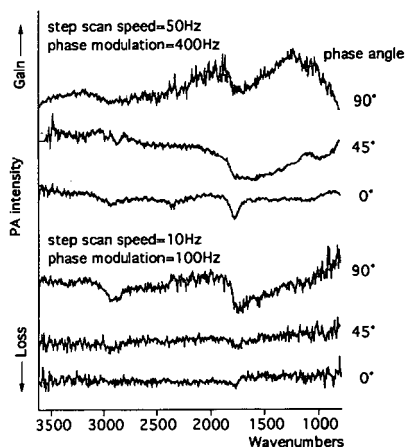

Figure 4   Depth profiling FT-IR/PA spectra of ion-irradiated Taiheiyo coal. Spectrum of untreated coal is used as background.
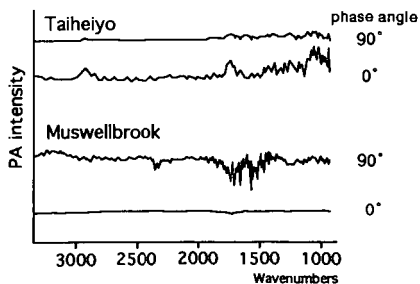

Figure 5   Depth profiling FT-IR/PA spectra of gasification chars obtained from HYCOL gasifier measured with step scan/phase modulation freq.= 10/100Hz.

THE EFFECT OF CHAR "AGE" ON GASIFICATION REACTIVITY

L. Zhang, J.M. Calo, and W. Lu
Chemical Engineering Program
Division of Engineering
Brown University
Providence, Rhode Island 02912, U.S.A.

Keywords: Reactivity; char "age"; thermal desorption methods.

INTRODUCTION
It is well known that, *ceteris paribus,* the overall gasification rate decreases with increasing pyrolysis severity [e.g., 1-7]. This effect can be attributed to various sources, including the loss of heteroatoms and annealing processes. All these types of processes affect the active site density of a char which is an important factor in determining its reactivity. In the current communication, we investigate the relationship between populations of oxygen surface complexes, which form on these sites, and char reactivity as a function of char "age."

EXPERIMENTAL
The char samples used in the current experiments were produced from Wyodak subbituminous coal samples obtained from the Argonne Premium Coal Sample Bank [8], and a phenol-formaldehyde resin synthesized in our laboratory. The latter material was used as a prototype of a non-mineral matter containing char.

Char samples were produced in a tube furnace in flowing ultrahigh purity helium at various ultimate temperatures for two hours. Variation in char "age" was achieved by pyrolyzing samples at temperatures of 900, 950, 1000°C for resin char, and 1000, 1050, and 1100°C for Wyodak char, respectively, for two hours.

All the oxidation and thermal desorption experiments were carried out in the TPD-MS/TGA apparatus. For gasification, the samples were exposed to one atmosphere of carbon dioxide at a selected temperature to a desired burn-off. The thermal desorptions were all carried out at a heating rate of 50K/min to 1200°C in ultrahigh purity helium carrier gas [9].

RESULTS AND DISCUSSION
Reactivities. As expected, the reactivities of the resin and Wyodak coal char samples all decrease monotonically with increasing pyrolysis temperature; i.e., the "younger" chars are more reactive than the "older" chars. Apparent activation energies, determined from Arrhenius plots, are presented in Table I. As shown, these values are well within the range reported by other workers (e.g., [6,7]) for different types of chars and carbons. These results suggest that the apparent activation energies of the "younger" chars are less than for the "older" chars, but only slightly so; certainly not enough to explain the significant differences in observed reactivities.

TPD Spectra. CO TPD spectra from CO_2-gasified Wyodak coal char samples as a function of pyrolysis temperature are presented in Figure 1. As shown, the broad desorption peak is centered at about 950°C. The total amount of oxygen surface complexes decreases with char "age", but not homogeneously over the entire TPD spectrum. That is, the higher temperature surface complexes fall off more rapidly with "age" than the lower temperature complexes. In fact, the low temperature complex population in Figure 1 is practically invariant with char "age."

Figure 2 presents the corresponding data for resin the char samples. The same qualitative behavior is readily apparent, although the desorption is peaked at a higher temperature of about 1010°C. In addition, the total amount of oxygen surface complexes is about a factor of three or so less than for the Wyodak coal char samples. Just as for the Wyodak coal char, the "younger" char samples exhibit a greater amount of CO evolution than the "older" char samples, and the decrease in the population of oxygen surface complexes is not homogeneous over the entire TPD spectrum; the higher temperature population falls off more rapidly than that at lower temperatures. However, somewhat larger differences are apparent in the low temperature region than in the corresponding Wyodak coal char spectra.

Distributions of Desorption Activation Energies. The observation that the population of oxygen surface complexes does not decrease evenly over the entire TPD spectrum suggests that the char surface exhibits a distribution of desorption activation energies. Du *et al.* [10] and Calo and Hall [11] developed distributed activation energy models for the desorption of oxygen surface complexes from carbons following O_2 and CO_2 gasification. In the current work, the distribution of desorption activation energies was calculated using the method described by Calo and Hall [11]. The relationship between the instantaneous CO desorption rate and the distribution of desorption activation energies can be expressed as:

$$d[CO]/dt = [C-O]_o S(E^*) dE^*/dt \qquad [1]$$

where E^* is the local desorption activation energy, as approximated by an instantaneous step at energy E^*, $S(E^*)$ is the desorption activation energy probability density function, $d[CO]/dt$ is the desorption rate of oxygen surface complexes as CO during TPD, and $[C-O]_o$ is the total initial (i.e.

prior to the initiation of desorption) amount of CO-evolving oxygen surface complexes on the surface. Based on the classical work of Redhead [12], the parameters are related by:

$$E*/RT = \ln [\upsilon_o T/\beta] - 3.64 \qquad [2]$$

which holds for for $10^8 < \upsilon_o/\beta < 10^{13}$ (K^{-1}), where υ_o is the pre-exponential factor for the desorption rate constant, T is the temperature, and β is the heating rate. Since a TPD experiment gives the instantaneous desorption rate directly, and $dE*/dt$ can be obtained from Eq. [2], the distribution of desorption activation energies, $[C-O]_o S(E)*$, can be determined from Eq. [1].

The value of the pre-exponential factor, υ_o, was assumed to be constant. A series of TPD runs was performed at various heating rates from 25K/min to 100K/min for the same oxidized char samples. It was determined that a value of $\upsilon_o = 10^{10}$ min^{-1} yielded the best fit in that it produced essentially the same energetic distribution for all the heating rates. This proved to be the best value for both resin and Wyodak char. Consequently, this value was used for the determination of the distributions of desorption activation energies.

Figure 3 presents a comparison of desorption activation energy distributions determined for Wyodak coal char pyrolyzed at various temperatures. As shown, as the pyrolysis temperature decreases, the desorption activation energy distribution of the char also changes. A similar trend was also found for resin char, as shown in Figure 4. In comparison to the Wyodak coal char distributions, the energetic distributions for resin char samples are shifted to higher energies. It is noted that mineral matter (most probably calcium) in the Wyodak coal char plays a significant role in determining the population of the low temperature surface complexes which turn over most rapidly during gasification. The absolute amount of the low temperature oxygen surface complexes is considerably greater for Wyodak coal char than for resin char, which contains no mineral matter. Therefore the mineral matter in the Wyodak coal char preferentially catalyzes the formation of low desorption activation energy surface complexes. This represents the basis of the catalytic effect in this char. This is the principal reason that the reactivity of Wyodak coal char is significantly greater than that for resin char even at lower gasification temperatures.

Mean Desorption Activation Energies and Active Site Concentrations. Two important parameters that can be used to characterize reactivity are the apparent mean concentration of active sites and the average desorption activation energy. For conditions where the gasification rate is desorption rate-controlled, the reactivity can be correlated using the distribution of desorption activation energies. This is accomplished by integrating the desorption rate over the entire distribution:

$$r = \int_0^\infty \upsilon_o \exp(-E*/RT) [C-O]_o S(E*)dE* \qquad [3]$$

In order to address the issue of the rate-controlling step in the current work, the following types of experiments were performed. Following gasification, samples were rapidly quenched to room temperature in either pure helium or CO_2. This was done to assess whether or not the surface was saturated with oxygen surface complexes at gasification conditions. It was reasoned that if the gasification reaction was not controlled by the desorption step, unoccupied active sites would exist which by cooling in the reactant would form additional oxygen surface complexes as the temperature decreased. Consequently, the resultant TPD spectra would differ from those obtained following rapid quenching in helium. From such experiments it was found that gasification of both resin and Wyodak coal char in one atmosphere of CO_2 is desorption rate-controlled under the current experimental conditions [13].

Equating the gasification rate expression for a single mean activation energy, E_d, with that described by a continuous distribution, as in Eq. [3], yields:

$$C_t \exp(-E_d/RT) = \int_0^\infty \exp(-E*/RT) [C-O]_o S(E*)dE* \qquad [4]$$

Figures 5 and 6 present the apparent mean active site concentration, C_t, calculated from Eq. [4], as a function of pyrolysis temperature for Wyodak coal char and resin char, respectively. These plots show that the mean active site concentration decreases as the pyrolysis temperature of the char samples increases. This result means that a "younger" char effectively has more active sites than an "older" char on a per unit mass basis. A similar conclusion has been reported by other workers (e.g.,[3,6,7]) Since gasification occurs at active sites on which oxygen surface complexes are formed, a char with a higher active site concentration at low desorption activation energies will exhibit a greater reaction rate.

The mean desorption activation energies determined from Eq. [4] are presented in Table I. As shown, they are almost constant with "age" for both resin and Wyodak coal chars. These values of mean desorption activation energies are similar to the apparent values determined from the reactivity measurements. They are also quite close to that reported for CO_2 gasification of a PVC char by Hüttinger and Nill [14]. It is clear that there is relatively little effect of char "age" on the mean desorption activation energy. Rather, the reactivity is controlled primarily by the active site

concentration, especially at the lower activation energies in the distribution. In a way, this is similar to the catalytic effect of metals and mineral matter on carbon gasification. That is, the catalytic effect in carbon gasification is predominantly an increase in the number of effective sites rather than the more typical catalytic effect of decreasing the effective activation energy.

SUMMARY· AND CONCLUSIONS
The objective of this work was to explore the relationship among char "age", CO_2 reactivity, and thermal desorption techniques. The results indicate that the major influence of char "age" for the samples investigated is the concentration of active carbon sites, which is greater for the "younger" chars than for the "older" chars. There is little apparent effect of char "age" on the mean desorption activation energy. Comparisons of the apparent activation energies from reactivity measurements with those obtained from analysis of the desorption activation energy distributions show reasonably good agreement, which suggests that reactivities of both chars in one atmosphere of CO_2 at the temperatures investigated are desorption rate-controlled.

It was determined that both chars exhibit energetically heterogeneous surfaces for all the samples examined. For these chars, the distribution of desorption activation energies can be determined from TPD desorption spectra. Prediction/correlation of reactivities from the desorption activation energy distribution was shown to be feasible for the carbon-CO_2 reaction operating under desorption rate-controlled conditions for both resin and Wyodak coal char over the range of char "ages" investigated.

It is noted that we have found very similar behavior for steam-gasified chars as a function of char "age" [15].

ACKNOWLEDGEMENT

REFERENCES
1. Jenkins,R.G., Nandi,S.P., Walker,Jr P.L. *Fuel* **52**, 288 (1973).
2. Johnson, J.L., *Kinetics of Coal Gasification*, Wiley, NY, 1979.
3. Suuberg, E.M., M. Wójtowicz, and J.M. Calo, *Carbon* **27**, 431 (1989).
4. Radovic, L.R., Walker,Jr., P.L., Jenkins,R.G., *Fuel* **62**, 849 (1983).
5. Miura, K. and Hashimoto, K., and Silveston, P.L., *Fuel* **68**, 1461 (1989).
6. Calemma, . and Radovic, L.R., *Fuel* **70**, 1027 (1991).
7. Rodriguez-Mirasol, J., Cordero, T., and Rodriguez, J.J., *Carbon* **31**, 1, 53, (1993).
8. Vorres, K.S., Users Handbook for the Argonne Premium Coal Samples, ANL/PCSP-93/1, DOE, Argonne, Il, 1993.
9. Zhang, L., *Ph.D. Dissertation*, Division of Engineering, Brown University, 1995.
10. Du, Z., A.F. Sarofim, and J.P. Longwell, *Energy & Fuels* **4**, 296 (1990).
11. Calo, J.M. and P.J. Hall, in *Fundamental Issues in the Control of Carbon Gasification Reactivity*, J. Lahaye and P. Ehrburger, eds, NATO ASI Series, Series E: Applied Sciences, Vol. 192, p. 329, Kluwer Academic Publishers, Dordrecht, 1991.
12. Redhead, P.A., *Vacuum* **12**, 203 (1962).
13. Zhang, L., *Ph.D. Dissertation*, Division of Engineering, Brown University, 1995.
14. Hüttinger, K. and Nill, J.S., *Carbon* **28**, 4, 457, (1990).
15. Calo, J.M. and W. Lu, *Proc. Carbon '95*, University of California, San Diego, p. 546, 1995.

Table I. **Mean activation energies as a function of char "age" for Wyodak coal and resin chars, as determined from reactivities and distributions of desorption activation energies.**

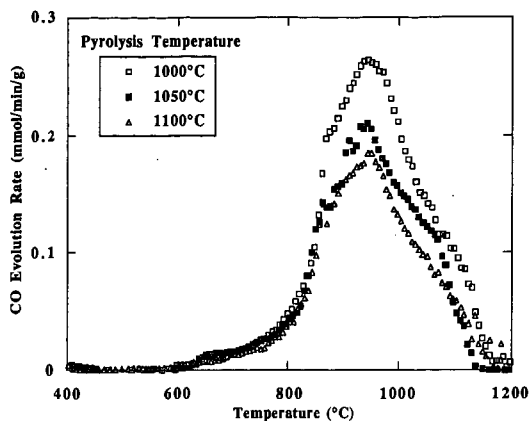| Wyodak Coal Char			Resin Char		
Pyrolysis Temperature (°C)	Mean Activation Energy (kJ/mol) (Reactivity)	Mean Activation Energy (kJ/mol) (Desorption)	Pyrolysis Temperature (°C)	Mean Activation Energy (kJ/mol) (Reactivity)	Mean Activation Energy (kJ/mol) (Desorption)
1000	214	211	900	195	234
1050	233	212	950	207	237
1100	243	212	1000	230	238

Figure 1. The effect of pyrolysis temperature on CO TPD spectra (50K/min) of Wyodak coal char gasified in 1 atm of CO_2 at 825°C to 20% burn-off.
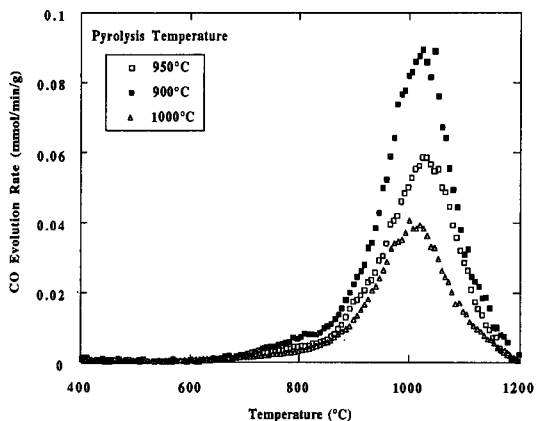

Figure 2. The effect of pyrolysis temperature on CO TPD spectra (50K/min) of resin char gasified in 1 atm of CO_2 at 890°C to 5% burn-off.
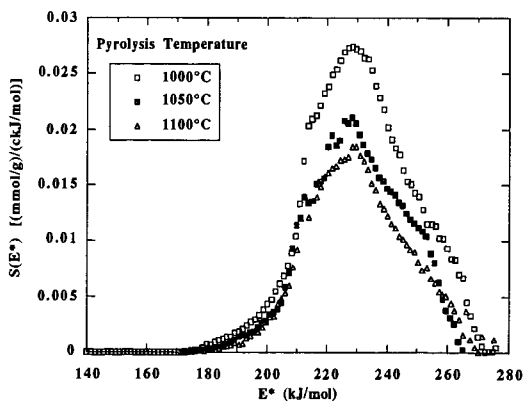

Figure 3. Comparison of desorption activation energy distributions for Wyodak char pyrolyzed at various temperatures and gasified in 1 atm of CO_2 at 825°C to 20% burn-off.
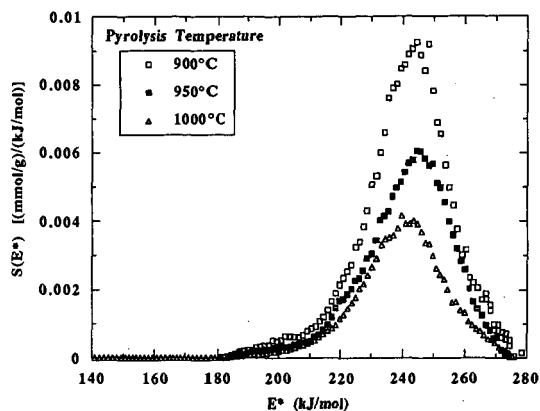
Figure 4. Comparison of desorption activation energy distributions for resin char pyrolyzed at various temperatures and gasified in 1 atm of CO_2 at 890°C to 5% burn-off.
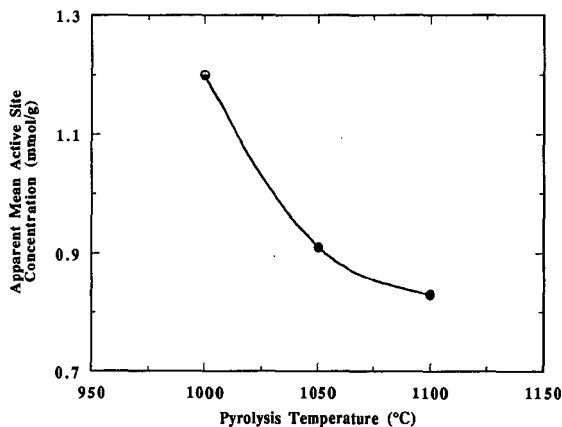

Figure 5. Apparent mean active site concentration as a function of pyrolysis temperature for Wyodak char gasified in 1 atm of CO_2 at 825°C to 20% burn-off.
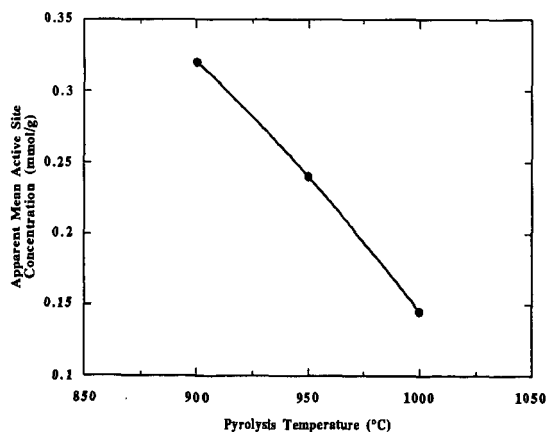

Figure 6. Apparent mean active site concentration as a function of pyrolysis temperature for resin char gasified in 1 atm of CO_2 at 890°C to 5% burn-off.

THE ROLE OF CARBONIZATION IN THE EVOLUTION
OF COAL CHAR GASIFICATION REACTIVITY

Osvalda Senneca, Paola Russo, Piero Salatino
Dipartimento di Ingegneria Chimica - Università *Federico II* di Napoli
Istituto di Ricerche sulla Combustione - C.N.R.
Piazzale V. Tecchio - 80125 Napoli (Italy)

Keywords: carbon gasification, annealing, reactivity.

INTRODUCTION

The relevance of thermal annealing of coals to the physico-chemical properties of the residual coke or char has been often addressed in the literature. The emphasis is most frequently on the structural modifications induced by carbonization in relation to mechanical properties. More limited and sparse information is available on the influence of the severity of pyrolysis and of carbonization conditions on the reactivity of chars in the context of coal gasification.

Thermal annealing affects char gasification along two paths: on one side it induces reordering of the turbostratic structure of coals, on the other side it affects the activity and distribution of mineral inclusions. Both processes lead to char deactivation, their relative importance being dependent on the nature of the parent coal.

In this paper the effect of thermal annealing on the reactivity of char from bituminous coal in carbon dioxide atmospheres is investigated. Experimental results are interpreted in the light of a simple reaction model.

MODEL DEVELOPMENT

The effect of thermal annealing on the reactivity of chars with carbon dioxide is afforded in a simplified manner. The detail of the individual processes that occur during thermal annealing is not considered: the whole spectrum of phenomena, including catalyst deactivation and carbon structure reordering, is lumped into a single deactivation step.

It is assumed that before thermal annealing only carbon of type A is present. Along heat treatment carbon A transforms into a less reactive carbon, B. This is at the origin of deactivation. The two types of carbon, A and B, may be thought as differing by degree of graphitization, catalytic activity or pore structure.

The kinetic model is based on a triangular network of reactions:

Gaseous products

(1) ⟋ ⟍ *(3)*

Annealing (2)

Untreated char, A   **Heat treated char, B**
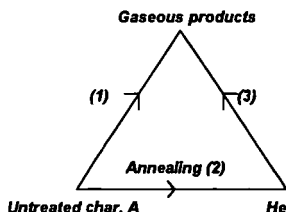
(1) the heterogeneous reaction of char A;
(2) thermal annealing transforming A into B;
(3) the heterogeneous reaction of char B. This reaction is slower than reaction (1).

The following simplifying hypotheses are made:
i.   all reactions are irreversible;
ii. all reactions are activated by temperature according to an Arrhenius type expression;
iii. the kinetics of reactions (1) and (3) is first order with respect to the mass of A and B respectively;
iv. the kinetics of reactions (1) and (3) is first order with respect to the concentration of the gaseous reactant (CO_2);
v.   the annealing process (2) is influenced neither by the gaseous atmosphere, nor by pressure;
vi. the annealing process (2) is irreversible;
vii. the kinetics of the annealing process (2) is first order with respect to the mass of A.

At a given temperature mass balances for chars of type A and B are as follows:

$$1) \quad -\frac{dm_A}{dt} = m_A \cdot k_A \cdot p_{CO2} + k_{A \to B} \cdot m_A$$

$$2) \quad -\frac{dm_B}{dt} = m_B \cdot k_B \cdot p_{CO2} - k_{A \to B} \cdot m_A$$

Initial conditions:
t=0
$$m_{A0} + m_{B0} = w_0$$
$$m_{A0} = w_0 \cdot \exp(-k_{A \to B} \cdot t_{HT})$$

where m_A, m_B are the mass of type A and type B char, w_0 is the initial total mass of char, k_A, k_B are the rate constants for the heterogeneous reaction of type A and B char respectively, p_{co2} is carbon dioxide partial pressure, and $k_{A \to B}$ is the rate constant for the annealing reaction .

Initial conditions take into account the possibility that heat treatment under inert atmosphere occurred for a time tHT, prior to gasification.

The reaction rate at zero carbon burn-off, expressed as the rate of change of carbon conversion degree, f, is given by:

$$3)\left[-\frac{df}{dt}\right]_0 = k_A \cdot p_{CO_2} \cdot \exp(-k_{A \to B} \cdot t_{HT}) + k_B \cdot p_{CO_2} \cdot (1 - \exp(-k_{A \to B} \cdot t_{HT}))$$

At higher burn-off, solution of the system of equations (1)+(2), with the assigned initial conditions, yields the following expression for the instantaneous carbon gasification rate:

$$4)\left[-\frac{df}{dt}\right]_r = k_B \cdot p_{CO_2} \cdot \left(1 - \frac{m_{A0}}{w_0} + \frac{m_{A0}}{w_0} \cdot \frac{1}{1 + \frac{k_A \cdot p_{CO_2}}{k_{A \to B}} - \frac{k_B \cdot p_{CO_2}}{k_{A \to B}}}\right) \cdot \exp(-k_B \cdot p_{CO_2} \cdot t) +$$

$$+\frac{m_{A0}}{w_0} \cdot \left(k_A \cdot p_{CO_2} + k_{A \to B}\right) \cdot \left(1 - \frac{1}{1 + \frac{k_A \cdot p_{CO_2}}{k_{A \to B}} - \frac{k_B \cdot p_{CO_2}}{k_{A \to B}}}\right) \cdot \exp((k_A p_{CO_2} + k_{A \to B}) \cdot t)$$

It can be noted that the reaction rate at any burn-off is a function of the duration of heat pre-treatment (tHT) and is parametric in the value of the three kinetic constants, k_A, k_B and $k_{A \to B}$.

The basic approach of the proposed model resembles that of a former one by Nagle and Strickland-Constable (NSC) (8). Formulated in 1961 to describe the oxidation of pyro-graphite at high flow rates, pressures of 0.2 atm, temperatures comprised between 1050 and 1700°C, the NSC model took after the theory of Blyholder, Bindford and Eyring (9) and assumed that two sites are present on the carbon surface, namely A, a more reactive one, and B, a less reactive one. Two heterogeneous reactions and one reaction of annealing were also considered, but their network differed from the one proposed in the present work. In particular the mass fraction of A was treated under a pseudo-steady state approximation.

EXPERIMENTAL

Experimental work has been focused on the gasification of chars with carbon dioxide. It has been directed to the evaluation of model parameters (kinetic constants for reactions (1), (2), and (3)), and to comparison with model predictions.
Samples of South African (SA) coal, ground and sieved to the size range of 75-125 µm, have been carbonized in inert atmosphere at 900°C for different times, comprised between 1 and 300 min. Heat treated chars have, then, been checked for reactivity with CO_2 under standard conditions.
Heat treatment was performed isothermally in a PL-TG1000M thermobalance after heating up the sample at a rate of 999°C/min. The thermobalance operated at atmospheric pressure with a 50 ml/min flow of nitrogen.
Standard reactivity tests were carried out isothermally in the thermogravimetric apparatus at 900°C and atmospheric pressure, with a 50 ml/min flow of carbon dioxide. Reaction rates have been expressed as rate of change of carbon conversion degree throughout the paper.

RESULTS

Experimental results
The dependence of the instantaneous reaction rate df/dt on carbon burn-off, f is shown in figure 1. Data are relative to SA coal heat treated at 900°C for different tHT. Notably, reaction rate corresponding to different tHT converge at f>0.55. The interpretation of these curves is deferred until *Model results and validation*.
The effect of tHT on char reactivity at 0% burn-off is reported in figure 2 for char heat treated at 900°C for tHT comprised between 1 and 300 min. Reaction rates at 0% burn-off have been evaluated from df/dt versus f curves of figure 1 by linear extrapolation of data up to 10% burn-off.
A non linear decrease of initial char reactivity with duration of heat treatment is observed.

Evaluation of model parameters

Model parameters have been evaluated from reactivities of samples heat treated at 900°C for different tHT.

The reaction rate constants of the heterogeneous reactions of type A and B char have been evaluated from df/dt versus f curves of samples heat treated for 1 and 300 min respectively (fig.1). The rate constant k_A has been assumed equal to the extrapolation to 0% burn-off of the first curve, using data points corresponding to 0<f<0.1; the rate constant k_B, instead, has been based on the extrapolation to 0% burn-off of the second curve, using data points corresponding to f >0.65.

The annealing constant has been evaluated from instantaneous reaction rates at 0% burn-off of samples heat-treated for different tHT (fig.2). On the basis of equation (3) of the model, once the rate constants k_A and k_B are known, regression analysis of data in figure 2 yields the annealing constant $k_{A \to B}$. Accordingly, $k_{A \to B}$ turns out to be about 0.02 min^{-1}. The best fit curve through the data is reported in fig. 2.

Model results and validation

Figure 1 compares computed profiles of gasification rate versus burn-off with those obtained in experiments using different tHT. Fair agreement of model prediction with experimental data is observed. It can be noted that at f<0.55 reaction rates are higher and fall off quicker, the shorter the heat-treatment, while at f>0.55 curves corresponding to different tHT converge, and reactivity appears no longer influenced by the duration of heat-treatment.

The convergence of curves relative to different tHT can be explained considering that in the first stage both annealing of carbon A, and char oxidation are active at the same time, whereas, once carbon A is depleted, oxidation of carbon B remains the main process active.

Notably, the occurrence of gradual transition from the reactivity of char A to that of char B, rather than a stepwise drop of reaction rate, is a consequence of the fact that the time scale over which annealing takes place at 900°C is comparable with those of the heterogeneous reactions 1) and 3). On the contrary, the pseudo-steady state approximation invoked by the NSC model implied that a stationary value of mass fraction of A was reached over a time scale much shorter than that of the gasification reaction.

On account of the closeness of annealing and gasification time scales at temperatures around 900°C, it can be argued whether annealing is the key factor for the evolution of char reactivity throughout conversion.

DISCUSSION

A rough order of magnitude evaluation of the time scale of the annealing process as compared with those of reactions with oxygen and carbon dioxide over a wide range of temperatures will be attempted in the following.

A kinetic constant of annealing of 0.02 min^{-1} has been evaluated at 900°C in this work. Accordingly the time required to transform the 95% of mass A into B would be approximately 140 min. Estimates of time scales of annealing at different temperatures are directly or indirectly provided in a number of papers (1,3,7). All these points have been located in the diagram of figure 3, reporting the process time scale versus reciprocal absolute temperature.

The solid line in figure 3 has been simply obtained by extrapolation to different temperatures of the annealing time evaluated in the present work at 900°C. The activation energy value of 97000 cal/mol has been used in the extrapolation. This value is that suggested by NSC and lies within the broad range of activation energies for annealing proposed in the literature (between 20000 (2) and 200000 (9) cal/mol).

The analysis is pursued further by comparing the time scale of annealing with those of the C-O$_2$ and C-CO$_2$ reactions.

In figure 3 a characteristic time of reaction, defined as the inverse of the reaction rate (df/dt)$_{f=0}$, is also plotted as a function of 1/T. Plots are relative to heterogeneous gasification of SA char with carbon dioxide and with oxygen in air, and have been obtained from extrapolation of experimental data at 1173K (10) and 693K (11) respectively. Activation energies suggested by Salatino et al. (10) and D'Amore et. al (11) (45000 cal/mol for reaction with carbon dioxide and 29000 cal/mol for reaction with oxygen) have been assumed.

The limitations of the comparison afforded in figure 3 lie, on one side, in the considerable uncertainty as regards the activation energy of annealing, and, on the other side, in the inadequacy of extrapolations of intrinsic kinetic data to temperatures where diffusion resistances may be relevant. Being aware of all the above approximations, it can be speculated that: at temperatures lower than 1173 K the rate of annealing is lower than the rate of reaction with both CO$_2$ and O$_2$. At about 1800K the time of annealing and the time of reaction with oxygen are comparable, as Davis et al. (7) found experimentally, and both are shorter than the time of reaction with carbon dioxide. At temperatures typical of entrained coal gasification processes (>1800K) the time scale of thermal annealing should be shorter than the time-scale of both gasification reactions considered: under these conditions, neglecting annealing when estimating reaction rates for entrained coal gasification processes may lead to serious overestimation.

CONCLUSIONS

A very simple approach has been undertaken to clarify the interactions between annealing and gasification reactions. A model based on a triangular network of reactions shows some ability to match experimental reactivity profiles over the entire range of carbon burn-offs.
A pronounced effect of the heat treatment of coal on the reactivity of its char towards CO_2 has been observed at the temperature of 900°C. Under the experimental conditions investigated thermal annealing occurs over time scales comparable with those of gasification reactions.

REFERENCES

1) Blake, J.H., Bopp, G.R., Jones, J.F., Miller, M.G., Tambo, W., *Fuel* **46** 115-125 (1967);
2) Blackwood, J.D., Cullis, B.D., McCarthy, D.J., *Aust. J. Chem.* **20** 1561-70 (1967);
3) Radovic, L.R., Walker, P.L. jr., Jenkins, R.G., *Fuel* **62** 849-56 (1983);
4) Kasaoka, S., Sakata,Y. and Shimada, *Fuel* **66** 697-701 (1987);
5) Sahu, R., Levendis, Y.A., Flagan, R.C., *Fuel* **67** 275-283 (1988);
6) Marsh, H., Diez, M.A., Kuo, K., in *Fundamental Issues in Control of Carbon Gasification Reactivity*, (J. Lahaye and P. Ehrburger, Eds), Kluwer Academic, Dordrecht, pp 205-220 (1991);
7) Davis K.A., Hurt, R.H., Yang, N.Y.C, Headley, T.J., *Combust. Flame* **100** 31-40 (1995);
8) Nagle, J., Strickland-Constable, R.F., *Proc. of Fifth Conf. Carbon*, Vol. 1, Pergamon Press, New York, pp 154-164 (1963);
9) Blyholder, G., Binford, J.S. jr., Eyring, H., *J. Phys. Chem.* **62**, 263-267 (1958);
10) Salatino, P., Senneca, O., Masi, S., A kinetic similarity analysis of the gasification of a coal char by oxygen and carbon dioxide, submitted for publication;
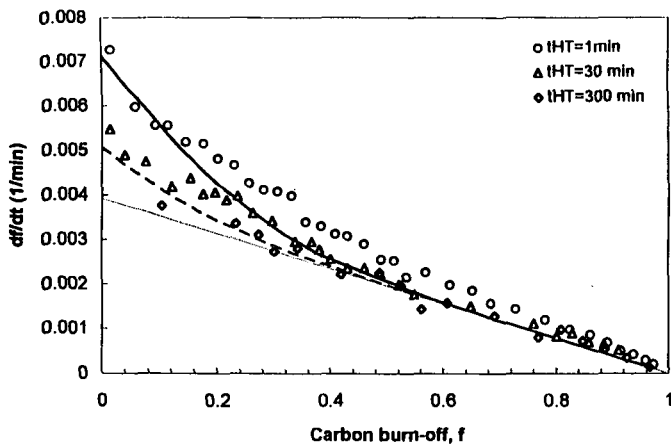11) D'Amore, M., Masi, S., Salatino, P., *Combust.Sci.Tech.*, **63,** 63-73 (1989).

Fig.1 Reaction rate of SA char versus burn-off for HTT=900C and different tHTs.
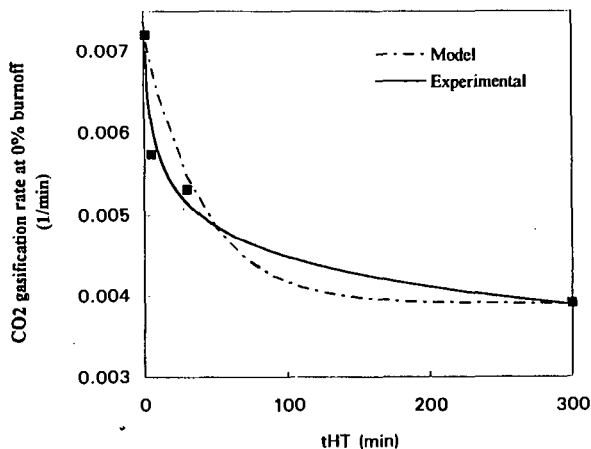Lines represent model results

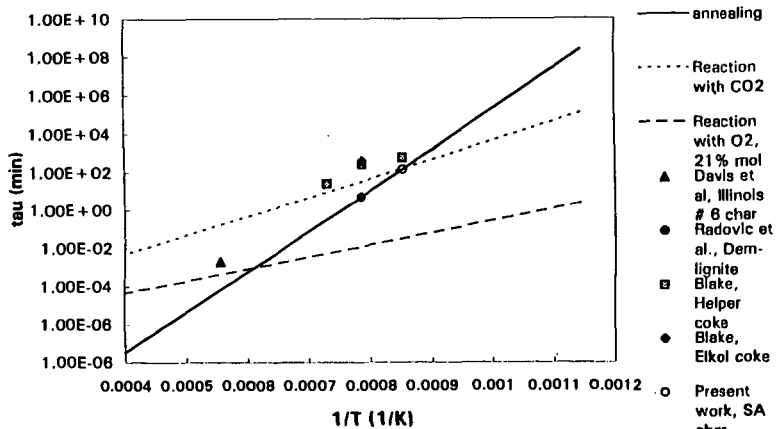Fig. 2 Effect of tHT on reactivity at 0 % burn-off of SA char treated at 900C

Fig. 3 Characteristic times and comparison of experimental data from different authors.

THE MECHANISM OF OXIDATION OF FULLERENES WITH MOLECULAR OXYGEN

M. Wohlers, A. Bauer, Th. Belz,Th. Rühle,Th. Schedel-Niedrig, R. Schlögl
Fritz Haber Institut der Max Planck Gesellschaft
Faradayweg 4-6, D-14195 Berlin, FAX -4930-8413-4401

INTRODUCTION

The novel allotrope of carbon, fullerene is a molecular analogue to the other form of sp^2 hybridised carbon, graphite. In our general attempt to understand the carbon-oxygen reaction at an atomic level we use fullerenes as reference compounds in oxidation studies as they will not exhibit influences of electronic defects on the reactivity. The van der Waals crystals of C_{60} and of C_{70} can be prepared by slow sublimation with single crystalline quality and in absence of any detectable phase impurity due to the molecular separation procedures for the sublimation precursors. It is equally convenient to work on thin films of fullerenes on e.g. silicon (100) surfaces, on large single crystals and on sublimed powder.

Solid fullerenes are air-sensitive materials. They degrade quickly within minutes into a stage of reduced solubility and become eventually fully polymerised upon air/sunlight exposure at 300 K(1). This property is reminiscent on coal degradation, a process in which a variety of gases are released at low rates. We first investigate this initial step of reactivity of fullerenes with air using temperature-programmed methods.

Upon thermal treatment gasification sets in at 573 K with a steep increase in rate at 720 K (2). We will investigate the steps of oxygen activation and fullerene attack in this window of low reactivity by FT-IR , by X-ray absorption spectroscopy and by XPS.

The pattern of gasification in temperature-programmed TG-MS experiments will be compared for the C_{60} fullerene and several other carbon materials in order to evaluate on the validity of the fullerene oxidation as model for the graphite oxidation reaction.

Intercalation of oxygen into the octahedral voids of C_{60} crystals was found to proceed without oxygen dissociation at 300 K (3). The process was described as being reversible at 300 K. Polymerisation of C_{60} at 300 K was observed to proceed to 80% in seven days under oxygen containing 2.6 % ozone (4). Photo-oxidation at 300 K was investigated with a thin film of C_{60}. An intermediate di-carbonyl structure of a fullerene dioxide was suggested based upon an IR absorption at 1750 cm-1. A second broad absorption at 1000 cm-1 remained largely unexplained (5).

High-temperature oxidation of C_{60} was found to begin at 525 K. IR bands at 1780 cm-1 were assigned to cyclic anhydrides, a second feature at 1590 cm-1 to isolated C=C double bonds. Additional discrete peaks at 1102 cm-1, 1037 cm-1 and 958 cm-1 which are superimposed on a broad intense background remained unassigned (6). The possible presence of the fullerene monoxide as epoxide structure can be ruled out on the basis of the absence of its single intense fingerprint peak at 867 cm-1. The reactivity of fullerenes and graphitic carbons against oxidation in air was studied with kinetic methods (7). Several batches of C_{60} showed different quantitative reaction behaviour but produced all a mixture of CO and CO_2 in a two-peak reaction profile centred around 730 K. A significant weight uptake in oxygen of 0.73 mole oxygen per mole fullerene was detected at lower temperature than the reaction onset occurred. Intercalation of CO_2 during attempts to determine the surface area was observed whereas dinitrogen did not intercalate. We have previously studied the interaction of oxygen with fullerenes using a variety of methods. The correlation of these data with kinetic observations is described in a recent review paper (8).The present work contains new results which are based upon the observation that the pre-history of the material plays an essential role in its gas-solid interface chemistry. Contrary to the basic expectations, the defect structure of the molecular crystal controls the intercalation of gases into the void system of the crystal and pre-determines the low-temperature reaction to oxygen-adduct precursors and controls the degradation of the molecular crystal by oxidative polymerisation. For this reason, even air-exposure for minutes causes irreversible damage to a fullerene crystal and generates an ill-defined initial status for a reaction experiment. All sample preparation and fullerene manipulation was carried out with freshly sublimed material in a glove box with a controlled level of less than 1.0 ppm of oxygenate contamination. This treatment gave quantitatively reproducible data with no differences in characteristic parameters between sample batches and minimised the weight uptake prior to oxidation. In this way characteristic differences between C_{60} and C_{70} became apparent as the different fullerene structures cause differences in reactivity which are smaller, however, than the spread in properties due to ill-defined materials. The air-induced degradation destroys the molecular nature of the fullerene crystal first before more obvious effects like the accumulation of oxides can be detected spectroscopically.

RESULTS

INTERCALATION OF OXYGEN

Clean fullerenes were transferred in a TDS apparatus and exposed in-situ for 24 h to synthetic air at ambient pressure. The results of the following TDS are shown in Figure 1 for the two fullerenes. The

two experiments first show that both fullerenes can intercalate a large amount of Ar during storage at 300 K. They further intercalate oxygen which replaces partly the Ar during exposure to air at 300 K. Furthermore, the oxygen reacts with the carbon skeleton under formation of labile C-O
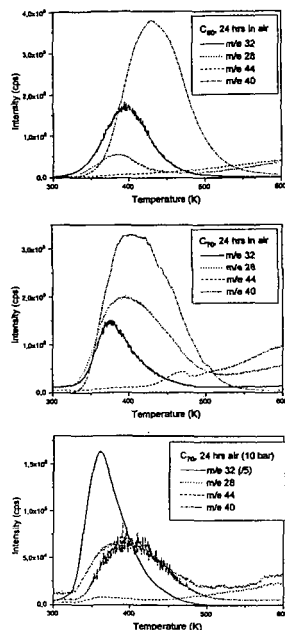

Figure 1. TDS profiles of fullerenes stored under Ar after exposure to air at 300 K and ambient pressure. The linear heating rate was 0.27 K/s. Desorption occurred into UHV. The sample size was with 10 mg identical for both experiments. The experiments were halted at 623 K due to beginning sublimation . The absence of nitrogen under the m/e 28 peak was checked with the absence of an m/e 14 peak. The high pressure experiment (bottom plot) was carried out with a different sample holder and a different sample mass. Note the reduced scale for the m/e 32 peak.

groups or even under formation and intercalation of CO as can be seen from the m/e 28 traces. This reactivity is quite different for the two fullerenes with C_{60} being more stable, as expected from its more „aromatic" and highly symmetric valence electronic structure. Above 450 K both fullerenes react in a thermally activated form with oxygen which was not evolved at 400 K /380 K respectively. This oxygen seems to be present in a more strongly bound and already activated form(epoxide) converting into gasification products at temperatures well below the literature values of gasification activity (2,6,8). The shapes of the desorption profiles indicate different reaction orders caused by the different relevance of bulk diffusion terms on the overall process. The spherical symmetry of C_{60} giving rise to isotropic gas diffusion is more suitable to enclose all gases irrespective of their chemical nature (Ar and di-oxygen), for the uniaxially elongated C_{70} molecule the gas diffusion in its solid is anisotropic but the chemical interaction seems less efficient as evidenced by the lower initial desorption temperature.

The fact that the noble gas desorbs at higher temperatures than the di-oxygen can be accounted for by the different location in the crystal. The oxygen is intercalated in an outer shell of each crystal, the Ar evolves from the inner core. In addition, it has to penetrate the damaged regions of the fullerene crystals which occur as consequence of the partial gasification. As the precursor to the gasification is molecularily disperse, this reaction is not topotactic and attacks every molecule within the shell of intercalation. A large number of partly oxidised molecules with dangling bonds and reactive C=C fragments will remain which can stabilise themselves by polymerisation into a three-dimensional network of non-planar basic structural units. In the presence of oxygen these defective fullerenes are activated precursor structures for enhanced gasification.

Raising the total pressure of air to 10 bars causes the reaction front to move deeper into each crystal This is illustrated for C_{70} where the di-oxygen desorption occurs at the same position but with a much higher intensity than after exposure at one bar. The „noise" on the Ar trace indicates the eruptions of the gas protruding through the now dense solid-solid reaction interface between oxidised and intact fullerene. It is noted that the fraction of di-oxygen which is activated to cause gasification is not changed by the total pressure which only increased the abundance of molecular oxygen intercalated.

In all these experiments the evolution of CO_2 is low but begins exactly with the evolution of di-oxygen. This indicates that only few fullerene molecules are more deeply oxidised than to the carbonyl stage. The fact that in all experiments a rise in the CO_2 partial pressure above 500 K is observed, indicates that a second process of oxidation requiring a higher thermal activation occurs and that a significant amount of oxygen which does not recombine to di-oxygen, resides within the fullerene crystals. It was verified that this sequence of events is independent of the optimised low heating rate.

The observation that C_{60} holds gas molecules more strongly than C_{70} was verified in a static experiment proving the ability of the system to intercalate molecular CO in the same way as molecular oxygen. Ar-loaded fullerenes were degassed with He at 573 K in-situ in a high pressure DRIFTS cell and exposed to 5 bar CO at 400 K for 1h. Both intercalated species show a red shift (2125 cm-1) to the gas phase (2170.21 cm-1) and C_{60} an extra shift of 5% which is in the expected order of magnitude according to the TDS experiments. This experiment is a chemical probe for the overall weak bonding interaction between fullerene host and diatomic guest molecules.

ELECTRONIC STRUCTURE OF OXO-INTERMEDIATES

Photoemission and photoabsorption with tuneable excitation wavelengths were used to study the chemical bonding of the intermediates causing the CO emission at 370-400 K and the enhanced CO_2 emission at 570 K. The valence band electronic structure of both fullerenes is characterised by a sequence of well-resolved molecular states which were probed with 100 eV excitation energy to
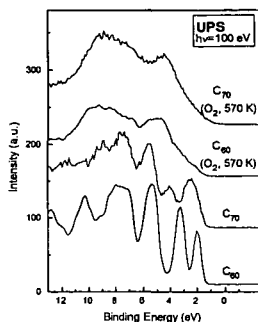
Figure 2: Valence band spectra of fullerene films in their pristine state and after oxidation at 570 K in 500 mbar oxygen (in-situ experiments). The data were recorded at the SX700 1 beamline at the BESSY synchrotron. The Fermi edge was calibrated with a gold sample.

ensure a minimum cross section modulation of σ and π states. This situation is not drastically altered upon intercalation of oxygen at 300 K and heating up to 400 K where already significant chemical reactivity was detected by the bulk-sensitive TDS technique. This implies that the average surface structure is containing up to 400 K still a large abundance of intact fullerene molecules. As can be seen in Figure 2, the surface undergoes complete restructuring upon heating to 570 K and transforms into a polymer structure with extended electronic states characterised by a resonance at 4.6 eV and a broad band around 9.5 eV. These peaks are not those of graphite (2.8 eV and 7.5 eV) but belong to oxygenated (O2p emission at 4.6 eV) partly unsaturated carbon-carbon bond systems. The corresponding C 1s XPS data show three structures at 285. 6 eV for the carbon-carbon skeleton (not graphitic, would be at 284.6 eV) and at 287.1 eV and 289.2 eV for oxygen-carbon single and double bonds. This classifies the chemical reaction leading to CO emission as a process creating mainly defective molecules such as holey fullerene cages with some oxygen functionalities at the empty co-ordination sites. Further thermal treatment is required to remove the C-O functions under CO_2 evolution and to create free carbon co-ordination sites which are saturated by homo-polymerisation with either intact molecules (they act as electrophilic unsaturated entities) or with neighbouring damaged cages. The abundance of oxygen functionalities is larger on C_{70} than on C_{60} although both species give rise to exactly the same spectral positions indicating the close similarity of the chemical bonding.

The modified reactivity of oxygen at different temperatures should be reflected in different chemical bonding of the oxygen precursors which must be present in a more reactive form at 370 K than at 570 K. X-ray absorption spectroscopy is well-suited to prove this as it is element-specific and offers high chemical selectivity. The discrimination of the chemical structure of the oxygen precursors at the two temperatures is shown in Figure 3. At 370 K a species with oxygen single bonds well-compatible with an epoxide (but no peroxide) or an ether structure is detected. The characteristic feature for this is the low intensity of the π^* resonance indicating the hybridisation/occupation of these states. At 570 K the oxygen is bonded via double bonds as can be seen from the now prominent π^* resonance at 532 eV.
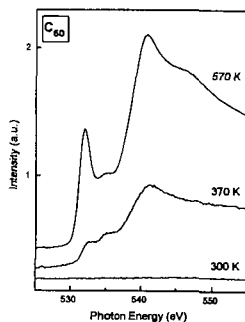
Figure 3: X-ray absorption spectra at the O 1s edge of C_{60} films oxidised at 370 K and 570 K in 500 mbar oxygen for 10 h each. The absence of any detectable oxygen after exposure of the film at 300 K indicates that the chemical bonding of intercalated molecular oxygen was too weak to prevent desorption of the surface-near layers in the UHV of the spectroscopy experiment.

DYNAMICS OF THE OXIDATION

In-situ DRIFTS spectroscopy was used to investigate the participation of the two oxo-intermediates in steady state reaction. The lowest possible temperature at which steady state conversion occurred with both fullerenes was 570 K. At this temperature the samples were exposed to 250 ml/min synthetic air and spectra were recorded as difference spectra to the initial state. In previous experiments it was shown that also at 470 K the formation of additional IR absorptions around 750 cm-1 and 1000 cm-1 occurred which is in agreement with the formation of carbon-oxygen insertion precursor compounds. The data in Figure 4 provide clear evidence for the formation of several oxygen-containing intermediates which are present under steady state oxidation. The low temperature was chosen to allow sufficient data to be accumulated for verification of the steady state. The spectra indicate the same functional groups to be formed than detected in a recent study of oxidised carbon blacks (9). The spectral quality is, however, much better in the present case due to the detection of in-situ spectra (without intermitting the oxidation process and without dilution of the carbon materials).

We observe a split carbonyl band around 1750 cm-1 indicating the presence of other C=O groups besides the cyclic anhydrides for which the high frequency of the absorption is characteristic. The 1580 cm-1 band for isolated double bonds is very prominent and occurs in both fullerenes with the
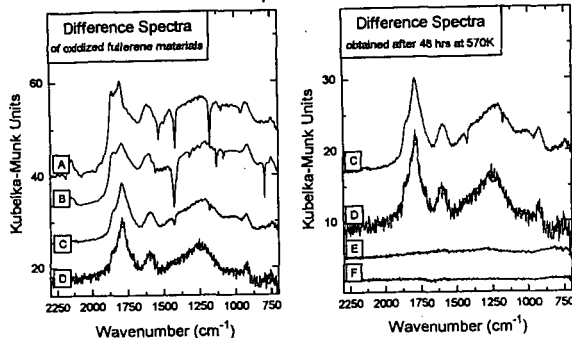
Figure 4: DRIFTS spectra of several fullerene and carbon materials during in-situ oxidation at 570 K. The left panel reports difference spectra after 20 h on stream, the right panel after 48 h oxidation. The burn-off was after 48 h below 10%. Samples were: $A=C_{60}$, $B=C_{70}$, C=fullerene black raw, D= fullerene black after extraction of solubles with toluene, E= activated carbon Norit A, F= graphitic electrode deposit (nanotubes).

same intensity irrespective of the quite different initial electronic structure. The negative sharp bands arise from the loss of molecular fullerene abundance in the gasifying samples. We note that in the non-extracted fullerene black the molecular fullerenes are oxidised preferentially over the other carbon as the bands of C_{60} occur as negative pattern. The molecular bands are superimposed on a broad structure peaking at 1000 cm-1, which was observed in all oxidation studies of fullerenes (6,8) and with oxidised carbon blacks (9). C-O single bond features and the fingerprints of C-C overlap here with high frequency aromatic substitution bands. Such bands occur further at lower frequencies of about 900 cm-1 and 750 cm-1. All these features were also detected in the carbon black oxidation study (9) and are discussed there with respect to the previous literature. The perfect agreement of the spectral features between all materials with nominally only sp^2 bonding clearly reveals that the reaction mechanism detected in detail for the model compounds of fullerenes should qualitatively apply for planar sp^2 carbon materials.

GASIFICATION OF FULLERENES

Temperature-programmed gasification data were obtained from TG-MS experiments in synthetic air (250 ml/min, 5K/min heating ramp). The results for C_{60} are displayed in Figure 5.
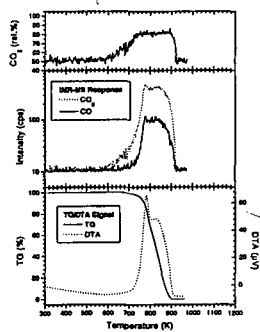

Figure 5: Combined TG-MS gasification experiment of 2.5 mg C_{60} in synthetic air. A horizontal sample pan with a specially directed gas supply and a high throughput ensured the absence of mass transport limitations. A special mass-spectrometer of the IMR-MS type allows to monitor the selectivity without interference with detection of molecular nitrogen and without fragmentation overlap. Note the log ordinate in the MS response plot. The weight uptake before gasification is low due to the high crystal quality of the material which was not air-exposed prior to the gasification experiment.

The gas evolution curve indicates the onset of gasification at 570 K in agreement with the data of Figure 1 (2,6). The selectivity changes in the initial stages of low-temperature oxidation which are dominated by the reaction of precursor compounds. Their abundance is with high-quality crystals so low that the weight uptake of less than 2% between 470 K and 570K is not visible in the overall weight change pattern. Contrary to the reaction pattern for all planar carbon samples which gasified under our experimental conditions all in a double-peak fashion with a slower initial rate and an accelerated second main reaction, the C_{60} fullerene gasifies also in a two-step sequence (7) but with an accelerated initial event. This is taken as indication for the action of the accumulated precursor compounds which leave a large number of defective fullerene molecules after cage-opening oxidation steps. The DTG curve (not shown) reveals that about 20 % of the total mass burns with the accelerated rate. This amount of material coincides with the number of molecules in the skin of oxygen penetration under ambient pressure which was shown to exist in the data of Figure 1.

THE REACTION MECHANISM

The observations indicated above and results from kinetic experiments (2,8) can be combined in a sequence of events for the fullerene oxidation. It is pointed out that no qualitative difference was found for the two molecular fullerenes and the DRIFTS data indicated that the mechanism should also apply for other sp^2 carbon materials. A schematic representation is given in Figure 6, for energetic details see ref. (8).
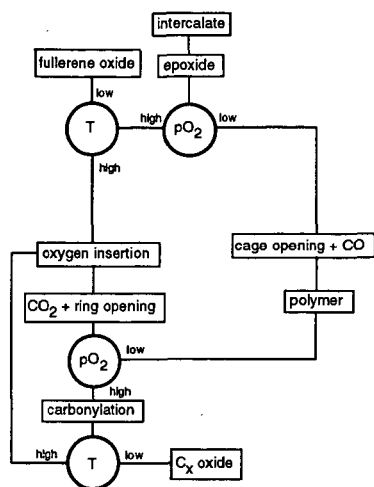
111

Figure 6: Schematic diagram of the sequence of events in fullerene oxidation: The end products besides CO and CO₂ are fullerene oxides, a homopolymer and carbon oxides with defective fullerene structures. The control variables are oxygen partial pressure and temperature.

The reaction starts with an intercalation of molecular oxygen into the van der Waals gaps of the molecular solids. With little thermal activation dissociation occurs and labile epoxides are formed besides activated atomic oxygen which will react with other electrophilic centres on the fullerene molecules. As long as the temperature is kept low (370 K) and the oxygen partial pressure remains present, the epoxides will be retained as fullerene oxides (epoxide or oxygen insertion compound). These materials are, however, not stable and will eventually react under ring opening and CO evolution to a defective fullerene molecule. Stabilisation of this state will occur at low oxygen pressures by homo-polymerisation. At higher partial pressures oxygen will be inserted in the form of e.g. cyclic anhydrides. Above 470 K these structures will evolve CO_2 and cause ring opening in the already attacked fullerene molecule. Should the oxygen partial pressure be low again (e.g. in TDS experiments, or during thermal processing), stabilisation by polymerisation will occur. At still sufficient partial pressures of oxygen carbonylation of the defective structure (5) will follow which remains as metastable product up to 570 K but which gasifies readily at higher temperatures entering a reaction loop ending with complete combustion (6). The reaction product of a polymer will not occur frequently with planar carbons (pinning defect) but the other products as well as the control variables do also occur with conventional carbon materials. The non-planar bonding geometry of the fullerene surface leads to an accumulation of the metastable intermediate products of carbon oxidation as they are formed at lower temperatures than on planar surfaces. For this reason it was possible to observe these intermediates in convenient abundance (9) for spectroscopic characterisation. At higher temperatures of above 700 K where gasification rates become significant for all carbon materials (7) the abundance of the intermediates will be much reduced also for fullerene carbon. Their ease of formation may, however, affect the overall kinetics detectable in macroscopic gasification experiments (7) as illustrated with Figure 5. The relevance of molecular intercalation of oxygen in graphitic carbon and the eventual localisation in between graphene galleries or at defect sites is currently under study. The higher temperatures required for intercalation in graphitic carbon than for fullerene carbon renders any detection with structural methods difficult as can be estimated from the localisation (10) of the extra oxygen in C_{60}.

In conclusion, the different topologies of curved fullerenes and planar sp^2 carbon cause a different abundance of oxo-intermediate compounds at low reaction temperatures. The higher chemical energy of the curved fullerenes allows for a lower activation energy for intermediate formation as well as the total „internal" surface of the fullerene crystal reacts as compared to the low abundance of reactive prismatic surfaces in planar carbon. High quality spectra were accessible for the intermediates allowing to observe some atomistic details of the carbon oxidation process.

ACKNOWLEDGEMENT

REFERENCES

(1) R. Taylor, J.P. Parsons, A.G. Avent, S.P. Rannard, T.J. Dennis, J.P. Hare, H.W. Kroto, D.R.M. Walton, *Nature, 351,* (1991) 277
(2) H. Werner, M. Wohlers, D. Bublak, J. Blöcker, R. Schlögl, *J. Full. Sci. Technol., 1,* (1993), 457
(3) R.A. Assink, J.E. Schirber, D.A. Loy, B. Morosin, G.A. Carlson, *J.Mater. Res.,7,* (1992), 2136
(4) D. Heyman, L.P.F. Chibante, *Chem. Phys. Lett.,* (1993), 207
(5) C. Taliani, G. Ruani, R. Zamboni, R. Danielli, S. Rossini, V.N. Denisov, V.M. Burlakov, F. Negri, *J. Chem. Soc., Chem. Commun.,* (1993), 220
(6) A.M. Vassallo, L.S.K. Pang, P.A. Cole-Clarke, M.A. Wilson, *J. Am. Chem. Soc., 113* (1991), 1103
(7) I.M.K. Ismail, S.L. Rodgers, *Carbon, 30,* (1992), 229
(8) M. Wohlers, A. Bauer, Th. Rühle, F. Neitzel, H. Werner, R. Schlögl, *J. Full. Sci. Technol.,* (1996), in press
(9) P.E. Fanning, M.A. Vannice, *Carbon,31 ,* (1993), 721
(10) W. Bensch, H. Werner, H. Bartl, R. Schlögl, *J. Chem. Soc., Faraday Trans., 90,* (1994), 2791

PURIFICATION OF CARBON NANOTUBES FROM CATHODE DEPOSIT BY MEANS OF DIFFERENT OXIDATION RATES

F. Ikazaki, K. Uchida, S. Ohshima, Y. Kuriki, K. Yase, S. Yoda and M. Yumura
National Institute of Materials and Chemical Research
1-1 Higashi, Tsukuba, Ibaraki 305 JAPAN

Abstract
    Two purification methods of nanotubes from a cathode deposit by an arc plasma were conducted by means of different oxidation rates of various graphites. One was chemical and the other physical method. Both could purify nanotubes at their optimum conditions. In the former, the catalytic oxidation was used of graphite materials by copper. Copper supported graphite was prepared by the intercalation of copper chloride and by the reduction to metal copper. The catalytic oxidation decomposed the graphite at 773 K and less. The temperature was significantly lower than the oxidation temperature former reported of graphite, which enabled purification. In the latter, dispersion, comminution and filtration of a cathode deposit in ethanol were used to separate coarse graphite. The rate of weight loss by oxidation increased with the decrease of size of the graphite. Nanotubes were more slowly oxidized from the edges than the graphite of the same size. This could purify nanotubes.

1. Introduction

    Carbon nanotubes were first observed by Iijima[1] in cathode deposits produced by an arc plasma method. They are completely novel carbon materials which have the property of either metal or semi-conductor according to the diameter and helical pitch[2]. Carbon nanotubes are also expected to have about two order higher fracture strength than that of commercial carbon fibers due to few defects in carbon crystal structures. Other carbon materials like graphite and amorphous carbon existed together with carbon nanotubes in the cathode deposit. Different from C60, carbon nanotubes are not dissolved in any organic solvent. Carbon nanotubes have to be purified from these carbon materials not only to analyze the properties but also to utilize the unique properties for industrial applications
    Some methods[3]-[6] were proposed for the purification. These methods were based on oxidation methods. But carbon nanotubes and other carbon materials in cathode deposits are not considered that they have much different oxidation rates. Some process was inevitable to enlarge the difference of oxidation rates between carbon nanotubes and the other carbon materials before oxidation. Two such methods were developed in our group; one was chemical,the other physical method.

2. Experimental procedure

2.1 Sample

    In chemical method, graphite powder(Nippon Carbon Co., SAD-4) was used for a model graphite. The diameter ranges from #100 to #325(about 44-149μm). Crude nanotubes, i.e. as-prepared cathode deposits were purchased from Shinku Yakin Co. or were prepared by an arc plasma in our laboratory. The weight percentage of nanotubes contained in the cathode deposit was not known.

2.2 Basic idea of both methods and procedures

    Chemical method   The chemical method is based on the concept that graphite intercalation compounds(GIC) are not synthesized in the case of carbon nanotubes because of the rigid structure of carbon nanotubes. Some metals like copper, molybdenum and so on catalytically oxidize graphite[7] at a rather low temperature. When graphite materials in cathode deposits intercalate such metal, for instance copper, carbon nanotubes are expected to be purified at a rather lower temperature. **Fig.1** is the procedure of chemical purification method. In our experiment copper was selected as a catalyst. Copper chloride-intercalated graphite(CuCl2-GIC) was prepared, followed by the reduction of chloride to metal copper, because copper-intercalated graphite was not obtained directly and chloride-intercalated graphite was stable in the air. Copper chloride-intercalated graphite was reduced either by gas phase containing hydrogen at 773 K for 1 hour or by metal lithium in THF containing naphthalene at room temperature for 1 week. Thus prepared graphite is hereafter called as copper supported graphite.
    Physical method   Basic idea is that the apparent oxidation rate of carbon material depends on the diameter of the material. There were various kinds of carbon materials in as-prepared cathode deposits, some of which were rather coarse graphite particles with lower oxidation rate than carbon nanotubes. Only very small portion of existing carbon nanotubes would survive when the as-prepared cathode deposits containing carbon nanotubes,amorphous carbon and graphite materials, were oxidized all together. Separation process is necessary of rather coarse carbon materials, i.e. coarse graphite from the as-prepared cathode deposit before oxidation process. Schematic procedure of the physical method is shown in **Fig.2**. Dispersion in methanol, classification by centrifugal forces and comminution in methanol of

cathode deposits were utilized to separate graphite particles with larger Stokes' diameter than carbon nanotubes. Then purified carbon nanotubes would be obtained by higher oxidation rate of the cathode deposits with equal and smaller Stokes' diameter than carbon nanotubes.

2.3 Characterization

Particle size distribution was measured by centrifugal settling photoextinction method(Shimadzu SA-CP3).

Thermogravimetric analyzer(Shinku rikou, TGD 9600) measured the oxidation rate of the cathode deposits remaining in each separation step in the physical method and of graphite and copper supported graphite in the chemical method. The sample weight was usually ca. 10 mg, but was ca. 2 mg in the case of the cathode deposit remaining in each separation step in the physical method. Temperature was raised at a rate of 10 K/m.

SEM(Hitachi, S-800 with EDX) was used for observation and element analysis of cathode deposits and of purified carbon nanotubes.

XRD(Philips PW1800) was used to measure the crystal structure of cathode deposit ,graphite,copper chloride-intercalated graphite and copper supported graphite.

Oxidation was also conducted with Thermogravimetric analyzer.

3. Results and discussions

3.1 Chemical method

Copper chloride-intercalated graphite(CuCl2-GIC) and copper supported graphite were identified by XRD profiles as shown in **Fig.3**. Oxidation rate measured by Thermogravimetry (TG.) is depicted in **Fig.4**. Copper supported graphite was oxidized at a considerable rate at the low temperature of 673 K.

Copper particles in the cathode deposits after the reduction by hydrogen seemed a little larger than those by metal lithium. The reduction by metal lithium was therefore considered better for the purification of crude nanotubes.

Oxidation was examined from 673 to 873 K   **Fig.5** shows the photographs at the oxidation temperature of 773 K. Even at the low temperature of 673 K carbon nanotubes could also be purified. The temperature was ca. 350 K lower than that of Ebbesen's method. The chemical method needs some reagents and takes time, but is very easy to be conducted.

3.2 Physical method

Figs 6 and 7 show the particle size distribution and oxidation rate of as-prepared cathode deposit and the cathode deposit remaining in each separation step. Apparent oxidation rate increased with the decrease of the particle size distribution of the remaining cathode deposit. The apparent activation energy also decreased with the decrease of the particle size distribution.

Purified carbon nanotubes are shown in **Fig.8**, which shows this method could separate graphite from the as-prepared cathode deposit. The oxidation temperature of 823 K. The temperature was about 200 K lower than that of Ebbesen's method. One of the defects in this method is rather tedious and needs skill.

4. Conclusion

Two purification methods were proposed of carbon nanotubes from as-prepared cathode deposits;one was chemical, the other physical method. Followings are the results induced.
(1) Both methods purified carbon nanotubes from as-prepared cathode deposit.
(2) The oxidation temperature was greatly lower than that of Ebbesen's method; ca. 350 K in chemical method and 200 K in physical method.
(3) Any process was inevitable to enlarge the difference of oxidation rate between carbon nanotubes and the other carbon materials containing in as-prepared cathode deposit.
(4) Optimization of the two methods is still necessary according to the varying property of as-prepared cathode deposit.

Literature cited
1) Iijima S.; Nature,**354**,56(1991)
2) Tanaka K., Satoh T., Yamabe T., Okahara K., Uchida K.,Yumura M.,Niino H.,
   Ohshima S., Kuriki Y., Yase K. and Ikazaki F.; Chem. Phys. Letters, **223**,65(1994)
3) Ebbesen T.W., Ajayan P.M., Hiura H. and Tanigaki K.; Nature,**367**,519(1994)
4) Uchida K., Yumura M., Ohshima S., Kuriki Y., Yase K. and Ikazaki F.; Chemical
   Engineer(In Japanese),**39**,896(1994)
5)Takarada Y., Morishita K., Yumura M. and Uchida K.; Proc. of 8th Fullerene
   symposium,p253(1995, Kyoto)
6) Ikazaki F., Ohshima S., Uchida K., Kuriki Y., Hayakawa H., Yumura M.,
   Takahashi K. and Tojima K.; Carbon,**32**,1539(1994)
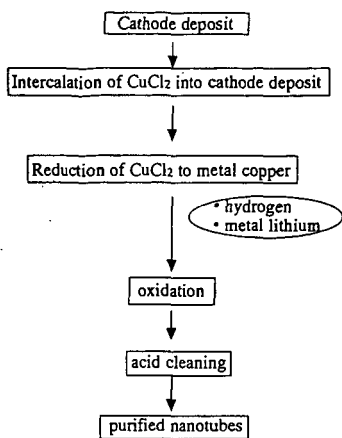7) Baker R.T.K.; Carbon,**24**,715(1986)

```
┌─────────────────┐                    ┌─────────────────┐
│ Cathode deposit │                    │ cathode deposit │
└─────────────────┘                    └─────────────────┘
        │                                      │
┌──────────────────────────────────┐  ┌───────────────────────────────┐
│ Intercalation of CuCl₂ into       │  │ ultrasonic dispersion in      │
│ cathode deposit                   │  │ methanol                      │
└──────────────────────────────────┘  └───────────────────────────────┘
        │                                   B  │
        │                              ┌──────────────┐
        │                              │ decantation  │ ──→ sediment
┌──────────────────────────────────┐  └──────────────┘
│ Reduction of CuCl₂ to metal copper│     C  │
└──────────────────────────────────┘  ┌───────────────────────────────┐
        │         ⟨• hydrogen    ⟩     │ comminution and redispersion  │
        │         ⟨• metal lithium⟩    └───────────────────────────────┘
        │                                      │
        │                              ┌───────────────┐
   ┌───────────┐                       │ centrifugation│ ──→ sediment
   │ oxidation │                       └───────────────┘
   └───────────┘                          D  │
        │                              ┌──────────┐
   ┌──────────────┐                    │ filtration│
   │ acid cleaning│                    └──────────┘
   └──────────────┘                       E  │
        │                              ┌──────────┐
┌──────────────────┐                   │ oxidation│
│ purified nanotubes│                  └──────────┘
└──────────────────┘                       │
                                    ┌──────────────────┐
                                    │ purified nanotubes│
                                    └──────────────────┘
                                          F
```

Fig.1 Procedure of chemical method   Fig.2 Procedure of physical method
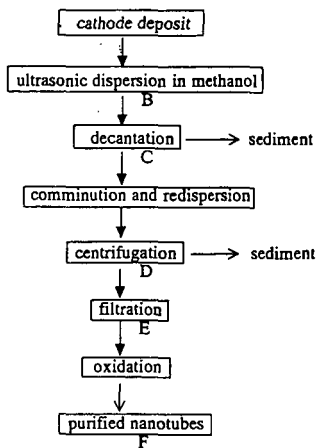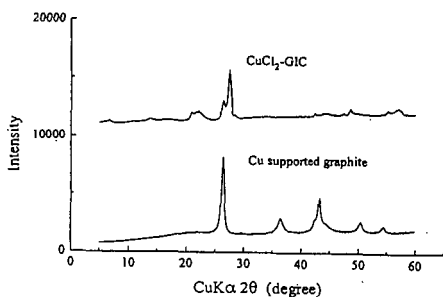
Fig.3 XRD profiles of CuCl$_2$-intercalated graphite and Cu supported graphite
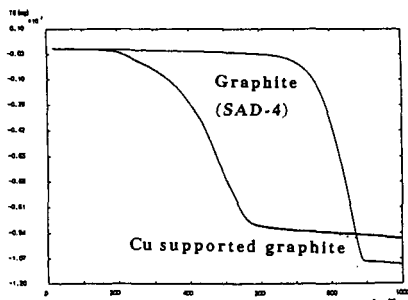
Fig.4 TG analysis of graphite(SAD-4) and Cu supported graphite
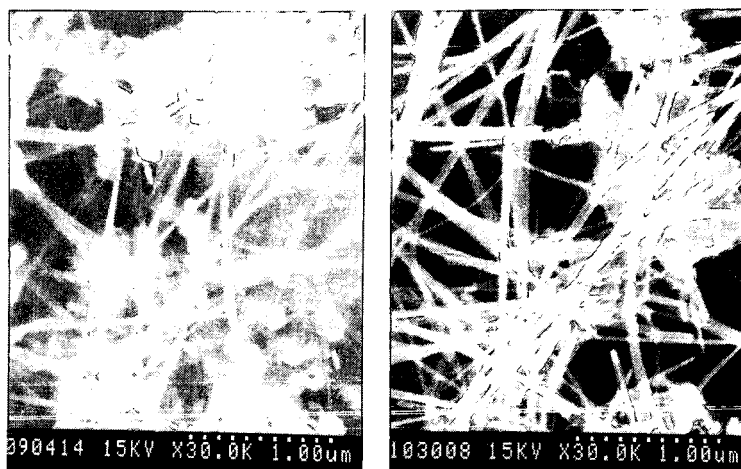
115

Fig.5 SEM photographs at the same position of cathode deposit at the oxidation
temperature of 773 K (left; 773 K 1h, right 773 K 3h in Chemical method)
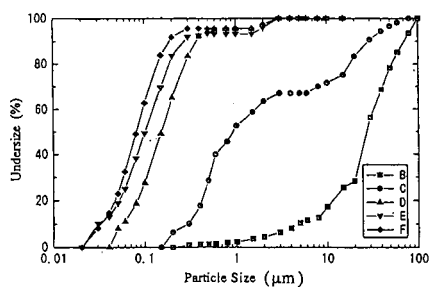

Fig.6 Particle size distribution of cathode deposit remaining in each separation step
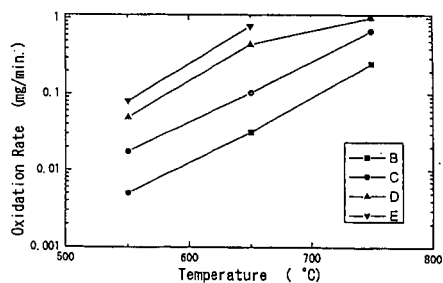of physical method(Symbols(B-F) correspond to the symbols in Fig.2)

Fig.7 Oxidation rate of cathode deposit remaining in each separation step
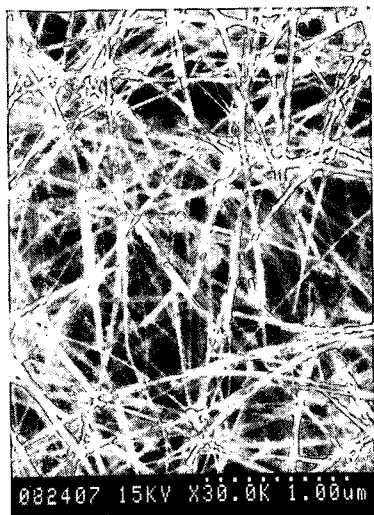of physical method(Symbols(B-E) correspond to the symbols in Fig.2)

Fig.8 SEM photograph of cathode deposit after physical purification method

GASIFICATION OF CARBON NANOTUBE-CONTAINING MATERIAL

K. Morishita and T. Takarada

Faculty of Engineering, Gunma University
1-5-1, Tenjin-cho, Kiryu, Gunma, Japan 376

Introduction

Carbon nanotubes synthesized using arc discharge evaporation method always include graphitic carbon, amorphous carbon and carbon nanoparticles. The purification step is needed to precisely characterize the physical and chemical properties of nanotubes and to study the application of those. Recently, the purification of nanotubes by the gasification with oxygen[1), 2)] or carbon dioxide[3)] was carried out. However, few studies on the mechanisms of gasification of carbon nanotube-containing materials have been reported. In this study, the gasification behaviors of nanotube-containing materials and nanotubes were investigated by fixed point observation techniques with scanning electron microscope (SEM) and transmission electron microscope (TEM).

Experimental

Materials

Samples synthesized by arc-discharge evaporation method (Vacuum Metallurgical Co., ltd., Type-3) in National Institute of Materials and Chemical Research were used. The conditions of synthesis were DC voltage of 18V and He pressure of 500 Torr. An inner black core of the cathode product was picked up. Then, the core was crushed and dispersed in methanol with the use of a sonicator. The sample recovered as a float was used as raw materials in this study.

Gasification

The gasifiation of sample was carried out in a thermo-balance (Shinku Riko; TGD-7000). After evacuation and substitution with N_2 gas, sample was heated up to a desired temperature with N_2 flow. Then, reaction gas was introduced into the reactor and the gasification of sample was initiated. The experimental conditions were as follows : oxygen (1, 10vol%) 773K, 823K, 1023K, 1073K; carbon dioxide (100vol%) 1173K.

SEM and TEM observations

A series of SEM observation and gasification of sample was carried out as follows. The raw materials put on Si wafer was observed with SEM and then set in the thermo-balance. After the sample was gasified for a desired reaction time, the area selected by the previous observation was observed with SEM, again. These procedures were repeated several times. The SEM used was JEOL JSM-5300. In the case of TEM observation, sample was put on copper grid (400mesh). A series of TEM observation and gasification of sample was essenntially similar to the case with SEM mentioned above. TEM observations were carried out using JEOL 1200EX at ACCV of 100kV. In these experiments, more than 10 fields were observed and more than 50 photograghs were taken for each sample. It is very important to observe many fields because microscopic observations are apt to give prejudiced informations.

Results & Discussions

Reactivity

Nanotube-containing materials were gasified in a thermo-balance. Figure 1 shows the gasification profiles obtained under various conditions. The reactivity of sample toward oxygen was so high that about 90wt% of sample was gasified in 5min at conditions of 1023K and 10vol% of oxygen. The activation energy for oxygen gasification was estimated as about 140kJ/mol. The gasification profile of sample in carbon dioxide was somewhat peculiar. The conversion was smoothly increased up to around 70wt%, and the gasification was seemed to be

saturated after that.

Gasification behaviors of nanotube-containing materials

A series of SEM observation and gasification of sample was repeated several times. Figure 2 shows the SEM photographs of raw material and the samples partially gasified. The gasification temperature was 1023K. Besides carbon nanotubes, many large lumps of carbon and many carbon nanoparticles were observed in the raw material. As the reaction progressed, other carbonaceous materials were gradually consumed and only carbon nanotubes were remained at 5min of reaction time. This is due to the difference in the reactivity between carbon nanotubes and other carbon materials. In the course of gasification, many tubes were newly appeared from lumps of carbon materials. Careful observations revealed that not only other carbonaceous materials but also carbon nanotubes were damaged by oxygen gasification. Figure 3 shows the results obtained at 823K. The total conversion was about 90wt%. No remarkable difference in the gasification rate between other carbon materials and nanotubes was observed. Therefore, considerable amount of other carbon materials were remained in the sample gasified. It may safely be said that it is better for the efficient recovery of nanotubes to gasify raw material with oxygen at a high temperature such as 1023K than at a low temperature of 823K. In the case of CO_2 gasification at 1173K, as the reaction progressed, large lumps of carbonaceous materials were gradually gasified just like the case of oxygen gasification. A number of carbon nanoparticles, however, were remained in the sample. Further purification step will be needed.

Gasification behaviors of nanotubes and nanoparticles

To clarify the gasification behaviors of nanotubes and nanoparticles, a series of TEM observation and gasification of sample was repeated several times. The gasification temperature was 1023K. A wide variety of gasification manners of carbon nanotubes were observed. It was often recognized that the gasification of nanotube was initiated from the cracks, defects and strains in nanotubes. Other typical gasification manner was shown in Figure 4. It can be seen that nanotube was gasified from the tip of the tube. This gasification manner was often observed in this study and reported by Tsang et al.[3]. The diameter of tube was reduced from 18nm to 11nm near the tip (point-A) and from 20nm to 15nm at point-B in 5 seconds. From these results, the gasification rate of carbon nanotube is able to be measured directly. A carefull observation showed that the tip angle of closed layer near the cap was enlarged as shown at point-C. Figure 5 shows the gasification manners of tubes and particles. In this field, many nanoparticles were observed as shown in Figure 5a. At 5sec of gasification time, some nanoparticles were considerably damaged and outer layers of some nanotubes were stripped off. Finally, almost all the nanoparticles were gasified at 10sec. The gasification rate of the irregular-shaped particles was higher than that of smooth-faced particles.

Similar experiments were carried out at 823K. The results obtained were shown in Figures 6 and 7. As the reaction progressed, the outer layers were transformed to amorphous and the spacing of the lattice was enlarged (Fig. 6). It was commonly observed that relatively thin tubes just as pointed by arrow in Figure 6 were swelled by the oxidation. The pitting formation by the oxygen gasification was sometimes recognized on the cylindrical outer surface of tubes (Figure 7). As a whole, no obvious difference in the gasification rate between nanotubes and nanoparticles was recognized at 873K. This is consistent with the results obtained with SEM observations.

Conclusions

The gasification behaviors of carbon nanotube-containing materials were clarified by SEM and TEM observations. The gasification rates of other carbonaceous materials were higher than those of nanotubes at 1023K. A wide variety of gasification manners of nanotubes were observed. The gasification manner of nanotubes strongly depended on the gasification temperature.

References

1. P. M. Ajayn et al., *Nature*, **362**, 522 (1993)
2. T. W. Ebbesen et al., *ibid.*, **367**, 519 (1994)
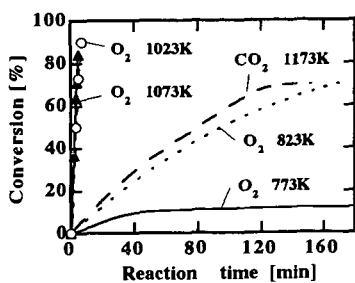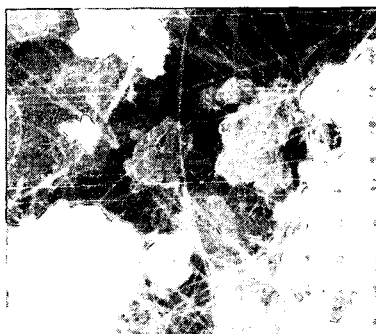3. S. C. Tsang et al., *ibid.*, **362**, 520 (1993)
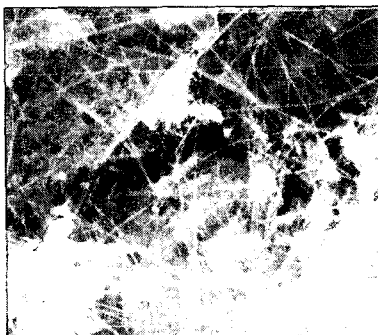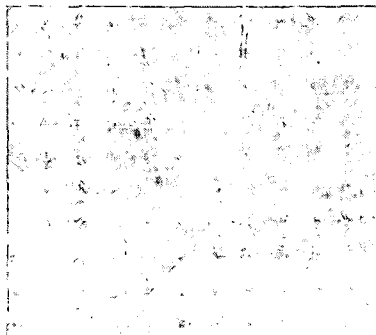
Fig. 1 Reaction profiles of samples

(a)

(b)

(c)

(d)

(e)

1um

Fig. 2 SEM images of samples before and after O_2 gasification at 1023K

(a) raw material
(b) reaction time 0.5 min
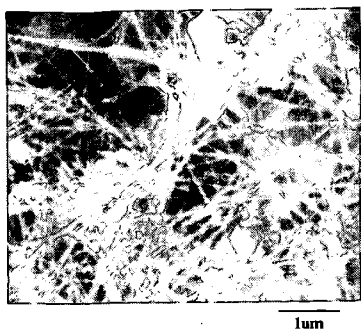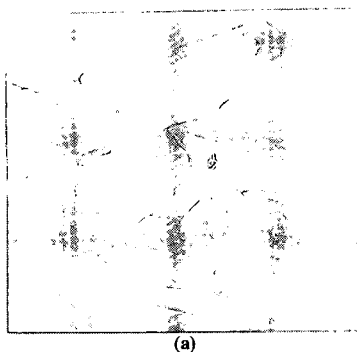(c) reaction time 1 min
(d) reaction time 3 min
(e) reaction time 5 min

120

Fig. 3 SEM image of sample
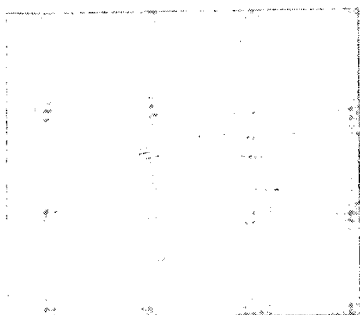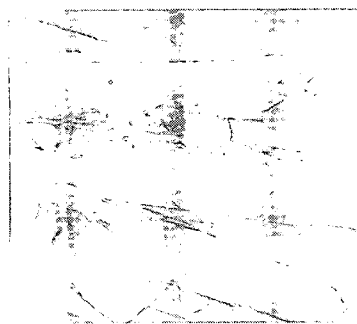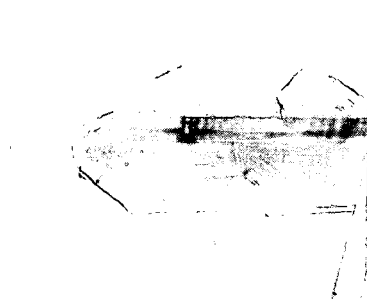after O_2 gasification at 823K
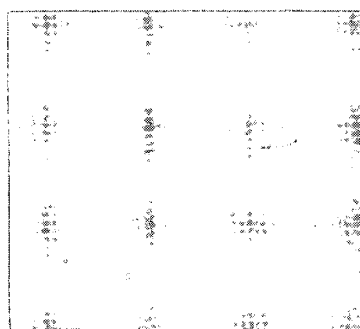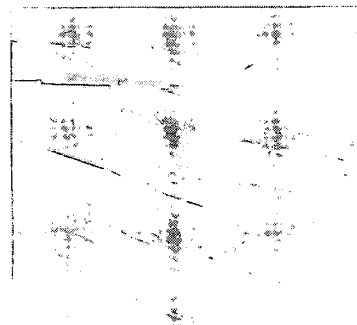
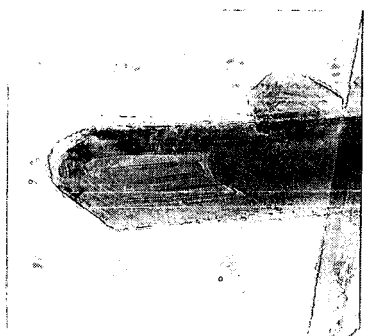Fig. 4 TEM images before and after
O_2 gasification at 1023K

(a)   raw material
(b)   reaction time 5 s

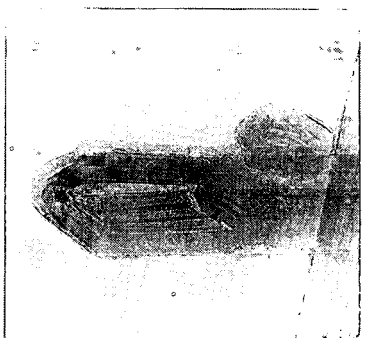Fig. 5 TEM images before and after
O_2 gasification at 1023K

(a)   raw material
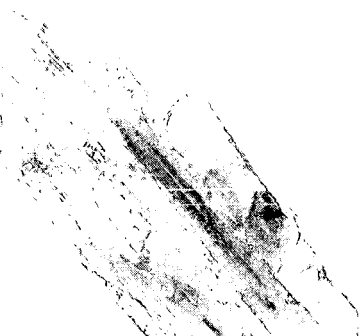(b)   reaction time 5 s
(c)   reaction time 10 s

(a)

(a)

(b)

(b)

(c) 20nm

(c) 20nm

Fig. 6 TEM images of samples before
and after O_2 gasification at 823K
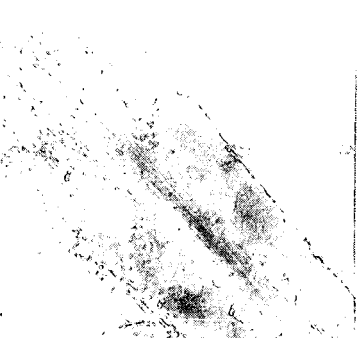
    (a)   raw material
    (b)   reaction time 20 s
    (c)   reaction time 40 s

Fig.7 TEM images of samples before
and after O_2 gasification at 823K

    (a)   raw material
    (b)   reaction time 10 s
    (c)   reaction time 30 s

DETERMINATION OF POROSITY AND POROSITY DEVELOPMENT DURING GASIFICATION FROM THERMAL DESORPTION METHODS

L. Zhang and J.M. Calo
Chemical Engineering Program
Division of Engineering
Brown University
Providence, Rhode Island 02912, U.S.A.

Keywords: Char porosity; porosity development; thermal desorption methods.

INTRODUCTION
In the current work, a new approach is explored for the characterization of porosity and porosity development in carbons and chars. It is shown that there exist both qualitative and quantitative relationships between porosity development and post-reaction desorption features of oxygen surface complexes formed during the activation process. It is proposed to exploit these relationships to develop a porosity characterization method based on the interpretation of post-activation temperature programmed desorption (TPD) spectra.

EXPERIMENTAL
The samples used in the experiments were chars produced from Wyodak subbituminous coal obtained from Argonne Premium Coal Sample Bank [1], and from phenol-formaldehyde resin synthesized in our laboratory. The latter material was used as a prototype of a non-mineral matter containing char. The char samples were produced in a tube furnace at 1000°C for 2h in flowing ultrahigh purity helium.

All the oxidation and thermal desorption experiments were carried out in the TPD-MS/TGA apparatus. For gasification, the samples were exposed to one atmosphere of oxygen at a selected temperature, and burned-off to varying extents. The subsequent thermal desorptions were all carried out at a heating rate of 50K/min to 1200°C in ultrahigh purity helium carrier gas, without exposing the previously oxidized samples to ambient air.

Adsorption isotherms for all the char samples were obtained using a Quantachrome Quantasorb surface area analyzer with nitrogen at 77K.

RESULTS AND DISCUSSION
Char Characterization. The total specific surface area, external surface area, and micropore volume of the samples were determined from the nitrogen isotherm data using the so-called α_s-plot method [2]. This technique is based on a comparison of the shape of the adsorption isotherm of a sample with that of a standard nonporous reference material. The α_s-plot method consists of plotting adsorption normalized to a particular point (typically $p/p° = 0.4$; i.e., $\alpha_s = n/n_{0.4}$) for the reference material *vs.* $p/p°$ to obtain a standard α_s curve. This curve is then used to construct the α_s-plot from the isotherm of the test sample. The slope of the resultant plot at low α_s provides the total surface area; the slope of the upper linear branch gives the nonmicroporous surface area; and the extrapolation of this branch of the curve to $\alpha_s = 0$ provides the total micropore volume. α_s-plots were constructed for all the nitrogen adsorption isotherms for the current samples using data for the standard nonporous carbon proposed by Rodriguez-Reinoso *et al.* [3]. Corresponding surface areas and pore volumes were also obtained *via* comparison with the isotherm for the reference adsorbent given in this reference [3], following the data work-up procedures contained therein.

Wyodak Coal Char. Figures 1 and 2 present the thermal desorption spectra for the Wyodak coal char samples as a function of burn-off. In Figures 3 and 4 the total evolved CO and CO_2 obtained from these figures are compared to the micropore volume and the nonmicroporous surface area, respectively, as determined from the α_s-plots, as described above. It is noted that the CO evolution was "corrected" by subtraction of the CO_2 signal, which is explained subsequently. The nitrogen adsorption data indicate that the total surface area (not shown), the nonmicroporous surface area, and the micropore volume all initially increase with burn-off, pass through maxima around 40% burn-off, and decrease steadily thereafter. This behavior is quite typical of carbonaceous materials [4]. As the burn-off proceeds, the nonmicroporous (i.e., the larger porosity) surface area increases continuously but more rapidly prior to 40% burn-off, and less rapidly at higher degrees of burn-off, as shown in Figure 4. This behavior indicates that the microporosity continues to develop up to about 40% burn-off, and decreases thereafter; while, the larger porosity develops continuously with burn-off. These results are consistent with the classical picture of microporosity development at low conversions, followed by pore wall collapse and concomitant surface area loss at higher conversions [5].The principal point of these figures, however, is that the CO and CO_2 evolution correlate quite well with the micropore volume and the nonmicroporous surface area, respectively.

Resin Char. Summaries of the corresponding data for resin char are presented in Figures 5 and 6. As shown, this char behaves somewhat differently than the Wyodak coal char. The nitrogen adsorption data indicate that the micropore volume increases to a maximum at about 45% burn-off, and decreases thereafter. The nonmicroporous surface area, however, increases steadily and monotonically up to 72% burn-off. It is noted that even though the larger porosity increases with extent of burn-off, the majority of the porosity is still microporous over the entire activation

process. That is, even at 72% burn-off, the surface area contribution from the larger porosity is only about 5% of the total surface area. In any case, as for the Wyodak coal char, the CO and CO_2 evolution correlate quite well with the micropore volume and the nonmicroporous surface area, respectively, in spite of the fact that the CO and CO_2 TPD spectra for resin char (not shown) differ considerably from the Wyodak char spectra, both qualitatively and quantitatively.

Starsinic et al. [6] identified carboxylic acid groups on oxidized carbon surfaces using FTIR spectroscopy, and noted that their concentration increases with extent of burn-off. Otake and Jenkins [7] have shown that the CO_2 complexes present on an air-oxidized char are responsible for the acidic nature of the surface, and that the high temperature CO_2 evolution is primarily due to the thermal decomposition of carboxylic acid anhydride surface complexes. Zhuang et al. [8] have also found that CO_2 evolution arises from the decomposition of lactone and/or acid anhydride complexes, whereas CO desorption is mainly from carbonyl and ether type complexes. In a DRIFTS study of the formation of surface groups on carbon by oxygen, Fanning and Vannice [9] also reported that initial exposure to oxygen produces ether structures, and that additional exposure develops cyclic anhydride groups.

Apparently, just like nitrogen, which penetrates practically all the char porosity (i.e., micro-, meso- and macroporosity) during adsorption measurements, oxygen can also penetrate all the porosity under gasification conditions to form surface complexes over the entire carbon surface. The obvious conclusion that one can draw from the results presented here is that CO evolution occurs from the entire apparent specific surface area, but that most of the CO_2-evolving surface complexes are formed only on the surfaces of the larger porosity. In a study of the effect of nonreacting gases on the desorption of reaction-created surface complexes on carbon, Britten et al. [10] concluded that surface transport processes were involved in the desorption of CO, but that no influence of the nonreactive gases on the CO_2 desorption rate was observed. These results support the conclusion that the CO_2-evolving surface complexes are formed on the surface area in the larger porosity.

From the preceding, it is possible that a large portion of the CO_2 evolution derives from carboxylic acid anhydride complexes. Since the stoichiometry for the thermal decomposition of these groups result in one CO_2 and one CO molecule, the CO evolution was "corrected" by subtracting the CO_2 evolution to account for the CO arising from carboxylic acid anhydride complexes. These are the "corrected" CO values which are plotted in Figures 3 and 5. In both cases, this correction improves the correlation between micropore volume and CO evolution. Therefore, it is concluded that there is some justification to this "correction."

Random Pore Model. In addition to the CO and CO_2 evolution data and the nitrogen adsorption data, the reactivities of the samples as a function of burn-off were also obtained. These latter data were used in conjunction with a random pore model [11] to determine the evolution of the microporosity.

According the random pore model [11], the sample burn-off, x_c, vs.time, t, follows the relationship:

$$[(1/4\pi(1-x_c)dx_c/dt]^2 = A_0 \ln[1/(1-x_c)] + A_1^2 \qquad [1]$$

where $A_0 = B_0 v^2/(2\pi)$, and $A_1^2 = (B_1 v)^2$, and B_0 and B_1 are the zeroth and first order moments of the pore number density function, and v is the velocity with which a pore surface element recedes due to reaction. A_0 and A_1 were determined by least squares regression from plots of Eq. [1] derived from the reactivity data. From these values and the surface area at one point (e.g., 5% burn-off), the parameters B_0, B_1, and v were obtained. The apparent total specific surface area, S, was then determined from:

$$S = 4\pi(1-\varepsilon_{T_0})(B_0 v t + B_1)(1-x_c(t)), \qquad [2]$$

where ε_{T_0} is the initial (i.e., zero burn-off) total void fraction. Comparisons of surface areas obtained from the nitrogen BET data with values calculated from Eq. [2] show very good agreement for both chars.

As indicated by the nitrogen adsorption data, both the resin and the Wyodak coal chars are essentially microporous materials at zero burn-off. A Gaussian pore number distribution for the micropore volume was assumed, following Dubinin et al. [12]. It was also assumed, as in the original random pore model development, that the probability density function of pore numbers does not vary with burn-off. With these assumptions, the following relationships were derived:

$$(1-\varepsilon_{micro})/(1-\varepsilon_{micro})_0 = \exp[-2\pi(B_0(\Delta r)^2 + 2 B_1 \Delta r)] \qquad [3]$$

$$S_{micro} = d(\varepsilon_{micro})/d(\Delta r) = 4\pi(1-\varepsilon_{micro})(B_0 \Delta r + B_1) \qquad [4]$$

where ε_{micro} is the void fraction of the micropores, and Δr is the mean micropore radius change.

For the current data, the micropore void fractions, ε_{micro}, for the two chars as a function of burn-off were determined from nitrogen adsorption data. The mean micropore radius change, Δr, was then determined from Eq. [3], and the total apparent micropore surface area, S_{micro}, was

determined from Eq. [4]. The difference between total surface area and micropore surface area was taken as the nonmicroporous surface area. The agreement between the nonmicroporous surface areas determined in this manner with those obtained from the α_s-plots was quite good. thereby validating this general approach.

Figure 7 shows the results for the mean micropore radius as a function of burn-off for resin and Wyodak coal chars, as determined using this approach. Here the initial mean micropore radius (i.e., prior to gasification) was determined from the zero burn-off nitrogen adsorption data assuming a normal micropore volume distribution. The resultant mean pore radius prior to oxidation was 1.04 nm for Wyodak coal char, and 0.64 nm for resin char. The variance of the normal distribution was 0.24 nm for Wyodak coal char, and 0.18 nm for resin char. These results indicate that the pore size is larger, and the pore distribution is broader for Wyodak coal char than for resin char prior to activation. It is noted that the rate of mean micropore radius decrease with burn-off at high conversion is slower for resin char than for Wyodak coal char. This suggests that the resin char remains more microporous with burn-off. This conclusion is also apparent from the nonmicroporous surface areas for both chars. From these results, it is concluded that the random pore model theory is capable of providing reasonable predictions of microporosity development during gasification for both resin char and Wyodak coal char.

SUMMARY AND CONCLUSIONS
It is concluded that CO-evolving surface complexes are formed over the entire surface area of all the porosity of the two very different chars investigated, and that the total CO evolution upon thermal desorption is well correlated with the total surface area. It is also concluded that the CO evolution "corrected" for the expected contribution from carboxylic acid anhydride surface complexes is well correlated with the microporosity. It is hypothesized that if these observations can be generalized and calibrated, they could be developed into a new method for the characterization of char porosity, in conjunction with the "extended" random pore model.

ACKNOWLEDGEMENT

REFERENCES
1. Vorres, K.S., Users Handbook for the Argonne Premium Coal Samples, ANL/PCSP-93/1, DOE, Argonne, Il, 1993.
2. Gregg, S.J., and Sing, K.S.W., Adsorption, Surface Area, and Porosity, 2nd ed., Academic Press, NY, 1982.
3. Rodriguez-Reinoso, F., Martin-Martinez, J.M., Prado-Burguete, C., and McEnaney, B., *J. Phys. Chem.* **91**, 515 (1987).
4. Walker, P.L. Jr., in *Carbon and Coal Gasification,* Figueiredo, Moulijn, eds., NATO ASI Series, 9.3, 1986.
5. Miura, K. and Hashimoto, K., *IEC Proc. Des. Dev.* **23**, 138-145,1984.
6. Starsinic, M., Taylor, R.L., Walker, P.L., Jr., and Painter, P.C., Carbon 21, 69 (1983).
7. Otake, Y. and Jenkins, R.G., *Carbon* **31**, 109 (1993).
8. Zhuang, Q-L, Kyotani, T., Tomita, A., *Energy and Fuels* **8**, 714, 1994.
9. Fanning, P.E. and Vannice, M.A., *Carbon* **31**, 5, 721, (1993).
10. Britten, J. A., Falconer, J. L. and Brown, L. F., *Carbon* **23**, 627 (1985).
11. Gavalas, G. *AIChE J.* **36**, 577 (1980).
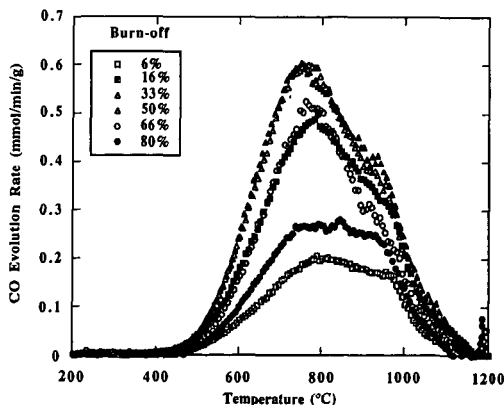12. Dubinin, M. M., *Chemistry and Physics of Carbon*, Vol. 2, Academic, NY, p. 51 (1966).

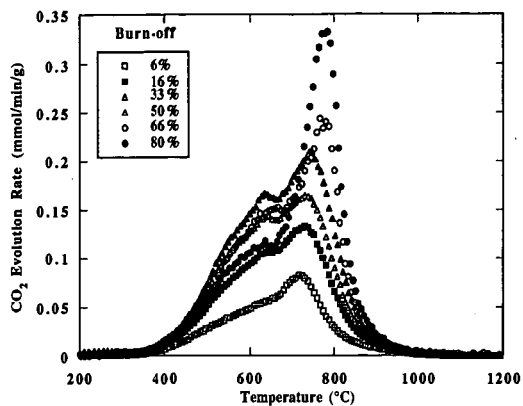Figure 1. 50K/min CO TPD spectra from Wyodak char as a function of burn-off in oxygen

125

Figure 2. 50K/min CO_2 TPD spectra from Wyodak char as a function of burn-off in oxygen (0.1MPa, 420°C).
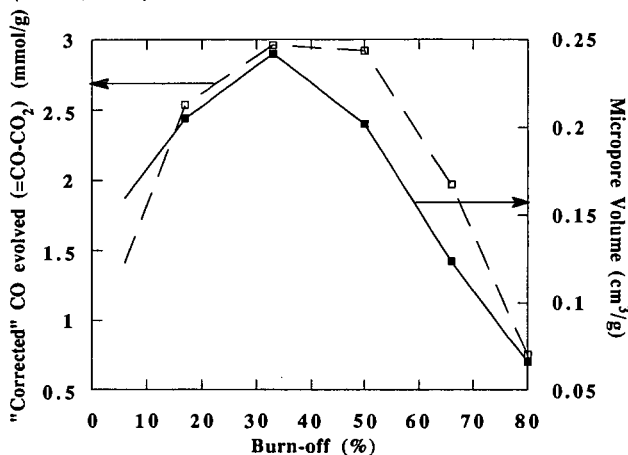

Figure 3. Comparison of total "corrected" CO evolved with micropore volume for Wyodak coal char as a function of burn-off (0.1MPa, 420°C).
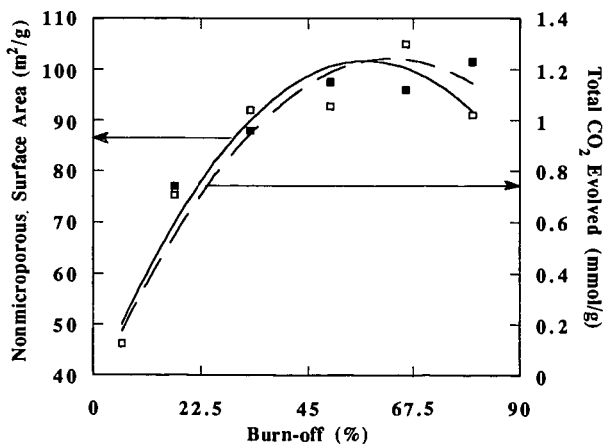

Figure 4. Comparison of total CO_2 evolved with nonmicroporous surface area as a function of burn-off (0.1MPa, 420°C).
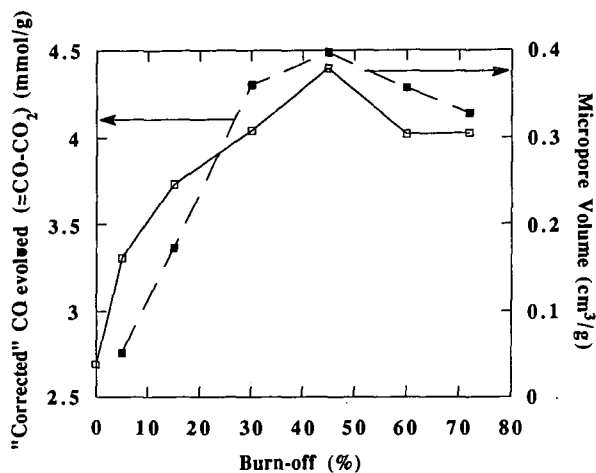
Figure 5. Comparison of total "corrected" CO evolved with micropore volume for resin char as a function of burn-off (0.1MPa, 470°C).
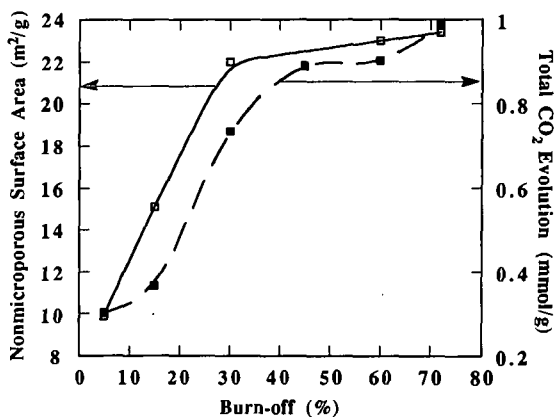

Figure 6. Comparison of total CO_2 evolved with nonmicroporous surface area for resin char as a function of burn-off (0.1 MPa, 470°C).
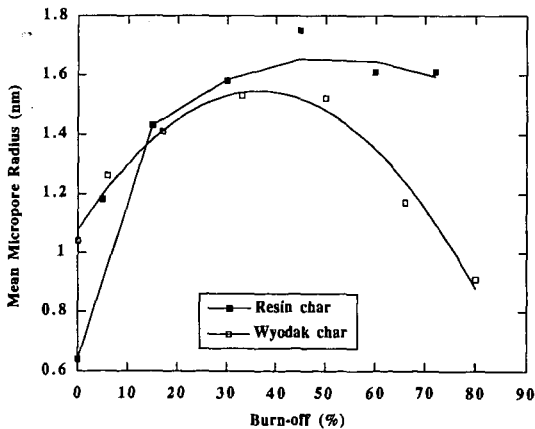

Figure 7. Mean pore radius as a function of burn-off for resin and Wyodak coal char, as determined from the "extended" random pore model.

ANALYSIS OF CARBON-OXYGEN REACTION BY USE OF A SQUARE-INPUT RESPONSE TECHNIQUE AND ^{18}O ISOTOPE

Kouichi Miura and Hiroyuki Nakagawa
Department of Chemical Engineering, Kyoto University
Kyoto 606, Japan

INTRODUCTION

Carbon gasification reaction has been investigated for decades including the pioneering works of Walker and his co-workers[1], but its mechanism has not been completely elucidated. The concept of the active surface area (ASA) was proposed by them, and its importance has been recognized. However, since ASA was measured by O_2 chemisorption at below 300 °C where carbon loss through gasification is negligible, it does not reflect the actual gasification situation. To overcome this weak point, measurements of ASA in a batch reactor[2-4] and the so-called transient kinetic (TK) method were proposed[5,6]. Ahmed and Back[4] successfully measured the chemisorbed oxygen during the gasification using a batch reactor, and proposed a new mechanistic sequence for carbon-oxygen reaction which stresses the importance of the reaction between the gaseous oxygen and the chemisorbed oxygen. Radovic et al.[7,8] proposed the concept of the reactive surface area (RSA), and reported excellent proportionality between the CO_2 gasification rate and the RSA estimated by the TK and the TPD methods. Kapteijn et al.[9,10] showed that the TK method with labeled molecules is more powerful to examine the mechanism. They found the presence of two types of surface oxygen complexes which desorb at different rates.

Although the TK method is powerful, the method can trace only the desorption phenomena after a step change from an oxidizing gas stream to an inert gas stream. On the other hand, the step response technique changing an isotope stream to another isotope stream step-wisely enables us to observe *in situ* transient behavior without disturbing the reaction system if we can trace the change in all isotope species. This technique has been recently applied to carbon-oxygen reaction by Kyotani et al.[11]

The authors have recently proposed a Square-Input Response (SIR) method as a modification of the step response technique[12]. When we apply the SIR technique to carbon-oxygen reaction, we change the reactant stream containing $^{16}O_2$ step-wisely to the $^{18}O_2$ containing stream at a certain instant, and after a predetermined time interval we change the $^{18}O_2$ stream backwardly to the $^{16}O_2$ stream. This method enables us to observe transient changes on two step changes, to minimize the usage of expensive isotopes, and to facilitate the establishment of the balance of the isotope supplied as the square-input. We have successfully applied this technique to the analysis of a coal char gasification and to the analysis of the stabilization reaction of carbon fiber[13].

In this work the SRI technique was applied to the analysis of carbon-oxygen reaction to examine the reaction mechanism presented by the authors[14], and to determine the rate constants of elementary reactions.

EXPERIMENTAL

A mineral-free carbon black (CB) was used in this study. It was provided by Mitsubishi Chemicals and had the designation CB-30. The ultimate analysis of CB is C: 99.1%, H: 0.8%, and O: 0.1% on weight basis .

Figure 1 shows the apparatus used for the gasification experiments. About 3 to 12 mg of CB were embedded in a reactor made of quartz tube (4mm in ID and 30 cm in length). They were heated to 900 °C in a helium stream and held at this temperature for 10 minutes. Then they were cooled to a constant temperatures of 550, 570, or 600°C. To start the gasification, the helium stream was changed to the $^{16}O_2$ stream diluted by helium (22% conc.), whose flow rate was regulated by a mass flow controller at 50 ml/min. A part of the product gas was introduced to a pressure regulated section *via* a valve (V-2). The pressure of this section was kept at a few mmHg by regulating the opening of the valve V-2. Only a small amount of gas was introduced from this section to a mass spectrometer (MS; Nichiden Anerva, AGS211R), where signals for mass numbers of 28, 30, 32, 36, 44, 46, and 48 were continuously detected. To minimize the delay of the gas analysis from the gas formation, a small tubing (1/16 inch OD) was used and the gas flow in the pressure regulated section was designed as shown in the bottom of Fig. 1. The main flow exiting the reactor was led to a gaschromatograph (GC), where it was analyzed in every 10 minutes to determine precisely the concentrations of CO, O_2, and CO_2. By referring to these concentrations the signals of the MS were calibrated in every 10 minutes. Then the concentration of CO, O_2, and CO_2 in the product gas could be measured continuously and precisely.

The pure ^{18}O isotope (ISOTEC Inc.) containing 99.2 mol % ^{18}O was used for the SIR experiment. The isotope diluted by helium (22% $^{18}O_2$ conc.) was stored in a sample loop of about 50 ml as shown in Figure 1. When the conversion of CB reached 10 %, the 6-way

valve (V-1) was switched. Then the helium stream containing $^{16}O_2$ pushed out the $^{18}O_2$ containing gas in the sample loop to the reactor. The $^{18}O_2$ containing stream was supplied for about 1 min, and then the stream returned again to the stream containing only $^{16}O_2$. After the elapse of 20 min the temperature was raised to 900°C to combust the sample, and the ^{18}O retained in the sample was detected as $C^{18}O$, $C^{18}OO$, and $C^{18}O_2$. Using this technique, the exact ^{18}O balance could be established after changing the $^{18}O_2$ containing stream to the stream containing only $^{16}O_2$. The experiments using 1:1 mixture of $^{16}O_2$ and $^{18}O_2$ as the square-input were also performed to examine probable isotope exchange reactions. The experiments using pure He as the square-input were also performed. The experiments are performed to compare our results with those obtained by the so called TK experiments.
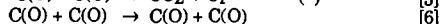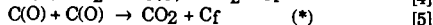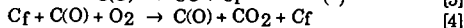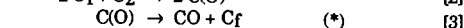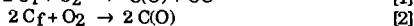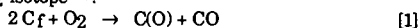
RESULTS AND DISCUSSION

Figures 2a and 2b show typical SIR results, where the formation rates of CO(28), CO(30), $CO_2(44)$, $CO_2(46)$, and $CO_2(48)$ and the flow rate of $O_2(36)$ are shown against the reaction time. Hereinafter, the isotopes are represented by the molecular weights in the brackets following the molecular formula. Figures 2c and 3, respectively, show the results obtained using the square-inputs of the 1:1 mixture of $^{16}O_2$ and $^{18}O_2$ and the pure He under the same experimental conditions as those in Fig. 2b.

First, we consider CO formation in Figs. 2a and 2b. On the step change from the $^{16}O_2$ stream to the $^{18}O_2$ (abbreviated to the $^{16}O_2/^{18}O_2$-step) the CO(28) formation rate decreased rapidly to a half or so, and then decreased gradually. The CO(30) formation rate responded almost instantaneously to the step change to increase a certain level, and increased gradually. On the step change from the $^{18}O_2$ stream to the $^{16}O_2$ (the $^{18}O_2/^{16}O_2$-step) almost reverse responses were observed. The CO(28) formation rate increased rapidly at first, then increased gradually. The CO(30) formation rate decreased instantaneously on the step change to a small value, then decreased gradually. These results clearly show that CO is formed at least two reactions. The gradual formation of CO(28) and CO(30) without the corresponding oxygen isotopes in the gas phase indicates that these are produced from the chemisorbed oxygen. The rapid changes of the formation rates of both CO(28) and CO(30) on the step changes are associated with the reaction between the gas phase oxygen and the active site.

The CO_2 formation rates are considered next. On the $^{16}O_2/^{18}O_2$-step the $CO_2(44)$ formation rate responded almost similarly as the CO(28) formation rate. The $CO_2(46)$ formation rate increased rapidly on the step change, but started to decrease gradually after reaching a maximum. The $CO_2(48)$ formation rate responded slowly to the step change, but it increased monotonously. On the $^{18}O_2/^{16}O_2$-step the $CO_2(44)$ formation rate again responded almost similarly as the CO(28) formation rate. The $CO_2(46)$ formation rate decreased rapidly first, and then decreased gradually. The $CO_2(48)$ formation rate decreased rapidly to a very small value, then decreased gradually. These results indicate that CO_2 is formed by several reaction paths: both the reaction between gaseous oxygen and chemisorbed oxygen and the reaction between chemisorbed oxygens are judged to be significant.

Both the total CO formation rate (the sum of the formation rates of CO(28) and CO(30)) and the total CO_2 formation rate (the sum of the formation rates of $CO_2(44)$, $CO_2(46)$, and $CO_2(48)$)change little during the SRI experiments as shown in Figs. 2a to 2c. This indicates that the SIR experiment using ^{18}O is powerful to examine the reaction mechanism without disturbing the steady state of reaction as expected. This conclusion is further substantiated when comparing Figs. 2b and 3. The response behavior of CO(28) and $CO_2(44)$ in Fig. 3, which is the TK experiment, is significantly different from that in Fig. 2b. The gradual formations of both CO(28) and $CO_2(44)$ observed in Fig.2b were not observed in Fig. 3. This means that the rate parameters determined by the TK method is different from those under the gasification of steady state for at least this reaction system.

We presented the following gasification mechanism for carbon oxidation based on the pulse experiments using $^{18}O_2$ isotope[14].

$$2\,C_f + O_2 \;\rightarrow\; C(O) + CO \qquad\qquad [1]$$
$$2\,C_f + O_2 \;\rightarrow\; 2\,C(O) \qquad\qquad [2]$$
$$C(O) \;\rightarrow\; CO + C_f \qquad (*) \qquad [3]$$
$$C_f + C(O) + O_2 \;\rightarrow\; C(O) + CO_2 + C_f \qquad [4]$$
$$C(O) + C(O) \;\rightarrow\; CO_2 + C_f \qquad (*) \qquad [5]$$
$$C(O) + C(O) \;\rightarrow\; C(O) + C(O) \qquad [6]$$

where C_f and C(O) represent the free active site and the chemisorbed oxygen, respectively. We assumed that these reactions proceed only when gaseous oxygen is present. The mechanism is close to that proposed by Ahmed et al.[4] One of the great differences is that we assume the amount of the short-lived oxygen is immeasurably small as Walker et al. assumed in the earlier paper[3]. In other words, we assumed that the short-lived oxygen is formed through Eqs. 1, 2, 4 and 6 only when gaseous oxygen interacted with carbon surface and the oxygen complex. The reactions in which only the short-lived oxygen surface intermediate participates are marked by an asterisk (*).

The validity of the proposed mechanism can be examined in more detail using the results

129

obtained in this work. The balance of the ^{18}O after the $^{18}O_2/^{16}O_2$-step is easily established as stated above, because we analyzed all the ^{18}O containing species including the amount of ^{18}O retained in the sample. Then the amount of chemisorbed oxygen, $n_O(18)$, at a certain time is estimated by summing up the ^{18}O evolved as CO(30), $CO_2(46)$, 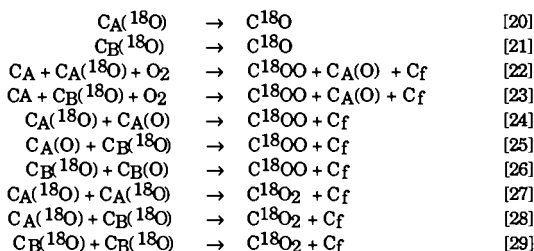and $CO_2(48)$ from the end of the reaction. Utilizing the $n_O(18)$ values estimated, the formation rates of CO(30) and $CO_2(46)$were plotted against $n_O(18)$ in Figures 4a and 4b at three reaction temperatures. Both rates increased with the increase of $n_O(18)$ as expected, but linear relationships did not hold. Since CO(30) is produced *via* Eq. 3, the CO(30) formation rate should be directly proportional to $n_O(18)$ if CO(30) was produced from only the stable oxygen complex. However, this was not the case, indicating that the contribution of the short-lived oxygen must be taken into account to explain the CO(30) formation. The relationship between the $CO_2(46)$ formation rate and $n_O(18)$ in Fig. 4b cannot be explained by only Eqs. 4 and 5 as far as we assume only single oxygen complex.

Then the mechanism was rewritten assuming two active sites, C_A and C_B, and in consequence two oxygen complexes, $C_A(O)$ and $C_B(O)$, as follows:

$$C_A + O_2 \rightarrow C_A(O) + CO \qquad ; r_{1A} \qquad [7]$$
$$C_B + O_2 \rightarrow C_B(O) + CO \qquad ; r_{1B} \qquad [8]$$
$$2C_A + O_2 \rightarrow 2\,C_A(O) \qquad ; r_{2A} \qquad [9]$$
$$2C_B + O_2 \rightarrow 2\,C_B(O) \qquad ; r_{2B} \qquad [10]$$
$$C_A(O) \rightarrow CO + C_f \qquad ; r_{3A} \qquad [11]$$
$$C_B(O) \rightarrow CO + C_f \qquad ; r_{3B} \qquad [12]$$
$$C_A + C_A(O) + O_2 \rightarrow CO_2 + C_A(O) \qquad ; r_{4A} \qquad [13]$$
$$C_A + C_B(O) + O_2 \rightarrow CO_2 + C_A(O) \qquad ; r_{4B} \qquad [14]$$
$$C_B + C_A(O) + O_2 \rightarrow CO_2 + C_B(O) \qquad ; r_{4C} \qquad [15]$$
$$C_B + C_B(O) + O_2 \rightarrow CO_2 + C_B(O) \qquad ; r_{4D} \qquad [16]$$
$$C_A(O) + C_A(O) \rightarrow CO_2 \qquad ; r_{5A} \qquad [17]$$
$$C_A(O) + C_B(O) \rightarrow CO_2 \qquad ; r_{5B} \qquad [18]$$
$$C_B(O) + C_B(O) \rightarrow CO_2 \qquad ; r_{5C} \qquad [19]$$
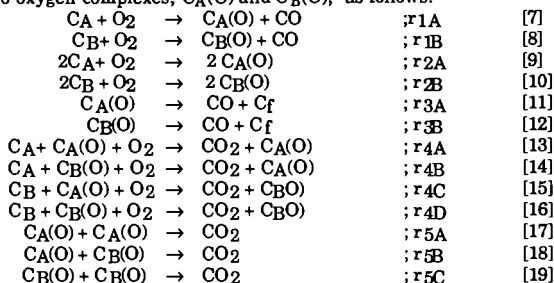
where $C_A(O)$ and $C_B(O)$ represent the short-lived oxygen complex and the stable oxygen complex, respectively. The contribution of Eq. 6 was neglected, because the amounts of $C_A(O)$ and $C_B(O)$ do not change through the reaction. r_{1A} to r_{5C} represent the reaction rates.

The validity of the reaction mechanism was tested using the change in the ^{18}O containing species after the $^{18}O_2/^{16}O_2$-step. The mechanistic sequence for this case is simplified as follows:

$$C_A(^{18}O) \rightarrow C^{18}O \qquad [20]$$
$$C_B(^{18}O) \rightarrow C^{18}O \qquad [21]$$
$$C_A + C_A(^{18}O) + O_2 \rightarrow C^{18}OO + C_A(O) + C_f \qquad [22]$$
$$C_A + C_B(^{18}O) + O_2 \rightarrow C^{18}OO + C_A(O) + C_f \qquad [23]$$
$$C_A(^{18}O) + C_A(O) \rightarrow C^{18}OO + C_f \qquad [24]$$
$$C_A(O) + C_B(^{18}O) \rightarrow C^{18}OO + C_f \qquad [25]$$
$$C_B(^{18}O) + C_B(O) \rightarrow C^{18}OO + C_f \qquad [26]$$
$$C_A(^{18}O) + C_A(^{18}O) \rightarrow C^{18}O_2 + C_f \qquad [27]$$
$$C_A(^{18}O) + C_B(^{18}O) \rightarrow C^{18}O_2 + C_f \qquad [28]$$
$$C_B(^{18}O) + C_B(^{18}O) \rightarrow C^{18}O_2 + C_f \qquad [29]$$

Under the steady state gasification the total amount of chemisorbed oxygen, n_O, is kept constant, and both n_{OA} and n_{OB} would be kept constant. Then the following relationships would hold:

$$n_{OA} + n_{OB} = n_O \quad \text{(constant)} \qquad [30]$$
$$n_{OA}(16) + n_{OA}(18) = n_{OA} \quad \text{(constant)} \qquad [31]$$
$$n_{OB}(16) + n_{OB}(18) = n_{OB} \quad \text{(constant)} \qquad [32]$$

Using the data for the changes in the ^{18}O species after the $^{18}O_2/^{16}O_2$-step and the relationships of Eqs. 30 to 32, we could determine the reaction rate constants, k_{3A}, k_{3B}, $k_{4A}[C_A]+k_{4B}[C_A]$, $k_{4C}[C_B]+k_{4D}[C_B]$, k_{5A}, k_{5B}, and k_{5C}, and the values of n_{OA}, n_{OB}, and n_O which appear in r_{3A}, r_{3B}, r_{4A}, r_{4B}, r_{4C}, r_{4D}, r_{5A}, r_{5B}, and r_{5C}. Then the rate constants, $k_{1A}+k_{1B}$, and $k_{2A}[C_A]+k_{2B}[C_B]$ could be estimated using the change in the formation rate of CO(28), the relationship of Eq. 30 and the parameters determined above. Thus all the rate constants were estimated, although some can not be determined independently. The rate constants at 570°C are shown in Table 2, and the calculated curves using these parameters are compared with the experimental data in Figure 5. Fairly good agreements were obtained between the calculated curves and the experimental data over the whole course of gasification, although most of the parameters were estimated using the changes in the ^{18}O species after the $^{18}O_2/^{16}O_2$-step. We could estimate the amounts of both n_{OA} and n_{OB}, and could clarify that n_{OA} is much smaller than n_{OB}. These results seem to support the validity of the mechanistic sequence given in Eqs. 7 to 19.

At 570°C the ratio of $r_{1A}+r_{1B} : r_{3A} : r_{3B}$ for the CO formation was 4 : 3 : 3, and the ratio of $r_{4A}+r_{4B} : r_{4C}+r_{4D} : r_{5A} : r_{5B} : r_{5C}$ for the CO_2 formation was 4 : 4 : 1 : 2 : 2. These values clearly indicate the importance of the direct reactions between the active site and the gaseous oxygen as well as the desorption and/or reaction of chemisorbed oxygen(s),

supporting the observations given in Figs. 2a to 2c.

CONCLUSION

A square-input response (SIR) technique was applied to analyze the carbon-oxygen reaction. Actual *in situ* transient behaviors of isotopes were successfully traced. Most significant findings are as follows: Existence of two oxygen complexes, one is short-lived and the other is rather stable, was clarified, and their amounts were estimated. The importance of the direct attack of the gaseous oxygen to the active site and/or the chemisorbed oxygen was clarified. In addition, the significant contributions of the desorption of the oxygen complex and the reaction between the complexes to the gasification reaction were notified. The TK method was found not to reflect *in situ* desorption behavior of the oxygen complex at least for the reaction system studied here. Relative importance of elementary reactions was clarified. Further investigation is under way to examine the soundness of the proposed reaction mechanism and the determined rate parameters.

Literatures Cited

1. Laine, N.R.; Vastola, F.J.; Walker, P.L., Jr. J.Phys.Chem. **1963**, 67, 2030- 2034.
2. Tucker, B.G.; Mulcahy, F.R. Trans. Faraday Soc. **1959**, 65, 274-286.
3. Vastola, F.J.; Hart, P.J.; Walker, P.L., Jr. Carbon **1965**, 2, 65-71.
4. Ahmed, S.; Back, M.H.; Roscoe, J.M. ACS Division Fuel Chemistry, **1989**, 34, No.1, 63-70.
5. Freund, H.; Fuel, 1986, 65, 63-66.
6. Nozaki, T.; Adschiri, T.; Furusawa, T. Fuel Process. Techn. **1990**, 24, 277-283.
7. Jiang, H.; Radovic, L.R. ACS Division Fuel Chemistry, **1989**, 34, No.1, 79-86.
8. Lizzo, A.A.; Jiang, H.; Radovic, L.R. Carbon **1990**, 28, 7-19.
9. Kapteijn, F,; Meijer, R.; Moulijn, J.A. Energy & Fuels **1992**, 6, 494-497.
10. Kapteijn, F,; Meijer, R.; Moulijn, J.A.; Cazorla-Amoros, D. Carbon, 1994, 32, 1223-1231.
11. Zhuang, Q.; Kyotanim T.; Tomita, A. Energy & Fuels **1995**, 9, 630-634.
12. Miura, K.; Zha, H.; Hashimoto, K. *Proc. 30th Conf. Coal Sci., Tokyo, Jpan, Oct. 25-26*, **1993**, 63-66.
13. Miura, K.; Nakagawa, H,; Carbon Hashimoto, K. Carbon **1995**, 33, 275-282.
14. Crick, T.M.; Silveston, P.L.; Miura, K.; Hashimoto, K.; Energy & Fuels **1993**, 7, 1054-1061.

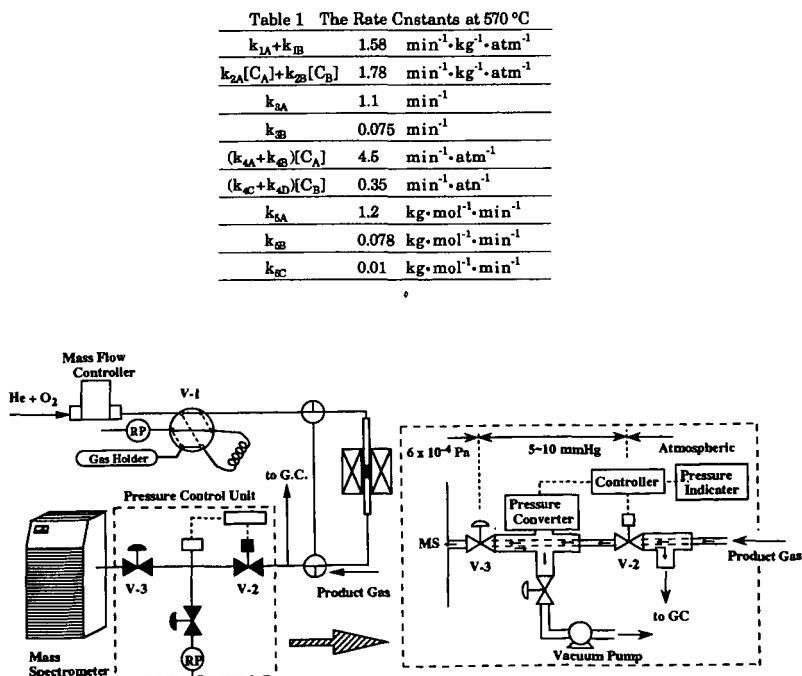### Table 1   The Rate Cnstants at 570 °C

$k_{1A}+k_{1B}$	1.58	$min^{-1} \cdot kg^{-1} \cdot atm^{-1}$
$k_{2A}[C_A]+k_{2B}[C_B]$	1.78	$min^{-1} \cdot kg^{-1} \cdot atm^{-1}$
k_{3A}	1.1	min^{-1}
k_{3B}	0.075	min^{-1}
$(k_{4A}+k_{4B})[C_A]$	4.5	$min^{-1} \cdot atm^{-1}$
$(k_{4C}+k_{4D})[C_B]$	0.35	$min^{-1} \cdot atn^{-1}$
k_{5A}	1.2	$kg \cdot mol^{-1} \cdot min^{-1}$
k_{5B}	0.078	$kg \cdot mol^{-1} \cdot min^{-1}$
k_{5C}	0.01	$kg \cdot mol^{-1} \cdot min^{-1}$

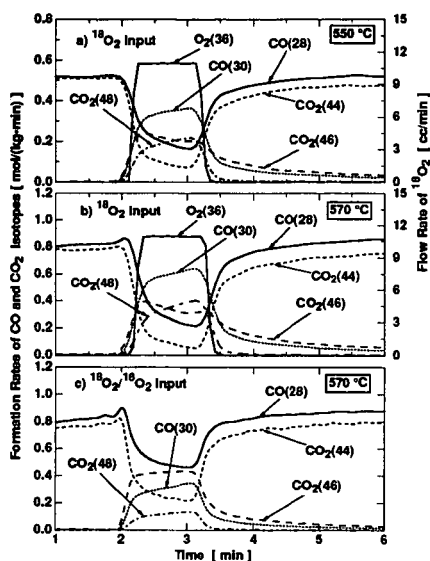**Figure 1 Experimental Apparatus**

Figure 2 Changes in the formation rates of CO and CO_2 isotopes of the SIR experiment
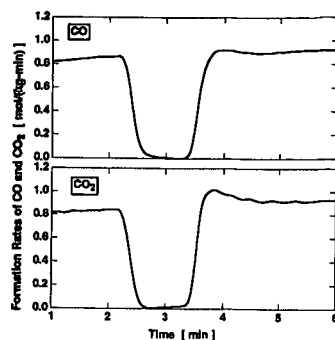

Figure 3 Changes in the formation rates of CO and CO_2 SIR experiment using square-input of the He (Equivalent to the TK technique)
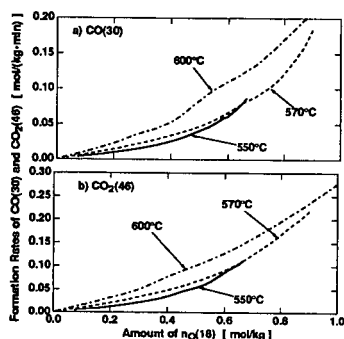

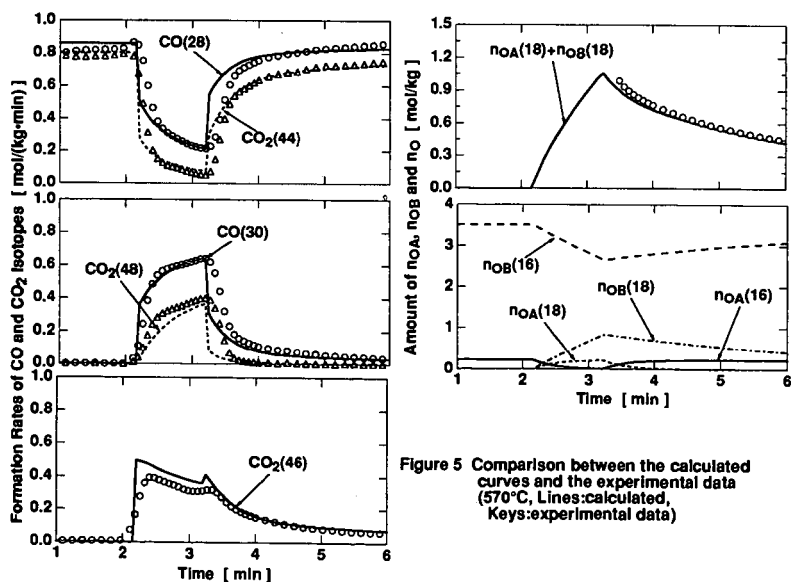Figure 4 Relationships between formation rates of CO(30), CO_2(46) and n_O(18)

Figure 5 Comparison between the calculated curves and the experimental data (570°C, Lines:calculated, Keys:experimental data)

132

ADSORBED MOLECULAR OXYGEN AND THE SURFACE BEHAVIOR OF SOOT

D. M. Smith, M. M. O. Atteya, B. K. Konowalchuk,
M. L. Rosenberger, and A. R. Chughtai
Department of Chemistry, University of Denver
Denver, CO 8020B

INTRODUCTION
A role of adsorbed molecular oxygen in surface reactions of black carbon (in the form of n-hexane soot) has been observed. Countless articles on the surface structure and reactivity of solid carbon, including several from this group (1-5), have identified carbon-oxygen surface functionalities as underlying adsorption or reactivity characteristics of specific materials. This paper describes, rather, several cases in which reversibly adsorbed molecular oxygen directly participates in phenomena occurring at the carbon surface.

RESULTS AND DISCUSSION
Hydration
A dependence of the extent of its surface hydration on soot aging was first observed in microgravimetric studies of water adsorption as a function of relative vapor pressure (6). Separate experiments in which freshly-prepared soot samples were exposed to pure O_2 prior to hydration with others evacuated prior to hydration, revealed significantly more and less water adsorption, respectively, compared with the fresh soot itself. Application of a modified Dubinin-Radushkevich (DR) equation (7) to the data enabled the determination of surface coverage and mass adsorbed per gram at limiting adsorption, and also at the point at which activated adsorption is essentially complete (the chemisorption limit).

The adsorption data (mass increase and the relative water pressure, P/P_0) from these measurements were treated with the DR equation to yield the results summarized in Table I.

Table I. Effect of Oxygen Adsorption on Soot Hydration

Soot	Limiting Adsorption $gx10^2/gs$	$\Theta_o{}^*$	Limiting Chemi-sorption $gx10^2/gs$	$\Theta_c{}^*$
24-hours O_2- contacted	1.76 ± 0.01	0.80 ± 0.02	0.507 ± 0.004	0.223 ± 0.004
Fresh	1.26 ± 0.01	0.58 ± 0.01	0.473 ± 0.005	0.217 ± 0.005
Evacuated	0.966 ± 0.006	0.44 ± 0.01	0.440 ± 0.003	0.202 ± 0.005

* Surface coverage using H_2O molecular area as $12.2\mathring{A}^2$ (8), where Θ_o is at limiting adsorption and Θ_c at the chemisorption limit.

As is evident from these data, adsorption of water by the soot increases with O_2 coverage of the soot surface. For example, the limiting surface coverage (Θ_o) increases from 44% for evacuated fresh soot to 80% for the same material whose surface is saturated with O_2 at ambient temperature. Similarly, by comparing the adsorption of water at the chemisorption limit and at limiting adsorption, it is seen that the fraction of adsorbed water involving chemisorption decreases from about 46% to 29% as the surface O_2 increases. Since a smaller fraction of the (greater) adsorbate is involved in chemisorption on an O_2-saturated surface, a process involving the hydrolysis of

carboxylic functionalities, the adsorbed oxygen appears to be providing adsorption sites for water. A regular decrease in adsorbate affinity coefficient for water (6) with increased O_2 coverage, determined from the DR equation plot, further supports relatively more (weaker) H_2O-O_2 surface interactions.

Although the mechanism by which surface O_2 facilitates increased water adsorption is not yet clear, earlier experiments showed that it is properly described as physisorption (as opposed to activated adsorption). Figure 1 illustrates the effect of the sequential treatment of soot with flowing dry nitrogen, water
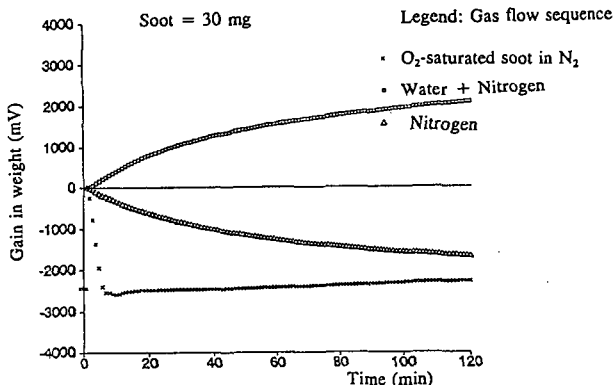

Figure 1. Study of desorption and adsorption of O_2 and H_2O on soot (6).

vapor plus nitrogen and then nitrogen again. Microgravimetric measurement of mass change reveals a rapid substantial loss when an O_2-saturated sample is subjected to flowing nitrogen, apparently most of it the loss of physisorbed O_2. Subsequent to resetting the microbalance, treatment with water vapor plus nitrogen, and then flowing nitrogen again shows the usual hydration pattern and removal of water adsorbate, respectively. Considerable quantities of molecular oxygen may be adsorbed on freshly-prepared n-hexane soot and are involved in the water adsorption by, and hydration of, the soot surface.

EPR Studies
The observation by EPR of significant concentrations of unpaired electrons in n-hexane soot(1), consistent with their existence in coals and other graphitic carbonaceous materials, suggested the use of spin density as a probe of the behavior of adsorbed molecular oxygen which is paramagnetic. The effect of adsorbed O_2 is to increase the width and to decrease the intensity of the EPR spectrum of soot, changes reflected in an increased peak-to-peak line width, decreased peak height, and decreased normalized integral of the single absorption having a g value of 2.0046. Accordingly, series of replicate measurements using X-band CW EPR on freshly prepared soot samples were carried out. These samples, attached to the vacuum line through a special manifold within a heating mantle, were evacuated at 100°C in the 10^{-6} torr range overnight before exposure to accurately measured pressures of pure O_2. Figure 2A is a plot of the corrected normalized integral (CNI) versus P_{O_2}, where the error bars represent the standard deviation of individual measurements. The CNI for soot evacuated in this manner, before addition of O_2, is (1.62 ± 0.07) x 10^7. The linear relationship between spin density and physisorbed O_2 (assumed proportional to gas phase pressure) over the pressure range from 0 to 35 torr demonstrates not only the interaction between the unpaired electron spins of molecular

oxygen and soot, but also provides a means of monitoring the surface behavior of O_2 during adsorption or reaction.
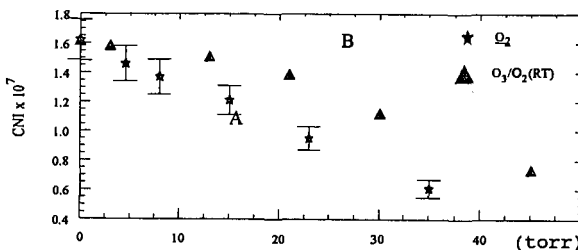

Figure 2. Effect of O_2 on the EPR signal of soot.

The Ozone-Soot Reaction
A detailed study (9) of the reaction between n-hexane soot and ozone at low concentrations has revealed a role of adsorbed molecular oxygen. This complex reaction involves essentially three stages. Following a fast initial catalytic decomposition of O_3, a rapid soot mass increase accompanied by CO_2 and H_2O formation is itself followed by a long period of soot oxidation in which the rate of O_3 loss is second order in O_3 (9). It is during the second stage of this reaction that material balance calculations, based upon careful analysis of products and reactants, reveal an involvement of O_2 in that stage. Expressing the oxygen atom content of reactants and products in micromoles, the overall reaction results in a net loss of O_3 oxygen (as O_2 from catalytic decomposition) in the amount of about 20% which does not yield measurable O-containing product. During this second stage of the reaction, from 2.5 to 30% of reaction, however, the O atom gain in products averages 70%, a gain which is not from O_3 oxygen.

A plot of CNI of the soot EPR spectrum versus gas pressure (1.5% O_3 in O_2) is Figure 2B, to be compared with the same plot for O_2 alone (Figure 2A). At lower pressures, the rate of spin density decrease with increased O_3/O_2 is much less than with O_2 alone, while beyond 20 torr the slopes of the two plots are essentially the same. These data appear to confirm the consumption of a fraction of the O_2 in a reaction which does not leave it for physisorption. A plausible interpretation is that the rapid reaction with O_3, actually probably O atom from its dissociation, yields fragments on the carbon surface which are reactive with O_2. The soot is not similarly reactive with O_2 alone under ambient conditions. We are not aware of other such examples of physisorbed O_2 involvement in surface reactions of black carbon. To the extent that soot " aging" is an annealing of the surface by physisorbed O_2, this effect also must underlie the difference in rate laws for the O_3-soot reaction (9) between freshly prepared and aged soot; for example,

Initial rate = $k[O_3](soot)^{1/2}$ (1)
versus
Initial rate = $k'[O_3] + k''(soot)$ (2)

respectively.

Other Adsorptions
SO_2
Because of the likelihood that adsorbed molecular O_2 plays a role in other soot surface reactions, in the manner discovered for the O_3 reaction, our studies of adsorption on soot also have included O_2 as adsorbate. The rapid oxidation of SO_2 at the soot surface which requires the presence of O_2 and H_2O, for example,

is one important case. The coadsorption of O_2 and SO_2 on n-hexane soot has been examined in detail.

Figure 3 shows the gain in mass of 10 mg soot as a function of
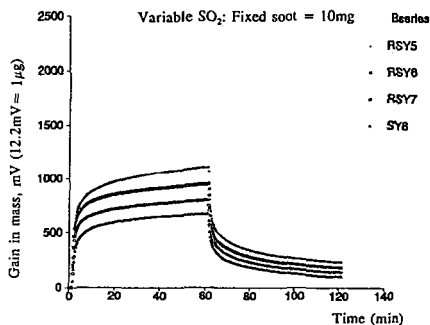

Figure 3. Adsorption of SO_2 on soot.

time in the presence of 606, 1010, 1515, and 2020 ppm SO_2. These were flow experiments in which the medium was zero air. At 60 minutes, the SO_2 flow was stopped and the microgravimetric cell (6) continued to purge with the zero air alone. The rapid loss of SO_2 from the surface follows a pattern which is the inverse of the adsorption, indicating physisorption of SO_2 according to

$$SO_{2\,(g)} + SS \underset{k_{-1}}{\overset{k_1}{\rightleftharpoons}} SS.SO_2(ads) \qquad (3)$$
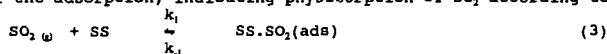
$$K = k_1/k_{-1} = [SS.SO_2(ads)]/[SO_2(g)][SS] \qquad (4)$$

where SS = surface site for SO_2.

From 85 to 79 percent of the SO_2 behaves in this manner, respectively, as indicated by the asymptotic approach of the microgravimetric curve to a limiting mass value greater than the initial. Another pathway, probably surface hydration and possibly oxidation, apparently exists for SO_2 as well; water molecules cannot be rigorously excluded from the surface under these conditions.

The coadsorption of SO_2 and O_2 were studied by EPR, and the results are summarized in Figure 4. No effect of SO_2 on the
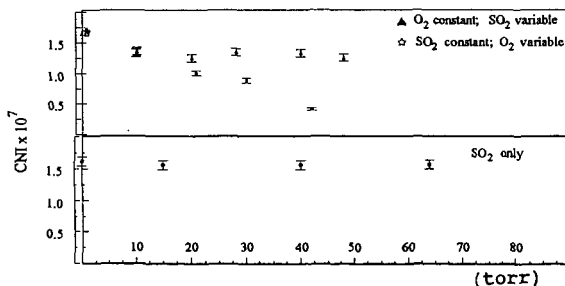

Figure 4. Effect of SO_2 on soot.

normalized integral of soot's EPR signal is observed, this lack of effect extending to 10^5 ppm. (The small decline from the 1.62

136

is due to a trace of O_2 in the SO_2 sample). The significance of this study is to be found in the fact that 1) O_2 has the same effect on the spin density of soot on which SO_2 is physisorbed as it does on pure soot, and 2) at a constant O_2 coverage, SO_2 has no effect; no O_2 is displaced by SO_2. This suggests that surface oxidation of SO_2 by O_2 does not occur measurably at these surface coverages. Either O_2 and SO_2 do not compete for the same sites or the soot surface-O_2 interaction is stronger than that between soot and SO_2. Calculations based on the specific surface of n-hexane soot ($89m^2/g$), masses of O_2 and SO_2 adsorbed per gram of soot under the experimental conditions, and established surface areas for the adsorbed molecules (19.2 Å^2 for SO_2 (10), 14.1 Å^2 for O_2 (11), indicate that SO_2 occupies nearly the same fraction of the surface ($\sim18\%$) that O_2 ($\sim20\%$) does, which means that about 1/3 less SO_2 molecules than O_2 are adsorbed per unit mass of soot under the conditions of zero air (125 torr O_2) and 2000 ppm SO_2. In the case of paramagnetic O_2, the surface coverage is no doubt governed by the surface density of soot's unpaired electrons, where the SO_2 is not influenced by that factor.

NO and NH$_3$

Evidence of the effect of adsorbed molecular O_2 on the adsorption of both NH_3 and NO has been found as well. These molecules, unlike the reversibly adsorbed SO_2 species, compete with O_2 for surface sites. Microgravimetric studies of NH_3 adsorption at higher concentrations, carried out in a variety of gas phase environments, reveal this competition which probably has its origin in the hydrogen bonding capacity of NH_3. EPR studies of the competition of NO and O_2 for unpaired electron sites on soot clearly show a surface interaction between NO and O_2 as well. Experiments on both of these systems continue.

REFERENCES
1. Akhter, M. S.; Chughtai, A. R. ; Smith, D. M., Appl. Spectrosc. 1985, 39, 143.
2. Akhter, M. S.; Chughtai, A. R. ; Smith, D. M., Appl. Spectrosc. 1985, 39, 154.
3. Chughtai, A. R. ; Jassim, J. A.; Peterson, J. A.; Stedman, D.H.; Smith, D. M., Aerosol. Sci. Technol. 1991, 15, 112.
4. Akhter, M. S.; Chughtai, A. R. ; Smith, D. M., Appl. Spectrosc. 1991, 45, 653.
5. Smith, D. M.; Chughtai, A. R., Trends. Appl. Spectrosc. 1993,1, 325.
6. Chughtai, A. R.; Brooks, M. E.; Smith, D. M., J. Geophys. Res., 1995, in press.
7. Kobayashi, M.; Ishikawa, E.; Toda, Y., Carbon 1993,31,990.
8. Harkins, W. D. ; Jura, G. J., J. Am. Chem. Soc. 1944, 66, 1366.
9. Smith, D. M.; Chughtai, A. R., J. Geophys. Res., 1995, in press.
10. Billinge, B. H. M., in Second Conference on Industrial Carbon and Graphite, Society of Chemical Industry, London, 1966; p. 399.
11. Adamson A. W., Physical Chemistry of Surfaces; 5 ed., Wiley, N.Y., 1990; p. 612.

THE EFFECT OF CO_2 PARTIAL PRESSURE ON GASIFICATION REACTIVITY

L. Zhang and J.M. Calo
Chemical Engineering Program
Division of Engineering
Brown University
Providence, Rhode Island 02912, U.S.A.

INTRODUCTION

The mechanisms by which varying partial pressures of oxidant gases affect char reactivity remains a matter of controversy. In the current communication we explore the effect of CO_2 partial pressure on the resultant populations of intermediate oxygen complexes on char surfaces and their relationship to reactivity.

EXPERIMENTAL

The samples used in the experiments were Wyodak subbituminous coal char samples produced from coal obtained from the Argonne Premium Coal Sample Bank [1], and a resin char produced from phenol-formaldehyde resin synthesized in our laboratory. The latter was used as a prototype of a non-mineral matter-containing char. Char samples were produced in a tube furnace in flowing ultrahigh purity helium at 1000°C for two hours.

Partial pressure variation was achieved using CO_2/helium mixtures. All the oxidation and thermal desorption experiments were carried out in the TPD-MS/TGA apparatus. For gasification, the samples were exposed to the CO_2/helium gas mixtures at one atmosphere at a selected temperature to a certain degree of burn-off. The gasification conditions selected for the current work were 825°C, 20% burn-off for Wyodak coal char, and 900°C, 5% burn-off for resin char. The thermal desorptions were all carried out at a heating rate of 50K/min to 1200°C in flowing ultrahigh purity helium carrier gas.

RESULTS AND DISCUSSION

The overall or global reaction order for the char-CO_2 reaction remains a matter of controversy. The typical Langmuir-Hinshelwood-type steady-state rate expressions, as obtained for the Mentser and Ergun [2] oxygen exchange mechanism for example, suggest that the reaction should be first order at low pressures, changing gradually to zeroth order behavior at higher pressures. Turkdogan and Vinters [3] reported half-order dependence at pressures less than 10 atm, and zeroth order behavior at pressures of 10-20 atm. Koenig *et al.* [4] also reported half-order behavior. Blackwood and Ingeme [5] reported that at high pressure, the gasification rate remains dependent on CO_2 partial pressure to a positive order. On the other hand, the gasification data of Johnson [6] for a bituminous coal char in CO/CO_2 mixtures over the range 2-35 atm, showed a decreasing effect of CO_2 pressure on the gasification rate at high pressures. A similar trend was reported by Golovina [7], who reported first order behavior at near-atmospheric pressure, tending to zeroth order over the 3-10 atm range, followed by decreasing gasification rate with CO_2 partial pressure in the 20-40 atm range. In the current work, the apparent reaction orders observed for CO_2 partial pressures of one atmosphere and less, were 0.71 for resin char and 0.60 for Wyodak coal char.

Obviously, the apparent reaction order varies considerably with the nature of the char and gasification conditions, which makes it difficult to compare data from various sources and predict/correlate reactivity. Moreover, most of the interpretive/correlative models are based on one or two-site models which tend to oversimplify the nature of char surfaces and mechanisms. Most chars exhibit distinctly energetically heterogeneous surfaces which can have a significant effect on the behavior of the apparent reaction order. For example, Calo and Perkins [8] demonstrated that surface heterogeneity can result in half-order behavior under certain conditions, and that the observed reaction order depends in a complex manner on the nature of the surface. For these reasons, here we focus on investigations of correlations between reactivity and populations of the intermediate oxygen surface complexes which desorb to gasify the char.

Figure 1 presents CO TPD spectra for resin char samples gasified in various CO_2/He mixtures. As shown, the broad desorption peak is centered at about 1010°C. The total amount of oxygen surface complexes increases with CO_2 partial pressure, but not homogeneously over the entire TPD spectrum. That is, the higher temperature surface complexes fall off more rapidly than the lower temperature complexes. These observations are consistent with those of Kapteijn *et al.* [9] who reported that increasing the CO_2 partial pressure from 0.1 to 1 atm increased the number of stable, higher temperature complexes more than the low temperature, unstable complexes.

Figure 2 presents the corresponding data for Wyodak coal char samples. The same qualitative behavior observed for resin char is readily apparent, although the desorption is peaked at a lower temperature of about 950°C. In addition, the total amount of oxygen surface complexes is about a factor of three or so greater than for the resin char.

The Rate-Controlling Step. It has been concluded by some workers that CO_2 gasification is

desorption rate-controlled [Marchon *et al.* [10]; Cerfontain *et al.* [11]; Chen and Yang [12]; Calo and Hall [13]; and Mentser and Ergun [2]. However, Kapteijn *et al.* [9] contend that for uncatalyzed CO_2 gasification, two processes are operative: (1) the decomposition of semiquinone/carbonyl surface complexes; and (2) the decomposition of an "out-of plane" oxygen complex which can be formed upon oxidation by CO_2 of a saturated carbon atom adjacent to an edge carbon which is already bonded to an oxygen atom. This latter type of oxygen complex has been shown to cause a substantial weakening of neighboring carbon-carbon bonds, and its decomposition results in the formation of a gas phase CO molecule and a semiquinone-type surface complex. This model explained their step-response data quite well, and supports the earlier mechanistic reasoning of Blackwood and Ingeme [5]. It was also concluded that the relative contribution of the two processes to the gasification rate is controlled by the CO_2 partial pressure.

In order to address the issue of the rate-controlling step in the current work, the following types of experiments were performed. Following gasification, samples were rapidly quenched to room temperature in either pure helium or the reactive gas mixture. This was done to assess whether or not the surface was saturated with oxygen surface complexes at gasification conditions. It was reasoned that if the gasification reaction was not controlled by the desorption step, unoccupied active sites would exist which by cooling in the reactant mixture would form additional oxygen surface complexes as the temperature decreased. Consequently, the resultant TPD spectra would differ from those obtained following rapid quenching in helium.

In Figure 3 are presented the corresponding desorption spectra for resin char following gasification in 1 atm of CO_2. As shown, the two spectra are practically identical. This result implies that gasification in pure CO_2 for resin char under these conditions is indeed desorption rate-controlled. However, as shown in Figure 4, the corresponding spectra following gasification in a 60/40 CO_2/He mixture yielded distinctly different TPD spectra. As shown, the principal difference lies in the low temperature surface complex populations. That is, the CO desorption over the temperature range between 600 and 900°C for the sample cooled down in the reaction mixture is greater than that for the sample cooled in He. This result is interpreted to mean that unoccupied active sites exist during the steady-state gasification in the 60/40 CO_2/He mixture under these conditions. These unoccupied active sites remained unoccupied when the samples were cooled down in He, but were populated with oxygen complexes in cooling down in the reaction mixture. Consequently, it is concluded that gasification departs from desorption rate-control as the CO_2 partial pressure decreases from 1 atm.

Distribution of Desorption Activation Energies. The observation that the population of oxygen surface complexes does not decrease evenly over the entire TPD spectrum suggests that the char surface exhibits a distribution of desorption activation energies. Du *et al.* [14] and Calo and Hall [13] have developed distributed activation energy models for the desorption of oxygen surface complexes from carbons following O_2 and CO_2 gasification. In the current work, the distribution of desorption activation energies was calculated using the method described by Calo and Hall [13]. The relationship between the instantaneous CO desorption rate and the distribution of desorption activation energies can be expressed as:

$$d[CO]/dt = [C-O]_0 S(E^*)dE^*/dt \qquad [1]$$

where E^* is the local desorption activation energy, as approximated by an instantaneous step at energy E^*, $S(E^*)$ is the desorption activation energy probability density function, $d[CO]/dt$ is the desorption rate of oxygen surface complexes as CO during TPD, and $[C-O]_0$ is the total initial (i.e. prior to the initiation of desorption) amount of CO-evolving oxygen surface complexes on the surface. Based on the classical work of Redhead [15], the parameters are related by:

$$E^*/RT = \ln [\upsilon_0 T/\beta] - 3.64 \qquad [2]$$

which holds for for $10^8 < \upsilon_0/\beta < 10^{13}$ (K^{-1}), where υ_0 is the pre-exponential factor for the desorption rate constant, T is the temperature, and β is the heating rate. Since a TPD experiment gives the instantaneous desorption rate directly, and dE^*/dt can be obtained from Eq. [2], the distribution of desorption activation energies, $[C-O]_0 S(E)^*$, can be determined from Eq. [1].

The value of the pre-exponential factor, υ_0, was assumed to be a constant. A series of TPD runs was performed at various heating rates from 25K/min to 100K/min for the same oxidized char samples. It was determined that a value of $\upsilon_0 = 10^{10}$ min^{-1} yielded the best fit in that it produced essentially the same energetic distribution for all the heating rates. This proved to be the best value for both resin and Wyodak char. Consequently, this value was used for the determination of the distributions of desorption activation energies.

Figure 5 presents the resultant desorption activation energy distribution for Wyodak coal char gasified in various CO_2/He mixtures. As can be seen, as the CO_2 partial pressure during gasification decreases, the desorption activation energy distribution of the char also changes.

The same trend was also found for resin char samples gasified in various CO_2/He mixtures. In comparison to the results for Wyodak coal char, the energetic distributions of oxygen surface complexes for the resin char samples are shifted to higher energies. It is also noted that mineral matter (most probably calcium) in the Wyodak coal char plays a significant role in determining the population of the low temperature surface complexes which turn over most rapidly during gasification. The absolute amount of the low temperature oxygen surface complexes is much higher for Wyodak coal char than for the resin car, which contains no mineral matter. Therefore the mineral matter in the Wyodak coal char "catalyzes" the formation of low desorption activation energy surface complexes. This represents the basis of the catalytic effect in this char. This is the principal reason that the reactivity of Wyodak coal char is significantly greater than that for resin char even at lower gasification temperatures.

Correlation of Reactivity. For conditions where the gasification rate is desorption rate-controlled, the reactivity can be correlated using the distribution of desorption activation energies. This is accomplished by integrating the desorption rate over the entire distribution:

$$r = \int_0^\infty \upsilon_0 \exp(-E^*/RT) \, [C-O]_0 S(E^*) dE^* \qquad [3]$$

Figure 6 presents a parity plot of predicted *vs.* measured reactivities for Wyodak coal char in one atmosphere of CO_2 as a function of temperature, as determined from Eq. [3] using the desorption activation energy distribution obtained at 825°C. As shown, the agreement is reasonably good. Similar results were obtained for resin char. Therefore, it can be concluded that the correlation of reactivity with the TPD desorption rate is feasible.

SUMMARY AND CONCLUSIONS
The objective of this work was to explore the relationship among reactivity, CO_2 partial pressure, and post-reaction TPD spectra. The results show that CO_2 partial pressure has a significant effect on the population of oxygen surface complexes for both resin and Wyodak coal chars. Generally, the oxygen surface coverage increases with increasing CO_2 partial pressure. It was also determined that gasification reactivity is desorption rate-controlled in 1 atm of CO_2 for both chars. However, as the CO_2 partial pressure decreases, the formation rates of surface complexes become comparable to the desorption rates, and the reaction rate begins to deviate from desorption rate-control.

For heterogeneous char surfaces, the distribution of desorption activation energies can be determined from TPD desorption rates. Prediction/correlation of reactivities from the desorption activation energy distribution is shown to be feasible for the carbon-CO_2 reaction operating under desorption rate-controlled conditions for both resin and Wyodak coal char.

It is possible that the most labile, low temperature oxygen surface complexes that are observed to increase in concentration with increasing CO_2 partial pressure may be of the type hypothesized by Kapteijn *et al.* [9] and Chen *et al.* [16], as being formed by the interaction of CO_2 with existing surface complexes. If this is so, then the thermal desorption methods applied here would reveal a shift or interconversion between labile and stable complexes with increasing pressure. This is a subject of continuing studies.

REFERENCES
1. Vorres, K.S., Users Handbook for the Argonne Premium Coal Samples, ANL/PCSP-93/1, DOE, Argonne, Il, 1993.
2. Mentser, M., and S,. Ergun, *US Bur. Mines Bull.* 644 (1973).
3. Turkdogan, E. T. and Vinters, J. V., *Carbon* 7, 101, (1969).
4. Koenig, P. C., Squires, R. G. and Laurendeau, N. M., *Carbon* 23, 5, 531 (1985); *Fuel* 65, 412 (1986).
5. Blackwood, J.D., and A.J. Ingeme, *Aust. J. Chem.* 13, 194 (1960).
6. Johnson, J.L., *Kinetics of Coal Gasification*, Wiley, NY, 1979.
7. Golovina, E.S., *Carbon* 18, 197 (1980).
8. Calo, J.M. and Perkins, M. T., *Carbon* 25, 395 (1987).
9. Kapteijn, F., R. Meijer, J.A. Moulijn, and D. Cazorla-Amorós, *Carbon* 32, 1223 (1994).
10. Marchon, B., Tysoe, W.T., Carrazza, J., Heinemann, H., and Somorjai, G.A., *J. Phys. Chem.* 92, 5447 (1988).
11. Cerfontain, M.B., Meijer, R., Kapteijn, F., and Moulijn, J.A., *J. Catal.* 107, 173 (1987).
12. Chen, S. G. and Yang, R. T., *J. Catal.* 138, 12 (1992); 141, 102 (1993).
13. Calo, J.M: and P.J. Hall, in *Fundamental Issues in the Control of Carbon Gasification Reactivity*, J. Lahaye and P. Ehrburger, eds, NATO ASI Series, Series E: Applied Sciences, Vol. 192, p. 329, Kluwer Academic Publishers, Dordrecht, 1991.
14. Du, Z., A.F. Sarofim, and J.P. Longwell, *Energy & Fuels* 4, 296 (1990).
15. Redhead, P.A., *Vacuum* 12, 203 (1962).
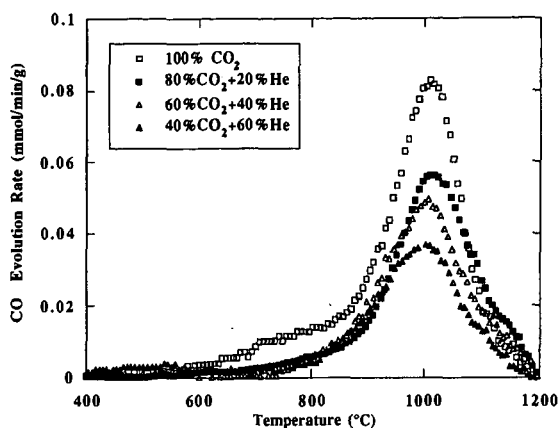16. Chen, S.G., R.T. Yang, F. Kapteijn, and J.A. Moulijn, *IEC Res.* 32, 2835 (1993).

Figure 1. CO TPD spectra from resin char gasified in 1 atm of CO_2/He mixtures at 900°C to 5% burn-off.
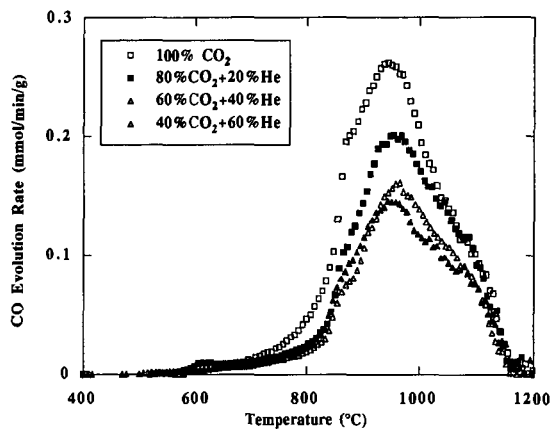

Figure 2. CO TPD spectra from Wyodak coal char gasified in 1 atm of CO_2/He mixtures at 825°C to 20% burn-off.
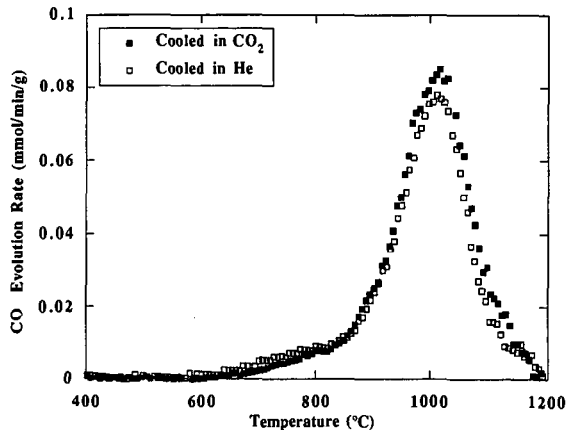

Figure 3. CO TPD spectra from resin char gasified in 1 atm of CO_2 at 900°C to 5% burn-off, following quenching in helium and CO_2.
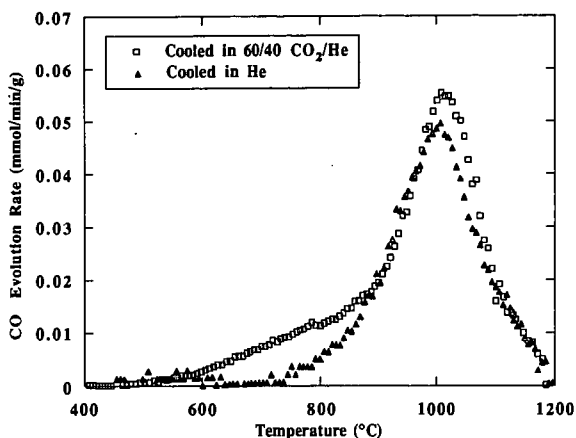
Figure 4. CO TPD spectra from resin char gasified 60/40 CO_2/He at 1 atm, 900°C to 5% burn-off, following quenching in helium and CO_2.
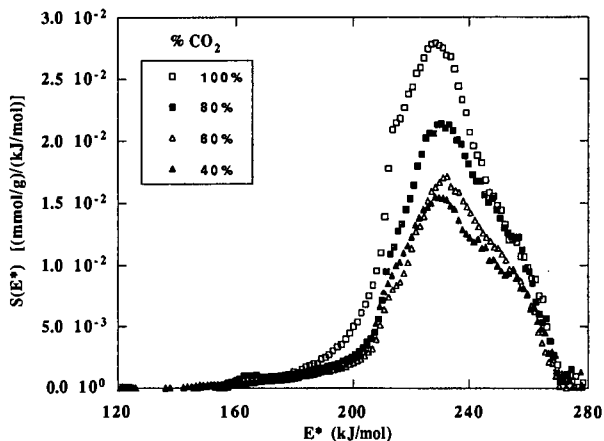

Figure 5. Distributions of desorption activation energies from TPD spectra presented in Figure 2 for Wyodak coal char gasified in CO_2/He mixtures at 825°C, 1 atm to 20% burn-off.
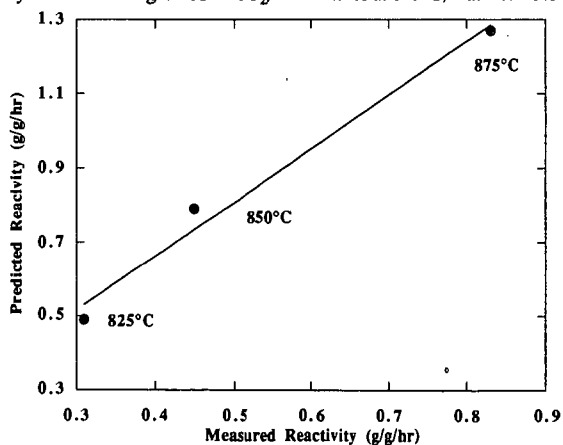

Figure 6. Predicted *vs.* measured reactivities for Wyodak coal char gasified in 1 atm of CO_2 to 20% burn-off.

ON THE ROLE OF CARBON-OXYGEN SURFACE COMPLEXES
IN THE CARBON/OXYGEN REACTION MECHANISM

K. Skokova and L. R. Radovic
Fuel Science Program
Department of Materials Science and Engineering
The Pennsylvania State University, University Park, PA 16802

KEYWORDS: carbon, gasification, oxygen complexes

INTRODUCTION

In the past, attempts to characterize the reactivity of carbon materials have led to conclusions regarding the importance of active sites and carbon-oxygen (C(O)) complexes in the carbon/O_2 reaction mechanism [1,2]. More recently, questions have been raised concerning the possibility of oxygen presence on the basal plane during gasification. Studies with disordered (turbostratic) carbons (e.g., polymer-derived carbons and coal chars) revealed that the quantity of C(O) complexes on the surface at gasification conditions exceeds significantly the quantities formed during low-temperature chemisorption [3-5]. One of the possible mechanistic explanations for this experimental fact is the so-called "spillover effect" whereby oxygen atoms, chemisorbed on the edge sites of carbon crystallites, migrate ("spill over") from the edges to the basal plane [5]. Spillover is the process that occurs when active species, C(O) complexes, are formed on one type of sites (e.g., edges), and are subsequently transferred to another type of sites (e.g., basal plane). Although the basal plane does not participate directly in carbon gasification, it serves as an additional reservoir of oxygen. A larger quantity of oxygen resides on the surface at higher temperatures, because spillover is an activated process.

Since it is rather difficult (or even impossible) to trace the fate of oxygen atoms on the basal plane by experimental techniques, theoretical molecular orbital calculations seem to be very attractive. Results of such calculations [6-11] have shown that there are no obstacles for the presence of oxygen atoms on the basal plane at temperatures at which gasification of carbon takes place.

Yang and Wong [12] were the first to provide experimental evidence for the presence and mobility of oxygen on the basal plane. Pan and Yang [10] have reiterated that basal-plane oxygen should be taken into consideration in the analysis of high-temperature CO desorption spectra. More recently, Chen *et al.* [11] showed that an oxygen atom on the basal plane lowers the binding energy of a neighboring C-C bond by 30%; therefore, it is important for the analysis of carbon reactivity. In our previous paper [13], a reaction mechanism was proposed according to which the quantity of basal-plane oxygen determines the CO/CO_2 product ratio.

The objective of the present communication is to pursue a further understanding of the role of basal-plane and edge C(O) complexes in the formation of CO and, especially, CO_2. Both theoretical and experimental techniques were used.

MECHANISM OF CO AND CO_2 FORMATION

The proposed mechanism of CO and CO_2 formation (Figure 1) follows from the reaction mechanism discussed in Ref. [13]. Carbon monoxide forms *via* decomposition of a C(O) complex at the edge of a carbon crystallite. Carbon dioxide, which is known to be a primary reaction product [14], forms by interaction and simultaneous decomposition of adjacent edge and basal-plane C(O) complexes. Formation of CO requires cleavage of two C-C bonds and is straightforward. The transition-state complex for CO_2 formation is more complicated; it requires the simultaneous cleavage of three bonds (two C-C and one C-O bond) and the formation of one C-O bond.
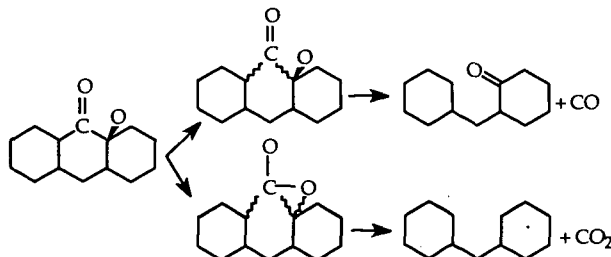

Figure 1. Proposed mechanism for CO and CO_2 formation in the C/O_2 reaction.

MOLECULAR ORBITAL CALCULATIONS

The objective of these computer simulations is to assess how the activation energy for C-C bond dissociation depends on the quantity and nature of surrounding $C(O)$ complexes. The results of such calculations allow us to estimate the relative changes in the rates of CO and CO_2 formation as the concentration of edge and basal-plane oxygen atoms changes. In addition, bond energies for oxygen atoms on the basal plane were calculated in order to show that basal-plane oxygen can indeed exist on the surface at reaction conditions.

The calculations were performed using a molecular orbital theory package (MOPAC 5). The PM3 semiempirical parametric method with unrestricted Hartree-Fock Hamiltonian was used. A seven-ring structure (coronene) was chosen as a model for the carbon surface. The edges were saturated with either hydrogen or oxygen atoms (Figure 2). In addition to the basic structures a, b and c, structures with oxygen on the basal plane in various positions were considered. With the aid of MOPAC, the geometries of each model structure were optimized, and heats of formation of the resulting structures were calculated.

The bond energy of oxygen on the basal plane was calculated as an enthalpy change in the hypothetical reaction of oxygen atom removal from the surface. The resulting bond energies of the basal-plane oxygen in different positions are shown in Table I. It appears that the most stable position of oxygen is between two carbon atoms, rather than right above a carbon atom. This is in agreement with the findings of other authors [6-10]; the absolute values of bond energies are also in agreement with the literature data [7-9]. The rather large bond energies indicate that the basal-plane complex could be present on the surface, and should be included in the reaction mechanism.

Figure 3 shows how the heat of formation of several model structures changes as the distance between carbon atoms 1 and 2 increases and the coordinates of all atoms except 1 and 2 are allowed to relax. The smallest distance corresponds to the unbroken C1-C2 bond, and the largest distance corresponds to the broken C1-C2 bond (zero bond order). The point of maximum energy corresponds to the geometry of a transition-state complex. The difference between the heats of formation of the transition-state complex and the initial structure is equal to the activation energy of the C1-C2 bond cleavage reaction.

As the quantity of both edge and basal-plane $C(O)$ complexes increases, the stability of the C-C bond is seen to decrease. For example, upon addition of a second edge oxygen atom, the activation energy of C1-C2 bond cleavage decreases from 64.7 kcal/mol (structure b) to 48.9 kcal/mol (structure c); similarly, it decreases from 30.7 kcal/mol for structure b_1 to 5.5 kcal/mol for structure c_1. More dramatic changes occur when additional basal-plane oxygen accumulates on the surface. The potential barrier diminishes from 64.7 to 30.7 kcal/mol (structures b and b_1, respectively), and from 48.9 to 5.5 kcal/mol (structures c and c_1, respectively). This result is in agreement with the important experimental fact that the activation energy for oxygen complex removal decreases as the surface coverage increases [15,16].

As it follows form the reaction mechanism shown in Figure 1, cleavage of the C1-C2 bond is a reaction path for CO formation. Therefore, the above results imply that the activation energy for CO formation decreases and the CO formation rate increases with increasing population of both edge and basal-plane oxygen on the surface.

Unfortunately, because of their complexity, no molecular orbital calculations of the potential barrier for CO_2 formation were done to date, and the influence of $C(O)$ complexes on the rate of CO_2 formation was not determined. However, some speculative conclusions can be made on the basis of stability of the C1-C2 bond. Calculations show that for structures with basal-plane oxygen (b_1 and c_1), C1-C2 bond cleavage is an exothermic reaction; therefore, it is probably favored thermodynamically. For structure c_1, the exothermicity of bond cleavage together with a low activation energy (5.5 kcal/mol) implies that this structure is not very stable, and its transition to the structure with the broken C1-C2 bond is more favorable. This in turn suggests that structure c_1 does not give any CO_2 upon its decomposition. This will enhance the above mentioned relative increase in CO formation as the amount of oxygen on the surface increases.

In conclusion, the addition of edge oxygen to structure b_1 and addition of basal-plane oxygen to structure c both lead to an increase in the CO/CO_2 ratio in the products of decomposition of $C(O)$ complexes present on the surface. In the next section, these predictions are compared with experimental results.

EXPERIMENTAL RESULTS AND DISCUSSION

In this section, the relative amounts of CO and CO_2 in the temperature-programmed desorption (TPD) patterns of two different carbon samples are analyzed as a function of the quantity of C(O) complexes on the surface.

Carbon samples were prepared by carbonization of petroleum pitch and cellulose at 1000 °C. Samples were oxidized at 600 °C in a mixture of 20% O_2/80% Ar until ~20% burnoff, and then cooled to room temperature at the fastest possible rate (~100 °C/min in the beginning of cooling) either in O_2 or in Ar. After cooling and without any exposure to air, the samples were analyzed by TPD. The products of surface oxygen complex decomposition were monitored by a quadrupole mass spectrometer.

The procedure of cooling the samples in different atmospheres allows one to prepare samples with different surface concentrations of C(O) complexes, while preserving the same total surface area; so the effect of surface area variations is minimized. During the cooling stage in O_2, chemisorption of oxygen produces additional C(O) complexes on the surface. Since gasification is not taking place, these complexes remain on the surface and are revealed in the subsequent TPD analysis. During the cooling stage in the inert gas, no additional oxygen chemisorption occurs; instead, desorption of the least stable (reactive) C(O) complexes takes place.

The TPD spectra of two pitch-based carbon samples are presented in Figure 4. In agreement with the work of Ranish and Walker [17] and Lizzio et al. [4], the sample cooled in O_2 has a much higher amount of oxygen on the surface; it also has a higher amount of CO in the decomposition products. Very similar results were obtained for two cellulose-based samples (Figure 5); although the total amount of C(O) complexes is much less dependent on the manner of cooling, the CO/CO_2 ratio is again higher for the sample that was cooled in O_2.

Therefore, the CO/CO_2 ratio in the products of TPD increases as the quantity of surface oxygen increases. This result is in excellent agreement with the results of molecular orbital calculations. An increasing amount of oxygen on the surface would lead to a larger proportion of structures of type c_1 relative to b, b_1 and c, of structures c relative to b, and of structures b_1 relative to b. According to the molecular orbital calculations discussed previously, all of this would lead to an increasing quantity of CO in the products of decomposition of these complexes.

It is important to emphasize that the observed increase in the CO/CO_2 ratio (in the products of TPD) with increasing quantity of C(O) complexes is exactly the opposite to what is commonly observed during carbon gasification in O_2. In agreement with the literature data [2], we have found that the CO/CO_2 ratio decreases as the total amount of C(O) complexes increases during gasification in O_2. In order to explain these different trends, which are thought to contain important mechanistic clues [18], further investigation of the effects of surface oxygen on O_2 chemisorption vs. C(O) complex decomposition is needed.

REFERENCES

1. Laine, N. R., Vastola, F. J., and Walker, P. L., Jr., *J. Chem. Phys.* **67**, 2030 (1963).
2. Phillips, R., Vastola, F. J., and Walker, P. L., Jr., *Carbon* **7**, 479 (1969); **8**, 205 (1970).
3. Taylor, R. L., Ph.D. Thesis, Penn State University (1982).
4. Lizzio, A. A., Jiang, H., and Radovic, L. R., *Carbon* **28**, 7 (1990).
5. Walker, P. L., Jr., Taylor, R. L., and Ranish, J. M., *Carbon* **29**, 411 (1991).
6. Bennett, A. J., McCarroll, B., and Messmer, R. P., *Phys. Rev. B* **3**, 1397 (1971).
7. Hayns, M. R., *Theoret. Chim. Acta* **39**, 61 (1975).
8. Barone, V., Lelj, F., Iaconis, E., Illas, F., Nino, R. and Jounou, A., *J. Mol. Struct.* **136**, 313 (1986).
9. Fromherz, T., Mendoza, C., and Ruette, F., *Mon. Not. R. Astron. Soc.* **263**, 851 (1993).
10. Pan, Z., and Yang, R. T., *Ind. Eng. Chem. Res.* **31**, 2675 (1992).
11. Chen, S. G., Yang, R. T., Kapteijn, F., and Moulijn, J. A., *Ind. Eng. Chem. Res.* **32**, 2835 (1993).
12. Yang, R. T., and Wong, C. J., *J. Chem. Phys.* **75**, 4471 (1981).
13. Skokova, K., and Radovic, L. R., Proc. 22nd Biennial Conference on Carbon, 1995, San Diego, CA, p. 608.
14. Hart, P. J., Ph.D. Thesis, Penn State University (1966).
15. Vastola, F. J., Hart, P. J., and Walker, P. L., Jr., *Carbon* **2**, 65 (1964).
16. Ahmed, S., and Back, M. H., *Carbon* **23**, 513 (1985).
17. Ranish, J. M., and Walker, P. L., Jr., *ACS Preprints (Div. Fuel Chem.)* **32**(4), 132 (1987).
18. Ranish, J. M., and Walker, P. L., Jr., *Carbon* **31**, 135 (1993).

Table I. Bond energies of oxygen atom on the basal plane in different positions, in kcal/mol.

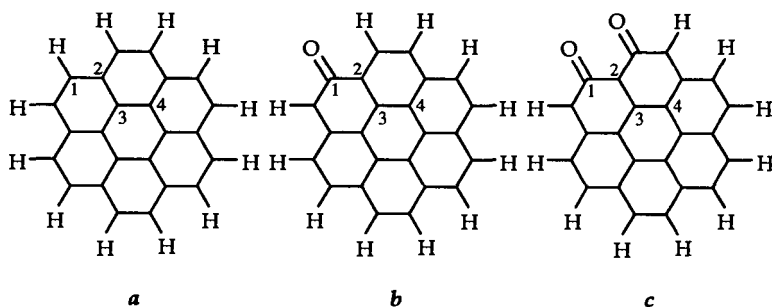| Structure	Position of oxygen on the basal plane			
	above C2	between C2 & C3	above C3	between C3 & C4
a	29.0	39.7	25.8	35.9
b	38.6	45.8	26.5	37.1
c	68.6	63.6	37.7	49.3

Figure 2. Model carbon structures used for molecular orbital calculations.
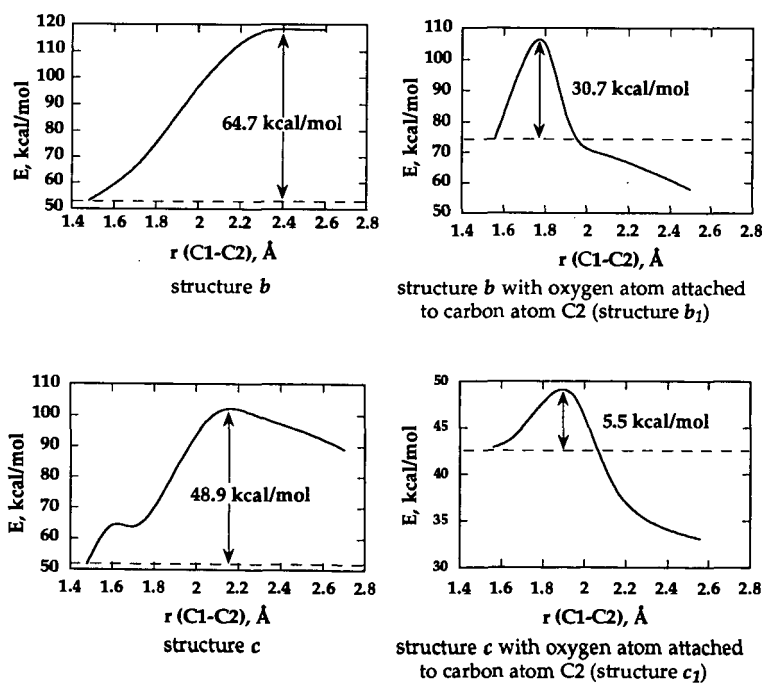

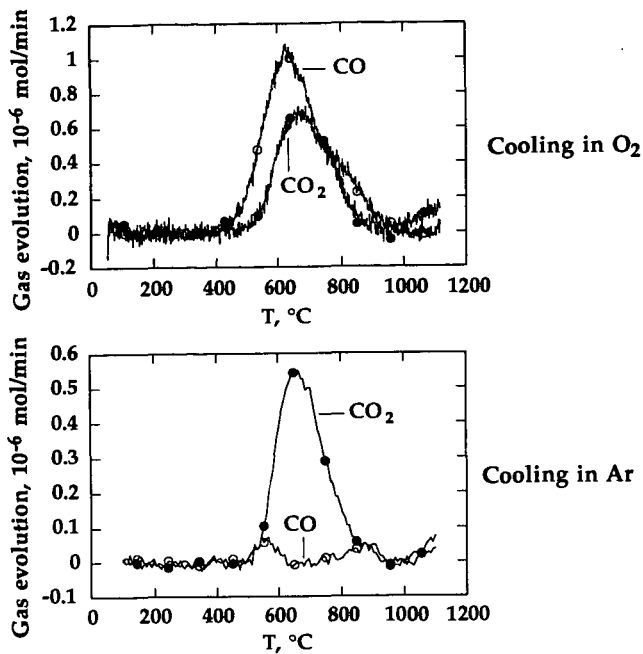**Figure 3.** Potential curves for the reaction of C1-C2 bond cleavage.

146

Figure 4. TPD profiles of petroleum pitch-derived carbon after gasification in O_2 until 20% burnoff followed by cooling in O_2 or Ar.
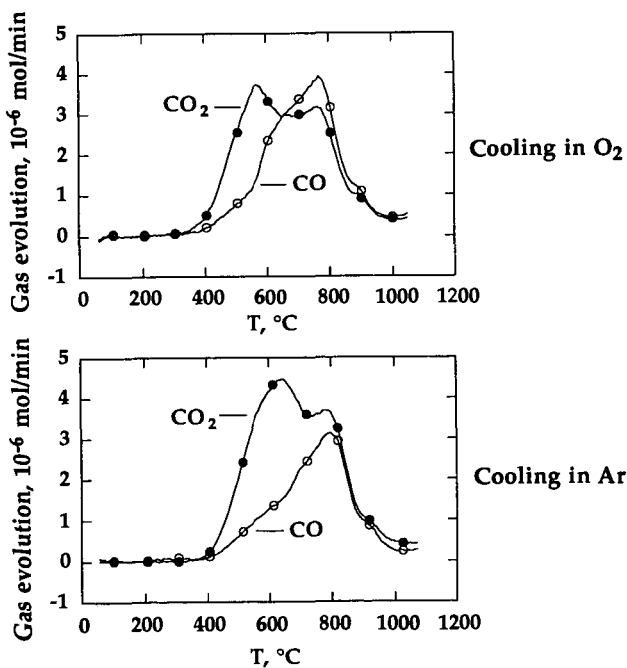

Figure 5. TPD profiles of cellulose-derived carbon after gasification in O_2 until 20% burnoff followed by cooling in O_2 or Ar.

ON THE RELATION BETWEEN STRUCTURE AND REACTIVITY IN THE CARBON OXYGEN REACTION

D. Herein, J. Find, B. Herzog, H. Kollmann, R. Schmidt, R. Schlögl
Fritz Haber Institut der Max Planck Gesellschaft,
Faradayweg 4-6, D- 14195 Berlin, FAX -4930-8413-4401
H. Bartl
Institut für Kristallographie der Universität Frankfurt,
Senckenberganlage 30, D- 60054 Frankfurt,
Ch. Troyer
Institut für Analytische Chemie, Technische Universität Wien
Neubaugeb. 5/11 A-1070 Wien

INTRODUCTION

The oxidation of graphite is a reference process for both generation of energy by combustion and for fundamental aspects of gas-solid interface reactions. The absence of large perfectly ordered crystals of graphite render rigorous model studies under surface science conditions very difficult despite the significant efforts in this area with large synthetic graphite surfaces(1). With integral kinetic techniques such as TPRS and instationary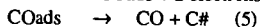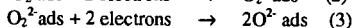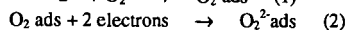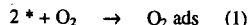 kinetic data a detailed mechanistic picture has been develloped in a longstanding effort introducing a fraction of the geometric surface as active surface and the competition of two types of oxygen surface complexes which are either static and hence inhibiting or mobile and hence reactive in gasification(2,3,4). In addition, the selectivity to CO and CO_2 was traced back to different types of reactive surface intermediates with carbonyl or lactone structures respectively(5). The present contribution is an attempt to investigate the reaction with experiments aimed at selected atomistic aspects of the mechanistic picture. In a previous study the gasification of HOPG was found to procede at low temperatures (200 K) and low oxygen partial pressures (10^{-5} mbar) on suitably prepared surfaces (6). In this work as well as in many other reports(1,2,5) the importance of defects was pointed out which are either present in the substrate or may be created during reaction. In the model experiment (6) self-passivation occured after very little conversion due to the creation of strongly adsorbed oxygen inhibiting low-temperature oxidation. The existence of strongly adsorbed oxygen and weakly adsorbed oxygen (2,3,7) in two different bonding geometrics is a common ingredient to kinetic models of graphite oxidation.

Graphite oxidation is the prototype of a topotactic reaction proceeding only at the prism faces which should lead to a uniform shrinkage of the individual particles in uncatalysed reaction. Parallel to the recession mechanism there are basal plane defects which cause pitting corrosion creating additional prismatic faces during gassification and contribute in a difficult to control way to the overall rate. Other types of defects pin the edge recession e.g. by the occurence of local sp^3 bonding leading to a continous change in the length of the reaction interface and the creation of micro-hills (8) on reacting surfaces.

We used large flakes of RFL (0.5-1.2 mm dia.) and powders AF (3-1-μm dia.) natural graphite from Kropfmühl (Bavaria) which was purified from silicate and metal residues by basic melt and acid leaching. Standard gassification conditions were 20% oxygen in nitrogen and 927 K reaction temperature.

Modelling of the reaction is necessary to link macroscopic rate observations which are often severely affected by mass- and energy transport limitations with a minimum set of elementary step reactions describing the overall process:

$$2 * + O_2 \quad \rightarrow \quad O_2 \text{ ads} \quad (1)$$
$$O_2 \text{ ads} + 2 \text{ electrons} \quad \rightarrow \quad O_2^{2-} \text{ads} \quad (2)$$
$$O_2^{2-} \text{ads} + 2 \text{ electrons} \quad \rightarrow \quad 2O^{2-} \text{ ads} \quad (3)$$
$$C\# + O^{2-} \text{ ads} \quad \rightarrow \quad CO \text{ads} + 2 \text{ electrons} + * \quad (4)$$
$$CO \text{ads} \quad \rightarrow \quad CO + C\# \quad (5)$$
$$CO \text{ads} + O^{2} \quad \rightarrow \quad CO_2 \text{ads} + 2 \text{ electrons} + * \quad (6)$$
$$CO_2 \text{ ads} \quad \rightarrow \quad CO_2 + C\# \quad (7)$$
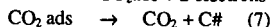
These steps of reductive activation and carbon oxidation at a suitable defect(#) comprise the minimum number of reaction steps for the overall oxidation. It is evident that besides the reaction centre a second type of chemisorption site (*) is required for the reductive activation of oxygen which must exhibit an excess of delocalised electrons such as at the basal planes. These terrace sites are, however, unreactive for the nucleophilic activation product which implies the surface diffusion of the activated species. Some of these steps are different when homolytically activated oxygen from chemical or physical sources is involved (9). In this case, however, the topotactic reaction behaviour is lost. A key issue is the exact chemical nature and the location of the two types of active sites.
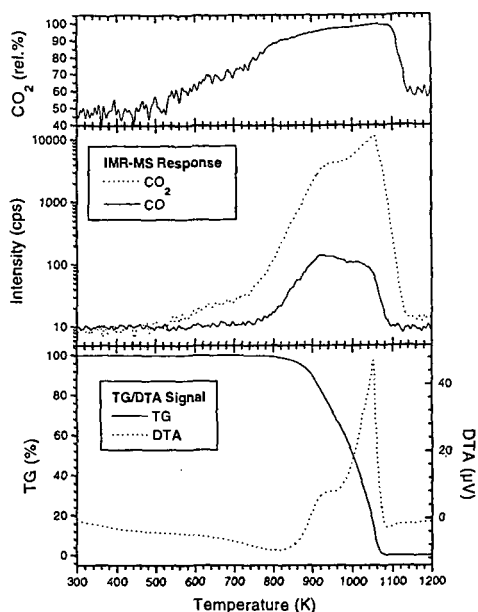
Fig.1: Selectivity, yield and TG/DTA response of an integral reaction experiment at standard conditions of a 0.5 cm bed composed of a 3:1 mixture of AF graphite with SiC powder in a coupled TG-IMR-MS experiment.

In Fig.1 we summarise macroscopic kinetic observations of a gassification experiment of AF graphite in an integral reactor. Sufficient dilution with silicon carbide ensured the presence of molecular oxygen at the reactor outlet at all temperatures applied. A special mass spectrometer of the IMR-MS ionisation type is applied for sensitive detection of CO and CO_2 without fragmentation overlap. Both the changes in selectivity and in rate (proportional to the DTA signal) indicate that the above reaction scheme is insufficient to explain the reaction progress in this case. The increase in CO_2 selectivity in the low-temperature regime complies with the initial removal of pre-formed C-O insertion structures. The second increase in CO_2 at high conversion would mean that the insertion of active oxygen in suitably defective carbon-carbon structures becomes increasingly dominating over the addition of active oxygen onto unsaturated edge sites. This can be seen as consequence of the increasing abundance of mobile surface atomic oxygen (4) creating a high virtual pressure of oxygen. The di-oxygen partial pressure and the increasing abundance of basal plane sites (C*) increase with burn-off in contrast to the decreasing abundance of oxidation sites (C#) due to the recession of prismatic faces.

Changes in rate and selectivity with burn-off were also observed in isothermal macroscopic experiments which were found to be critical in quantitative reproducibility. Thus it was felt that single particle gassification experiments should be useful. The alternative, to use less active reagents or to drastically reduce the temperature, may lead to better kinetic data but may not describe the reaction in the same kinetic state as it is characteristic for a practical combustion, i.e. a different reaction step may be rate-determining at low rates (10) than at higher rates.
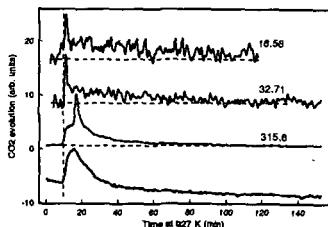
RESULTS

Fig.2: IMR-MS responses for single particle gassifications. The graphite weight in μg is used to designate the experiments. The top two traces refer to AF, the lower trace to RFL gassification. The unassigned trace is the water response for the RFL gassification. The vertical dashed line indicates the first time of constant oxygen partial pressure. At t=0 the heating in nitrogen was started. After reaching 927 K the gas was changed to oxygen in nitrogen. For the RFL experiment the oxygen was admitted in two steps at 11 and 20.5 min.

The simultaneous observation of the weight change and the gas evolution allowed to accurately fix the correct sample weight in single particle gassification experiments displayed in Fig. 2 which are heavily perturbed by bouyancy effects when starting the isothermal reaction after rapid heating in nitrogen. For AF oxidation a portion of the ceramic sample holder was dusted with graphite particles, for RFL single clean flakes (optical microscope) were used. In all cases after reaching a certain threshold partial pressure of oxygen a burst of reactivity occured which was followed by a continous activity at much lower level. For RFL graphite the threshold lies at about 5 vol% oxygen. Associated with the inital gassification is the desorption of water arising from oxidation of OH groups. The burst in reactivity is not connected with the creation of active sites from the OH group desorption as can be seen from the absence of a burst in the water trace. The data imply that an aged graphite surface is particularily reactive as the short duration of the burst excludes a location of the active centres underneath the surface.

149

The behaviour is reflected in the inital rates of reaction obtained from the weight change data. The observation that within the experimental accuracy both types of graphite with differing geometric surfaces gave comparable results indicates the integral character of the rate integrating over many processes and changes in local surface structure. Unexpected is the shape of the rate curve with time, as the initial gassification of a reactive surface followed by a steady state bulk reaction should not lead to a rate minimum which depends in its shape on type and mass of the graphite used. The characteristic time for reaching a constant rate is with about 120 min so long that a process of surface modification can be excluded. Moreover, comparison with the gas evolution data in Fig.2 reveals that the activity in gassification does not pass through a minimum but follows the expected behaviour. This implies that the weight change not only reflects the weight *loss* from gassification but indicates a simultaneous weight *gain* from the uptake of oxygen. Given that we are dealing with non-porous samples, the increase in weight cannot only be attributed to the formation of unreactive surface oxygen functions which can only cover a fraction of a monolayer (a monolayer of oxygen atoms on the geometric surface of a RFL flake would weigh about 0.002 µg, which is below the detection limit of the present experiment). We attribute the weight gain to the incorporation of oxygen in the bulk of the graphite sample. The effect is strongly dependent on temperature with a significant reduction in the detectable amount of incorporated oxygen with increasing temperature (less than 20% at 977 K compared to the amount at 927 K for RFL, for AF the effect is smaller than for RFL and so is the temperature dependence). The total amount of incorporated oxygen is with about 3 wt% of the RFL sample small enough to leave the question about its location in irregularities of the mosaic structure or as intercalate within the van-der Waals gaps of the regular crystallites. This will be discussed below.

STM can be used to reveal local details of the oxidation mechanism of graphite (8,11) as the reaction does not produce -as in metal oxidation reactions- scales of low electric conductivity. The extra high sensitivity of STM to roughness allows to image deviation from a planar surface with a sensitivity of 2-3 orders of magnitude higher than the lateral resolution of a survey image. This is illustrated in Fig.3 showing a RFL flake before gassification and the same flake after 20 % burn-off. The outer surface of the flake is rather irregular and exposes a high abundance of prismatic faces in form of micro-flakes sitting on top of the main particle. After partial gassification these micro flakes have all disappeared leaving a smooth surface with a considerably lower basal- to prism face ratio. It is noted that none of the steps seen in this image are monosteps. The minimum height is 3 steps and only odd numbers of graphene layers were observed to constitute these stable edges. The impression of the regularity is adventitious, there are many situations with irregular edges on the over 1200 images which were analysed. The different appearance of the steps in different directions is due to the uneven shape of the STM tip used for imaging. These tips have to be extra coarse in order to survive the frequent crashes which are unavoidable in imaging such rough surfaces. From these images it becomes apparent why gassification starts with a high initial rate as the intermixing of the two active centres of planar basal planes for oxygen activation and of rough prism faces for oxidation is much better than after removal of the microflakes. The images fit well to the integral observations of the rate measurements. The triangular rows in image 3C indicate the local interruption of the surface electronic conductivity by firmly held adsorbates such as strongly bound oxygen atoms decorating lines of defects in the partly gassified crystal. Ribbons of dislocations which are normally detected by TEM contrast (12) are exposed to atomic oxygen and provide centres for stable functional group formation. The absence of atomic resolution in oxidised areas can further be seen in image 3D which shows the rare situation (8 out of 1200) of the co-existence of insulating islands of non-graphitic nature such as „carbon oxide" or diamond-like carbon with normal surfaces separated by a double- and single-atomic step structure. These two latter images reveal the presence of lines and areas of basal planes which are non-graphitic in character and provide evidence for a local chemical heterogeneiety.

Imaging monoatomic steps on graphite is rarely possible on cleaved surfaces. On oxidised surfaces it is, however, possible in particular at monoatomic etch pits. Fig.4A shows a situation in which a top crystallite exhibits a 120 deg edge while sitting on a monoatomic step. At this level of resolution the high degree of orientation along crystallographic main directions can be seen in areas with low defect density. Most remarkable is the different appearance of the two prism faces (triatomic step height) in two different directions. The analysis of the effect as function of the STM parameters reveals that the „structure" in one prism face is an artefact caused by the absence of electrical conductivity. This precludes imaging of the atomic arrangement but reveals that the local chemistry of the two prism face orientations is different with the structured face being largely covered by covalently bound oxygen groups. The other edge seems to be free of insulating bonds and may thus represent a more reactive face. These assignments are speculative as the observations are not possible during gassification (4). It remains, however, the evidence for a local difference in chemical interaction of differently oriented prismatic faces.
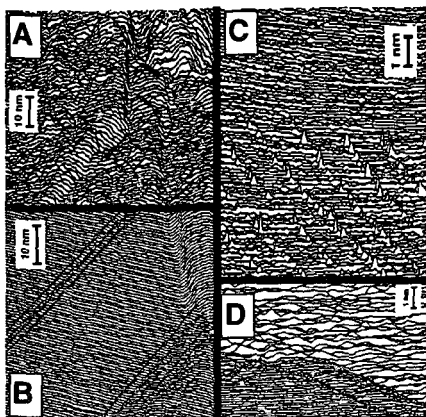
Fig.3: STM wide scans over a flake of RFL graphite before oxidation(A) and after 20% burn-off (B,C;D). A Burleigh ARIS 6000 instrument with a W tip was used: gap voltage + 50 mV, constant current 1.0 nA, raw data as line scans. Scan areas are: A,B: 300x300 nm, C:500x500 nm, D:50x50 nm

In image 4B the atomic resolution is illustrated of oxidised steps near a terminating basal plane defect. Two top graphene layers are sitting in different rotation angles relative to the supporting graphene layer. The fuzzy appearance of the steps is also due to an imaging artefact caused by a low electrical conductivity at the step edges. The striped appearance is a sign of the tip crashing into the step and requiring to travel over several atomic distances behind the steps to reach stable tunnelling conditions again. This is a strong indication of the presence of localised electronic states at the step edges and the absence of radicals or delocalised states at these locations. The presence of carbon-heterobonds (oxygen or hydrogen) is the likely explanation
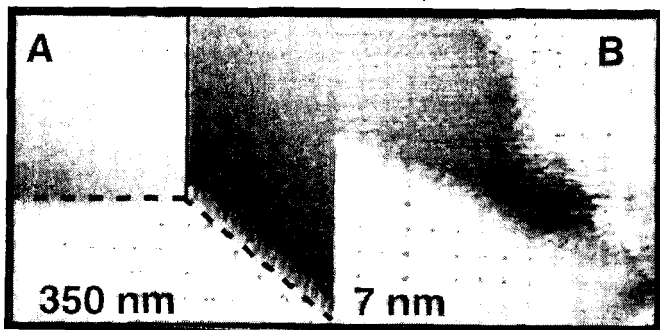

Fig.4: STM images of RFL after 50 % burn-off. In image A the dashed lines denote the contours of a top crystallite sitting over a plane with a monoatomic step (full line). In B the atomic resolution is achieved for oxidised monoatomic steps. The figures denote the lateral image size, the step heights were determined from profile scans (not shown). The imaging conditions were as in Fig.3.

which allows to experimentally support the chemical notion that the terminating graphene edges are the places of interaction between carbon and oxygen. This image reveals a possible zone of reactivity for addition (edges) and insertion (rows of atoms right behind the step) of activated oxygen. The formation of islands of modified carbon atoms within basal plane terraces as a consequence of gassification was not observed indicating that the spontaneous creation of gassification sites within perfect graphene sheets does not occur. This follows also from thermodynamics as the creation of the very first single vacancy requires 676 kJ/mol energy (13) whereas the produced CO_2 molecule contributes only 393 kJ/mole to the energy balance. The creation of vacancies becomes rapidly easier with defects already present (13). The necessity to have already an interruption in the graphene layer for the oxidation to procede, drives the reaction to clean basal planes (11) and to a topotactic progression along prism faces and along „a-priori" defect sites (4,14).

We failed to detect islands of oxygen at the terraces of the basal planes as they are seen in metal-oxygen interaction studies. This implies that the interaction of oxygen with the basal planes which is required for its activation is too weak to allow imaging by STM or that the STM tip field is sufficient to clear the imaging area on the basal planes. We have shown by TDS that both water and oxygen are adsorbed on basal planes and that the failure to see these adsorbates is an STM artefact(8).

X-RAX DIFFRACTION EXPERIMENTS

For the observation of a gas-solid interface reaction the bulk-sensitive technique of X-ray diffraction should not provide any useful data as the reacting surface is not probed by the

experiment. In continuation of our single particle analysis of the reaction we studied RFL flakes by Laue photographs as function of burn-off. The results are summarised in Fig.5.
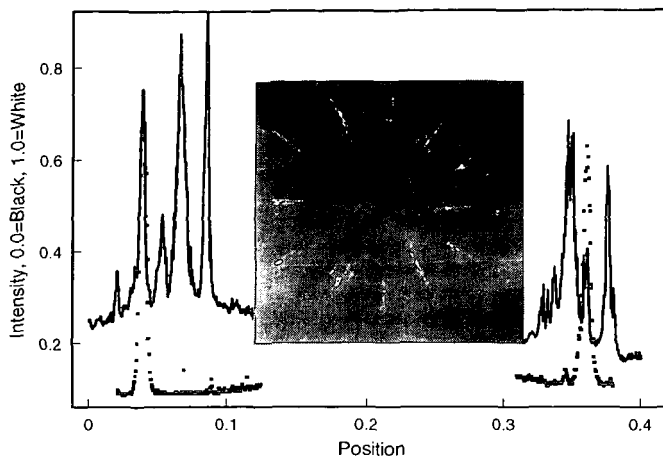

Fig.5. Laue Photographs (Mo kα radiation, beam parallel to the c-axis) of a RFL flake before oxidation (top densitometer trace and photograph) and after 20 % burn-off (bottom densitometer trace). It emerges very clearly that the flake was polycrystalline in (hk) orientation and became almost perfectly single crystalline after partial oxidation.

The data show that the flake was liberated from small crystallites throughout its volume. Moreover, the mosaic crystallites constituing the main part of the flake became better aligned in the basal plane (sharp profile after partial oxidation). This observation is corroborated by the fact that Laue patterns (parallel a,b) showing the stacking order could not be obtained before oxidation but revealed a high degree of AB stacking after partial burn-off. This indicates that partial oxidation causes a kind of „chemical annealing". The most defective crystallites will be burnt away preferentially and so will be interstitial carbon in the interior of the mosaic crystal. This requires the action of oxygen not only on the geometric surface but also at the inner surfaces of defective regions. This is seen in parallel to the small but detectable storage of oxygen in the initial phase of oxidation. We would thus locate the oxygen not as an intercalate in between the graphene galleries but rather as „bubbles" located at defects.

In-situ powder diffraction studies of the (002) reflection under standard gassification conditions were performed in order to support this interpretation. Intercalation, even in small quantities should lead like in residue compounds to a splitting and broadening of the (002) reflection. Initial experiments with HOPG as sample and Si as internal standard seemed indeed to support the notion about the residual intercalation (15). Frequent repetion of the experiment in different diffractometer geometries and with different graphite materials revealed, however, that the observed drastic changes in lineprofiles are diffraction artefacts caused by the uncontrolled sample movement exposing differently misaligned sections of the mosaic crystal to the diffraction condition. The lineprofile became increasingly symmetric and significantly narrower with progressing oxidation after removing this artefact. This is exemplified in Fig.6 The unsteady course of the difference curve at low temperatures indicates the residual positionning problems of the RFL sample. A persistent reduction of the linewidth close to the instrumental limit was observed after oxidation and cooling back to 300 K. The lattice constant was also observed to shrink irrevesibly after oxidation from the value of the Ar experiment which was found to be 340.12 (±0.03) pm at 873 K. The selectivity was also found to change with the structural parameters. The excess of CO_2 formation increased in parallel with the reducing FWHM and with the change in lattice spacing. In particular, the onset of all changes co-incided in all experiments suggesting a correlation of the effects. The defective structural parts gassify preferentially to CO, the better ordered graphitic carbon reacts preferentially to CO_2..

X-RAY ABSORPTION SPECTROSCOPY

The average local electronic structure is an important parameter in the reactivity scenario of the gassification as it provides information about the action of the di-oxygen activation as rate-determining step. XPS was found to be rather insensitive to the variation of carbon-carbon bonding within one type of graphite partly because of the photoemission physics and partly because of the ill-defined surface-sensitivity (16). This fact can be used advantageously in performing photoabsorption experiments at the carbon 1s edge using synchrotron radiation. In this experiment the insensitive photoemission process is the inital state allowing thus to interpret the spectra without having to account for initial state changes. The general shape of the spectra which allow cleary to discriminate π* states from σ* states has been discussed elesewhere(16, 17). In Fig.

152

7 some quantitative data about the π^* states are collected. A sample of HOPG was used for the reference experiment shown in the top panel. The changes in the polarisation of the π^* resonance
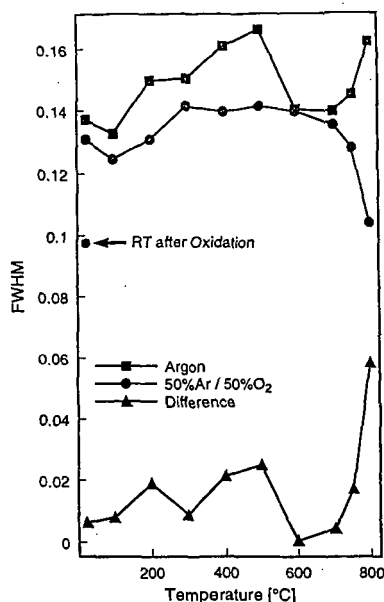

Fig.6: Evolution of the FWHM of the RFL graphite (002) reflection as function of in-situ treatment temperature. The data were obtained from Gaussian lineprofile fits. The difference plot proves the action of oxygen and not of temperature in the annealing procdure. The data were recorded after reaching steady state conversion at each temperature point in the oxidation scan and after 2h waiting under Ar respectively.

are compared for pristine, oxidised and Ar ion sputtered surfaces. Oxidation causes mainly a surface roughening by pitting giving rise to the small loss in polarisation at low angles between the light beam and the sample basal plane. The average electronic structure is, however, not different between pristine and oxidised graphite indicating that oxidation procedes on few sites on the surface and does not cover the surface with intermediate C-O groups. This precludes a significant reaction-induced increase in defect abundance. Sputtering of graphite with Ar ions destroys the surface and breaks many sp^2 bonds leaving a electronically highly disordered surface (18). This can also be seen drastically from the change in polarisation behaviour which indicates the loss of preferred orientation of the π^* orbitals (reduced slope) and the loss in abundance of sp^2 centers (smaller absolute value at high angles). This type of surface serves as model for a type of defects inhibiting oxidation by removing the delocalised electronic states required for the first three steps in the oxidation sequence. The fact that such an isotropic attack of the surface electronic structure does not occur during oxidation is a microscopic confirmation of the topotactic nature of the reaction requiring for its progression minority surface sites which are not located within the basal plane.

This technique is also suited to follow the evolution of the graphitic character with burn-off by examination of the intensity of the π^* resonance normalised to the carbon content as shown in the lower panel of Fig. 7. Changing the detection condition from total Auger yield to partial Auger yield allows to probe non-destructively the electronic structure depth-selective. The data show that with increasing burn-off the degree of graphitic surface increases both at the surface (topmost atomic layer) and in the bulk (some 10 nm). This is full in line with all other observations reported here and shows for a large area the „cleaning" effect detected by STM. It further shows that the oxidative bulk annealing reduces in the inital stage of gasification the abundance of non-graphitic carbon atoms.

CONCLUSIONS

The microscopic informations presented corroborate in general the traditional view about the reaction mechanism as a topotactic gas-solid reaction with two different active sites having to interact for efficient reaction. The prism faces seem to be chemically different according to their crystallographic orientation. They are, however, clearly the sites of carbon-heterobond formation. The consequence of the step is a pronounced modification of the electronic structure of the carbon atoms near the edge. These observations call for a structure-sensitivity of the reaction at different location of the active sites (e.g. variation after equations (5) and (6) of the mechanism). This would be in line with the picture of oxygen addition and insertion as being the elementary steps defining the selectivity. The conjecture that one of these reaction sites would mainly not be located near prism edges or „a-priori" defects is not supported by the data presented. The high thermal stability of the carbon heterobonds on an intact long-range-ordered prismatic edge (see Fig. 4) requires the overall high reaction temperature of the gasification in order to achieve steps (5) and (7) of the reaction sequence. Higher disordered reaction interfaces with an average lower carbon coordination number are benificial for a lower reaction temperature or a higher rate (Fig. 3).
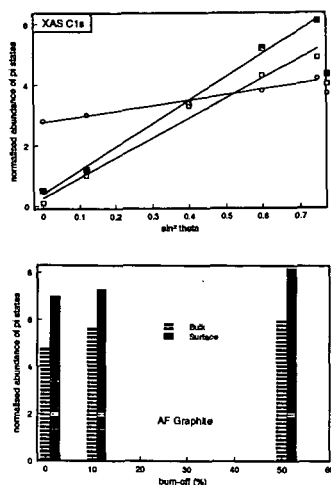
Fig. 7. Top: Angular dependence of the intensity of the 286 eV π^* resonance for differently prepared HOPG surfaces. Oxidation was performed in-situ under standard conditions which created a large amounts of etch pits. Ar ion bombardment was carried out at 1 kV and 10-4 mbar Ar for 2 min. XAS data were recorded in the total yield mode at the HE PGM II station at the BESSY synchrotron. The bottom panel shows the evolution of the π^* intensity with burn-off for AF graphite (external sample preparation). Surface sensitivity is created by comparison of total yield (0 eV, bulk) and partial yield (150 eV, surface) data.

The single particle experiments further gave evidence for the preferential burn-off of small crystallites with high initial rate covering the individual flakes. This process drives the reaction towards a state in which activation of chemisorbed di-oxygen according to reactions (1)-(3) is not rate-determining despite the overall small sticking coefficient of di-oxygen on graphite (001). This is taken as strong indication that the well-ordered basal planes provide active centers for reductive di-oxygen dissociation and exhibit a function in the gassification mechanism.

Incorporation of oxygen into graphite in weighable amounts was detected which is likely to be located in the voids of the mosaic crystal. It was not possible to produce unambigous structural evidence for regular intercalation of oxygen as islands between graphene layers. At the „internal" surfaces the oxygen removes preferentially lattice defects which allow oxidation-induced low-temperature annealing of the graphite crystal. The effect was detected by X-ray diffraction methods and by the observation of the action of mechanical forces providing activation energy for defect ordering (see Fig. 3 C). Careful oxidation of natural graphite flakes can lead to well-ordered samples.

Defects act on the gassification rate as promoters by interrupting the long-range electronic structure of the graphene edges or within the planes (pitting) without destroying the local electronic structure (Fig. 7) or as inhibitors by pinning the delocalised valence electrons within a few interatomic distances. The counteraction of these irregularities gives rise to an unpredictable rate of individual mosaic flakes. The generation of a sufficient number of defetcs to modify the surface electronic structure as detectable by a (small) change in average hybridisation or structural roughening was not observed.

ACKNOWLEDGEMENTS

REFERENCES

(1) S.R. Kelemen, H. Freund, Carbon 23, (1986), 619
(2) P.L. Walker jr., R.L. Taylor, J.M. Ranish, Carbon,29, (1991), 411
(3) J.A. Moulijn, F. Kapteijn, Carbon,33 (1995), 1155
(4) J.M. Ranish, P.L. Walker jr., Carbon, 31, (1993), 135
(5) R.N. Smith, D.A. Young, R.A. Smith, Trans. Faraday Soc., 62, (1966), 2280
(6) R. Schlögl, G. Loose, M. Wesemann, Solid State Ionics,43 (1190), 183
(7) B. Henschke, H. Schubert, J. Blöcker, F. Atamny, R. Schlögl, Thermochimica Acta,234 (1994), 53
(8) R. Schlögl, F. Atamny, J. Wirth, J. Stephan, Ultramicroscopy,42-44, (1992), 660
(9) H. Marsh, T.E. O'Hair, R. Reed, Trans. Faraday Soc., 61, (1965), 285
(10) I.M.K. Ismail, P.L. Walker jr., Carbon,27, (1989), 549
(11) L. Porte, D. Richards, P. Gallezot, J. Microscopy, 152, (1988) , 515
(12) M.M. Heerschap, P. Delavignette, Carbon, 5, (1967), 383
(13) A.P.P. Nicholson, D.J. Bakon, Carbon, 13, (1974), 275
(14) C. Roscoe, J.M. Thomas, Proc. Roy. Soc., A, London, 297 (1966), 397
(15) B. Herzog, D. Bokern, Th. Braun, R. Schlögl, Proc. EPDIC-3, European Conf. Powder Diffraction, (1993), 3
(16) F. Atamny, J. Blöcker, B. Henschke, R. Schlögl, Th. Schedel-Niedrig, M. Keil, A.M. Bradshaw, J. Phys. Chem., 96, (1992), 4522
(17) R. A. Rosenberg, P.J. Love, V. Rehn, Phys. Rev., B, 33 , (1986), 4034
(18) R. Schlögl, Surf. Sci., 189, (1987), 861

BEHAVIOR OF HIGHLY POROUS CHARS DURING OXIDATION IN REGIME I

Ezra Bar-Ziv
Department of Mechanical Engineering, Ben-Gurion University of the Negev, and
Nuclear Research Center - Negev, P.O. Box 9001
Beer-Sheva, Israel

Keywords: *Coal Char, Pore Structure, Char Oxidation*

INTRODUCTION

The pore structure and its evolution during burnout are major influence on the mechanism of conversion of highly porous chars. Recently, this topic has been presented in several studies [1-8]. Pore structure, can be studied from macroscopic quantities that can be presently measured routinely. Evolution of the pore structure and its influence on char reactivity can be studied from changes in (1) external dimensions, (2) physical properties, and (3) reaction rate. In this review we concentrate on the role of pore structure for char reactivity and narrowed down to highly porous chars with no volatile or mineral matters. We present an overview, that includes only experimental results, on processes and properties for single particles of highly porous synthetic chars oxidized by oxygen. We will show that there is a general behavior connected to the evolution of the pore structure.

Spherocarb particles (synthetic char) were chosen as a model material because they have relatively well defined and reproducible, are quite spherical and have very close pore structure to certain coal chars. Only results from kinetically controlled conditions (regime I) are included. The particles were with initial total porosities in the range 70-80%, with diameters in the range 150-250 μm, oxidized in air or in pure oxygen, with or without moisture, in the temperature range 700-1200 K. Care was taken to include results that obey the Thiele criterion. Four topics will be discussed: (1) Changes in external shape of particles. (2) Fragmentation. (3) Changes in physical properties. (4) Oxidation rate.

Most of the results presented here were obtained with an electrodynamic chamber (EDC). For details on the EDC see for example in Refs. [5,9-17]. The EDC has been developed and applied for kinetic studies of single particles at high temperatures in many studies. The main advantages of the EDC are: (1) Ability to study the kinetics of a single particle in well controlled conditions. (2) Ability to characterize the particle prior to reaction and monitor the important quantities in real time during reaction. (3) The elimination of heat and mass transfer limitations existing in other methods that restrict kinetic measurements to slow rates. (4) The ability to study particle to particle variations. The quantities that were measured for single particles are: weight, shape and dimensions, density and porosity, temperature, total surface area, thermal conductivity, heat capacity, reaction rate.

OBSERVATIONS AND DISCUSSION

1. Changes in External Shape

Decrease in external dimensions of a particle is referred to as shrinkage. If reaction occurred in external surface, as in regime III and partially in regime II, change in external dimensions are understandable and expected. However, in regime I where oxygen is available to all active sites, the changes in the external dimensions must reflect the changes in the internal morphology. Two types of shrinkage have been observed: uniform and non-uniform shrinkage.

Uniform Shrinkage. Shrinkage has been observed in various studies [15,16,18-20] for highly porous synthetic chars oxidized in regime I. It has been shown [21] that shrinkage is a general phenomenon occurring for a variety of carbonaceous materials at ranges varying from tens of nanometers [22] to 70 mm [23]. Shrinkage factor was defined as the ratio of volume to initial volume. Figure I shows results for the shrinkage factor vs. conversion. The results were gathered from about forty different experiments covering the ranges of diameters, temperatures, and densities mentioned above. The shrinkage factor decreases monotonically with conversion not obeying neither the shrinking sphere model (linear decrease, constant density) nor the hollow sphere model (constant diameter). It was established [19] that shrinkage is not due to external surface reaction, but is a homogeneous reaction-induced densification of the microporous solid phase. Shrinkage is ascribed to rearrangement in the microstructure. Thus, if shrinkage is a result of morphological changes, other properties connected to the pore structure must change accordingly. Porosity (or density) and internal surface area were extensively investigated. Figure 2 presents results for normalized density vs. conversion. Density decreases with conversion to approximately half its initial value at about 85% conversion. Although at high conversion the results are scattered a clear indication of increase in density is seen. This increase may be due to densification of the solid, which is also reflected in the thermal conductivity as will be shown below. The total surface area results are less dramatic, but display the same behavior.

Non-Uniform Shrinkage. Non-uniform shrinkage has been observed [15,17] when a particle was irradiated non-uniformly. It has been quantitatively investigated in a systematic manner [24]. Results

of the shrinkage factor for non-uniform shrinkage from many runs show a similar trend to that seen in Fig. 2, however, with some meaningful differences. The shrinkage factor is equal in the two cases from zero conversion to about 50% conversion, then there is a systematic deviation between the two phenomena. Clearly, the deviation is due to different propagation of the pore structure in the two cases. The important finding is that non-uniform shrinkage is also a general phenomenon that is independent on initial values of porosity and diameter, and reaction rate. The major conclusion from both uniform and non-uniform shrinkage is that the pore structure as represented by shape, external dimension, porosity and total surface area, is undergoing a pattern that is equal to all cases regardless the initial conditions or reaction rates.

2. Fragmentation

Fragmentation is another phenomenon that can shed light on the nature of the pore structure and its evolution. The mechanism that arises from the evolution of the pore structure is usually referred to as percolation fragmentation for oxygen percolates through the porous structure and "erodes" the carbon microcrystals with a possible subsequent fragmentation. Percolation fragmentation of carbon spheres during oxidation was reported in a number of studies [25-28]. A theory for percolation fragmentation was developed and showed that for any homogeneous material, fragmentation will occur at a critical porosity of about 70% [28]. Recent observation [15,24] showed also local percolation fragmentation. These results strengthen the thesis that fragmentation is a threshold phenomenon that occurs above a critical porosity, as predicted in [28]. More than one hundred experiments were carried out up to 80% conversion. None of these showed any fragmentation but a few (two or three) showed formation of a hole in the center of the particle. This was indicative to local percolation fragmentation and was predicted by a recent model [23]. Another twenty-two experiments were conducted up to completion and half of them developed holes in the particle center. Out of these, only a few particles broke into two particles. The formation of holes is resulting from the evolution of the pore structure. In all experiments the particle underwent non-uniform shrinkage, transforming the initially spherical particle into a disk at 50-60% conversion. At higher conversion (above 85%) about half of the particles developed holes in the center. Figure 3 presents a typical conversion vs. time curve with a sequence of shadowgraphs depicting the shape development of a Spherocarb particle of 204 micron diameter at various conversions, oxidized in air at T=920 K. Spatial dimensions of the particle are included in the figure. Three regions of oxidation are observed: (i) at low conversion the particle hardly loses mass; (ii) quick mass loss from about 4% conversion to about 95 conversion; and (iii) very slow mass loss from about 95% up to completion. The initially spherical particle turned into a disk at about 60% conversion.

To conclude, formation of holes is a manifestation of the pore structure evolution displayed more pronouncely in disk-shaped particles, formed due to non-uniform shrinkage. Finally, breaking of the particle is a mere coincidence and a random incident where a particle can break due to growth and overlap of large macropores. The important thing is that in all these experiments, the behavior during oxidation was identical for all particles, regardless of initial conditions and oxidation rate.

3. Changes in Physical Properties

Some physical properties of chars depend on distribution of voids and solid microcrystals. Other properties are the reflection of the details of the pore structure, such as connectivities, microcrystal dimensions. Density, total surface area, and heat capacity, belong to the former and thermal conductivity to the latter. In both groups the behavior of the properties depend on the evolution of the pore structure. Thermal conductivity was systematically studied recently [16,29,30] and was shown to be a very strong tool for details of the pore structure and its evolution.

Thermal conductivity. It has been clearly shown [29] that all previous concepts for highly porous materials cannot explain the strong observed change in thermal conductivity with conversion. The surprising result is that total porosity plays a minor role in the evolution of the thermal conductivity. A model showing that thermal conductivity is a property that is highly capacious of the information on the internal microstructure has been developed [29]. Main conclusions are that thermal conductivity is affected by: (1) Consumption of carbon on the internal surface. (2) Coalescence of microcrystals. (3) Activation of intercrystal joints. The change in thermal conductivity k_p with conversion was found to be similar for all particles, regardless of initial conditions or reaction rate. Figure 4 shows k_p/k_{min} (min refer to minimum) for eleven particles at different temperatures. The value of k_p/k_{min} decreases with conversion by a factor of 5-7 from zero to 30% conversion. k_p/k_{min} remains constant until 80% conversion, then it rises by a factor of 2-3 from about 90% conversion to final burnout. The results from the common models [32] show a very poor match to the experimental data. k_p/k_{min} decreases much slower with conversion at low conversions than observed and it behaves opposite to the observed behavior at high conversions. However, a good fit to the model that includes the features of the micromedium was obtained. The significance of these results is that it is most probable that the main role in the change in thermal conductivity, both at low and high conversion, is the change in the dimensions of microcrystal joints. At low conversion the fast

decrease in k_p can be explained by activation of intercrystal joints, i.e., breaking the joints. The increase of thermal conductivity at high conversion can be ascribed to the increase in the radius of an intercrystal joint. The increase of a joint is a manifestation of better ordering of an individual microcrystal. The abruptness of the increase is likely to reflect the spontaneity of the process. Therefore, we interpret the increase in k_p as an indication of conversion induced graphitization. An indication to graphitization at final burnout stages can be found in a recent study [31] where high-resolution tunneling electron microscopy was used. We should, therefore, conclude that the more likely model to represent thermal conductivity is the one that considers the details of the micromedium structure (including nature of connections between microcrystals) and does not consider the porous structure as a mere two-phase medium -- solid/gas -- as represented in most thermal conductivity models [32]. This conclusion strengthens the importance of thermal conductivity for the understanding of changes in the pore structure of highly porous media in general, and for chars in particular.

4. Mass Transients

Numerous measurements of mass loss were carried out for Spherocarb particles reacting in regime I at the range of conditions specified above. A convenient way of presenting the data is conversion vs. normalized time (by time at half conversion -- $t_{1/2}$), as shown in Fig. 5. The various results fall within one curve, within experimental uncertainty (larger scatter at long time region). Three regions of behavior are observed: (1) slow mass loss with time in the early stages of burnout; (2) fast reaction; and (3) slow reaction at final burnout. Figure 6 shows normalized reaction rate (with $t_{1/2}$) vs. conversion measured from different studies at various temperatures. The fact that all results (transients and rates) can be normalized by one quantity ($t_{1/2}$) has a very strong significance: All three stages of conversion are strongly related to the same mechanism. Note that this mechanism prevails for all conditions of regime I. One can deduce that consumption of carbon is governed by one mechanism. Dividing the consumption process into two stages, one at which reaction sites are activated and the other is the actual gasification (solid carbon turns into gaseous carbon, i.e., CO or CO_2). Clearly, from the results of Figs. 5 and 6, gasification (stage 2) cannot be the rate determining step for it is unlikely that the two mechanisms have the same activation energies. Thus, the only conclusion that one can draw from this behavior is that activation of sites is the dominant mechanism that governs the consumption of carbon. Active sites, however, are a direct consequence of the evolution of the pore structure. Therefore, the reactivity of chars as physical properties discussed above are also a direct consequence of the pore structure.

In light of this conclusion one can draw a picture of the reactivity behavior of highly porous chars. In the early stages of burnout reactive sites are very scarce and reaction is very slow. As reaction proceeds, morphology and crystallinity change, and as a consequence reactive sites start to build up and reactivity increases. At some stage, reaction progressed such that reactive sites start to decline, resulting in decreasing of reaction rate, that occurs at high conversion. In fact from this description one can deduce that the behavior of reaction rate is a consequence of the change in active sites an that the intrinsic reaction rate is constant with conversion.

SUMMARY

The selection of Spherocarb particles has given us the opportunity to examine physicochemical processes under well defined and reproducible conditions. Differences were only on total porosity and diameter. The numerous results obtained in a wide range of conditions has provided a wide-angled view that can help elucidate the governing mechanisms for oxidation. Each of the physical properties studied has behaved in a certain quantitative way equal in all experiments. Similarly, the phenomena of shrinkage and fragmentation showed, each, clear and reproducible pathways. Dependence of reaction rate on temperature, on oxygen concentration, on conversion, on time has shown also a clear pattern regardless of initial conditions. From these observations it is inevitable to reach the conclusion that all these processes and quantities are related to the pore structure and its fine tunes. The most striking evidence is the results of conversion versus normalized time that showed clearly that all stages of conversion must be all connected to one mechanism. This conclusion, however, is only circumstantial. We do not have yet results from direct observation of microscopic changes (morphology and crystallinity) for Spherocarb particles. Still the numerous macroscopic data can serve as strong indication of the microscopic processes. Insights can be gained if a model that includes the microscopic features and can reconstruct the numerous physicochemical experimental data, by minimum parameter fitting.

References

1. Sahimi, A., Gavalas, G.R., and Tsotsis, T.T., Chem. Eng. Sci. **45**:1443 (1990).
2. Hurt, R.H., Sarofim, A.F., and Longwell, J.P., Energy & Fuel **5**:290 (1991).
3. Miccio, F., and Salatino, P., 24th Sym. (Int.) on Combustion, The Combustion Institute, Pittsburgh, 1992, pp. 1145-1151.
4. Salatino, P., Miccio, F., and Massimilla, L., Combust. Flame **95**:342 (1993).
5. D'Amore, M.D., Tognotti, L., Sarofim, A.F., Combust. Flame, **95**:374 (1993).
6. Salatino, P., Miccio, F., 24th Sym. (Int) on Combustion, The Combustion Institute, Pittsburgh, PA, 1994, pp. 1145-1151.
7. Kantorovich, I.I, and Bar-Ziv, E., Combust. Flame **97**:61 (1994).
8. Kantorovich, I.I, and Bar-Ziv, E., Combust. Flame **97**:79 (1994).
9. D'Amore, M., Dudek. R.D., Sarofim, A.F., and Longwell, J.P., Powder Technology **56**:129 (1988).
10. Dudek, D.R., Fletcher, T.H., Longwell, J.P., and Sarofim, A.F., Int. J. Heat Mass Transfer **31**:863 (1988).
11. Bar-Ziv, E., Jones, D.B., Spjut, R.E., Dudek, D.R., Sarofim, A.F., and Longwell, J.P., Combustion and Flame **75**: 81 (1989).
12. Tognotti, L., Longwell, J.P., and Sarofim, A.F., 23rd Sym. (Int.) on Combustion, The Combustion Institute, Pittsburgh, 1990, pp. 1207-1213.
13. Bar-Ziv, E., Longwell, J.P., Sarofim, A.F., Energy and Fuels **5**:227 (1991).
14. Bar-Ziv, E., and Sarofim, A.F., Prog. Energy Comb. Sci. **17**:10 (1991).
15. Weiss, Y., and Bar-Ziv, E., Combust. Flame **95**:362 (1993).
16. Weiss, Y., Ben-Ari, Y., Kantorovich, I.I., Bar-Ziv, E., Krammer, G., Modestino, A., and Sarofim, A.F., 25th Sym. (Int.) on Combustion, The Combustion Institute, Pittsburgh, PA 1994, pp. 519-525.
17. Weiss, Y., and Bar-Ziv, E., Combustion and Flame **101**:452 (1995).
18. Weiss, Y., Ph.D. Thesis, Ben-Gurion University of the Negev, 1995.
19. Hurt, R.H., Dudek, D.R., Longwell, J.P., and Sarofim, A.F., Carbon **25**:433 (1988).
20. Dudek, D.R., Ph.D. Thesis, Massachusetts Institute of Technology, Cambridge, MA, 1988.
21. Hurt, R.H., Sarofim, A.F., and Longwell, J.P., Combust. Flame **95**:430 (1993).
22. Ishiguro, T., Suzuki, N., Fujitani, Y., and Morimoto, H., Combust. Flame **85**:1 (1991).
23. Easler, T.E., Bradt, R.C., and Walker, P.L., Fuel **69**:124 (1990).
24. Zhang, X., Dukhan, A., Kantorovich, I.I., and Bar-Ziv, E., "Bulk Fragmentation of Highly Porous Char Particles in Regime I," Combust. Flame **XX**:XXX (1995).
25. Davis, H., and Hottel, H.C., Ind. Eng. Chem. **26**:889 (1934).
26. Walker, P.L., Jr., Rusino, F., and Austin, L.G., Adv. Catal. **11**:133 (1957).
27. Dutta, S., Wen, C.Y., and Belt, R.J., Ind. Eng. Chem. Proc. Des. Dev. **16**:20 (1977).
28. Kerstein, A.R., and Niksa, S., 20th Sym. (Int.) on Combustion, The Combustion Institute, Pittsburgh, 1984, pp. 941-949.
29. Kantorovich, I.I, and Bar-Ziv, E., "The Effect of Microstructural Transformation on the Evolution of Thermal Conductivity of Highly Porous Chars during Oxidation," Combust. Flame, (1995).
30. Dukhan, A., Zhang, X., Kantorovich, I.I., and Bar-Ziv, E., "Thermal Conductivity and Porosity of Char Particles in Regime I," submitted to 26th Sym. (Int.) on Combustion, The Combustion Institute, Pittsburgh, PA 1996.
31. Davis, K.A., Hurt, R.H., Yang, N.Y.C., nd Headly, T.H., 25th Sym. (Int.) on Combustion, (The Combustion Institute, Pittsburgh, PA 1994), pp. XXX-XXX.
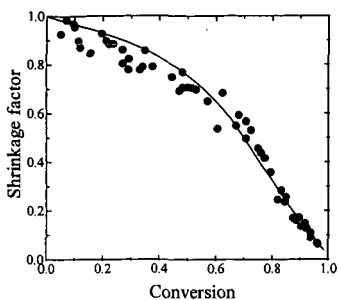32. Hashin, Z. and Shtrinkman, S., J. Appl. Phys. **10**:3125 (1962).

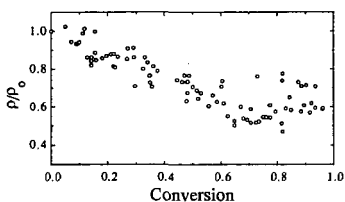Figure 1. Shrinkage factor versus conversion for uniform shrinkage [9,16,19,20].

Figure 2. Ratio of density to initial density vesrus conversion [7,17,19,20].
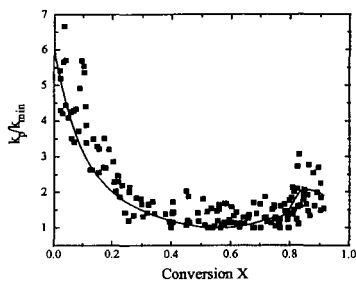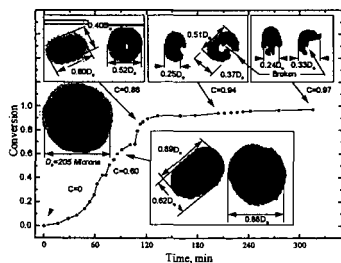

Figure 3. Conversion versus time and a sequence of shadowgraphs presenting the development of shape of a 204 microns Spherocarb particle vs. conversion oxidized in air at 920 K; C is conversion, l is length, and w is width.
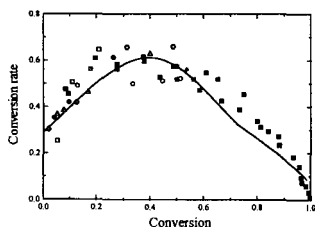

Figure 4. Ratio of thermal conductivity to its minimum value, k_p/k_{min} as a function of conversion.
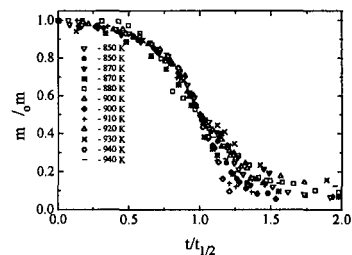
Figure 5. Conversion versus normalized time τ (by time at half conversion -- $t_{1/2}$) for particles oxidized under un-even temperature field.

Figure 6. Normalized reaction rate defined as $dC/d\tau$ versus conversion [9,12,20].